PRINTED ISSN: 1308-9080 / OLINE ISSN: 1308-9099

Volume: 15 / Number: 2 / Year: 2020

TURKISH JOURNAL OF SCIENCE & TECHNOLOGY

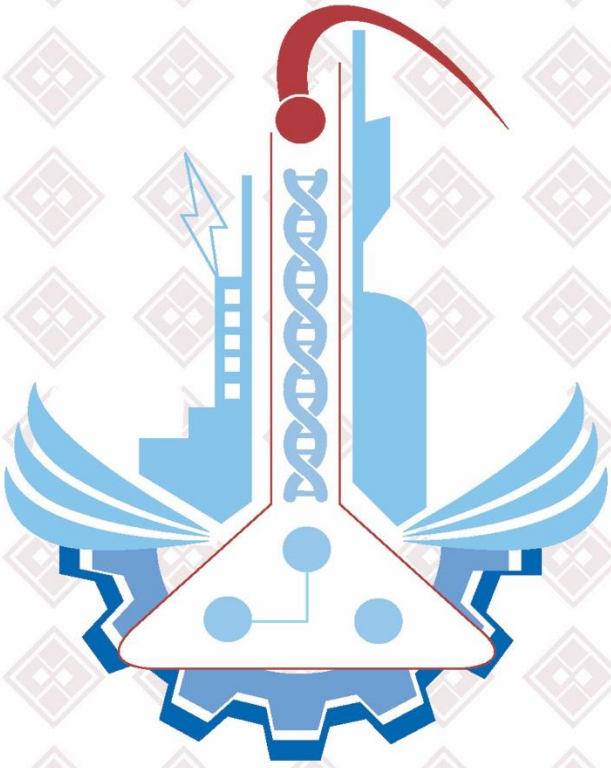

TURKISH JOURNAL OF SCIENCE & TECHNOLOGY (TJST)
Published by Firat University

TURKISH JOURNAL OF SCIENCE & TECHNOLOGY (TJST)
Published by Firat University

Owner

Prof Dr. Fahrettin GÖKTAŞ
Fırat Üniversitesi Rektörü

Responsible Director

Prof. Dr. Soner ÖZGEN
F.Ü. Fen Bilimleri Enstitüsü Müdürü

Editor in Chef
Prof. Dr. Erkan TANYILDIZI

Fırat University, Technology Faculty
Department of Software Engineering

Editor
Assis. Prof. Dr. Sencer ÜNAL

Fırat University, Engineering Faculty
Department of Electrical-Electronics Engineering

ADVISORY BOARD

Fırat University Turkish Journal of Science & Technology (TJST)
15-2, 2020

CONTENTS / İÇİNDEKİLER

Turkish Journal of Science & Technology
15(2), 49-60, 2020

A Control of SynRM using MPPT Algorithm and Effects of Advance Angle on Motor Performance

Gullu BOZTAS[1*], Omur AYDOGMUS[2], Hanifi GULDEMIR[3]
[1,3]Electrical and Electronic Engineering, Technology Faculty, Firat University, Elazig, Turkey
[2]Mechatronics Engineering, Technology Faculty, Firat University, Elazig, Turkey
[*1]gboztas@firat.edu.tr, [2]oaydogmus@firat.edu.tr, [3]hguldemir@firat.edu.tr

(Geliş/Received: 26/03/2020; Kabul/Accepted: 30/07/2020)

Abstract: Solar-powered irrigation systems are quite important in terms of renewable energy usage. These systems consist of solar panel, boost converter, battery, battery charge management system, motor drive, motor and pump. The installation costs of system increase and the system reliability reduces due to the amount of equipment. Nowadays, low-voltage Permanent Magnet Synchronous Motors (PMSMs) are used to eliminate drawbacks of the boost converter. However, PMSMs have high cost because of the magnets. Synchronous Reluctance Motors (SynRMs) having lower cost than PMSMs can be used in these applications. The proposed system can be operated by using only the solar-panel, SynRM and drive without other devices. Thus, the system cost can be significantly reduced. In addition, durability of the system can be increased due to not using battery and magnets causing problems such as maintenance and low lifespan. A SynRM pump motor which can operate with a lower voltage level generated by the photovoltaic (PV) panel was designed in this paper. This motor has high efficiency because of no-copper losses of the rotor. Effects of advance angle on designed motor performance were analyzed and suitable advance angle was selected for the motor. Additionally, the designed SynRM was controlled by the MPPT algorithm.

Key words: AC Motors, Energy Conversion, Energy Efficiency, Solar Energy, Advance Angle, SynRM

MPTT Algoritması Kullanarak SynRM'nin Kontrolü ve İlerleme Açısının Motor Performansı Üzerindeki Etkileri

Öz: Güneş enerjisiyle çalışan sulama sistemleri, yenilenebilir enerji kaynak kullanımı açısından oldukça önemlidir. Bu sistemler güneş paneli, yükseltici çevirici, batarya, batarya şarj yönetim sistemi, motor sürücü, motor ve pompadan oluşur. Bu sistemlerde kullanılan ekipman miktarından dolayı sistem maliyeti artar ve sistem güvenirliği azalır. Günümüzde yükseltici çeviricinin dezavantajlarını ortadan kaldırmak için düşük gerilim seviyeli Sabit Mıknatıslı Senkron Motorlar (SMSM) kullanılır. Fakat kalıcı mıknatıslardan dolayı SMSM'ler yüksek maliyeti sahiptir. Senkron Relüktans Motorlar (SynRM), SMSM'lerden daha düşük maliyete sahiptir. Önerilen sistem; sadece güneş paneli, SynRM ve motor sürücüsü kullanılarak gerçekleştirilebilir. Böylece sistem maliyeti önemli ölçüde azaltılabilir. Ayrıca bakım ve düşük kullanım ömrü gibi sorunlara neden olan batarya ve mıknatısların kullanılmaması nedeniyle sistemin dayanıklılığı arttırılabilir. Bu çalışmada; Fotovoltaik (FV) panel tarafından üretilen düşük gerilim seviyesinde çalışabilen bir pompa motoru tasarlanmıştır. Tasarlanan motor rotorunda bakır kayıpları olmamasından dolayı yüksek verime sahip olan SynRM olarak tasarlanmıştır. Tasarlanan motor performansı üzerinde ilerleme açısının etkileri incelenmiştir ve motor için uygun ilerleme açısı seçilmiştir. Ayrıca tasarlanan SynRM, MPPT algoritması ile birlikte kontrol edilmiştir.

Anahtar kelimeler: AA Motorlar, Enerji Dönüşümü, Enerji Verimi, Güneş Enerjisi, İlerleme açısı, SynRM

1. Introduction

Nowadays, global warming and energy policies have become an important issue on the international agenda. Greenhouse gas emissions have been reduced by developed countries. PV system has become an important renewable source because it can generate electricity without emitting greenhouse gasses [1]. In addition, PV panels are a suitable solution for areas far from the electric source. The efficiency of the PV power stations has three factors such as the efficiency of the PV panel (8-15%), the efficiency of the inverter (95-98%) and efficiency of the Maximum Power Point Tracking (MPPT) (98%) [2]. Nowadays, the efficiency of the PV panels is reached up

* Corresponding author: gboztas@firat.edu.tr. ORCID Number of authors: [1]0002-1720-1285, [2]0001-8142-1146, [3]0003-0491-8348

only 22% by very few producer firms (Panasonic, SunPower, etc.). MPPT is an important parameter in order to obtain desired maximum power in the PV systems. MPPT algorithms must be used in the PV systems because PV panel arrays have a nonlinear voltage-current (V-I) characteristic with only one maximum point. This point depends on irradiation conditions and panel temperature changed by weather through both days and seasons. There are nearly 20 different MPPT algorithm in the literature [3–5]. Perturb and Observe (P&O) and Incremental Conductance (InCond) are more widely used than other algorithms. In addition, there are MPPT algorithms such as fuzzy logic, artificial neural network, fractional open circuit voltage or short circuit current, current sweep.

Electric motors consume nearly 50% of total electrical energy. Especially, fan, pump and compressor motors constitute more than half of the consuming electrical energy of the motors [6]. Generally, three-phase induction motors are widely used in all of the motor applications. Therefore, numerous studies have been performed in order to increase the efficiency of the induction motors. Reduction gear systems and/or belt-pulley systems are generally used so as to obtain high torque from an induction motor at low speed region. However, these systems have low efficiency because of high friction. DC motors were preferred in low speed-high torque applications in the past. Brushless DC (BLDC) motor and PMSM have been used since 1980's. They do not require brush-collector and rotor winding. These motors known as synchronous motor have advantages such as high performance, low volume and high efficiency [7–9]. They have a major problem such as not available direct-starting with grid connected. Therefore, these motors require a motor drive. They have high costs because these motors have magnets on the rotor. Therefore, in nowadays, Synchronous Reluctance Motors (SynRM) have a rising trend because of not requiring any windings and magnets on the rotor. SynRM can produce shaft torque by using reluctance concept similarly sinusoidal rotating magnetic field generated from the stator of the traditional induction motor. The theoretical concept of reluctance torque was firstly presented by Kostko in 1923 [10]. SynRM has become popular thanks to developing power electronic drive systems with feedback control. Field Oriented Control (FOC), Direct Torque Control (DTC) and similar methods is presented in literature in order that SynRM can be operated [11–15].

Until nearly two decades ago, SynRMs were less preferred because they had higher torque ripples and lower average torque according to the other AC motors. The efficiency and torque of SynRMs are increased by developing of the motor design program. Nowadays, modern SynRMs can generate 15-20 % more torque than same-size induction motor [16,17]. Also, SynRMs have a lower power loss and higher torque according to induction motor at the same stator current. Both performance and efficiency of the SynRMs can be increased by using a motor drive. SynRMs may have unstable operation points when operated with a simple V/f control. Therefore, FOC or DTC is widely preferred in order to control speed of SynRMs. These control methods are required either rotor position or flux position information. Sensorless speed control methods are generally used instead of mechanical position encoders due to low cost and high robustness. DTC is simpler than FOC though most of researchers focus on FOC for sensorless motor drive [13,18–21]. Consoli and et al. are proposed sensorless torque control for SynRM drives. SynRMs are used in variable speed applications with high efficiency [16,22–24]. These motors are more superior than induction motors because of simpler of mass production, higher efficiency, higher density of torque [11,24] higher load capacity and lower rotor temperature. SynRMs have become popular due to these superior properties [25–27]. However, these machines require an inverter bigger than standard size inverter due to their low power factor (PF) [10]. The PF of SynRM can be increased by using rotor structure assisted Permanent Magnet (PM) which is known as Permanent Magnet Assisted SynRM (PMaSynRM) [11,28].

In this work, a pump motor was designed a SynRM directly connected to PV panels which generate a low voltage level. Robustness of SynRM rotor is higher than other motors because SynRM has not magnets and windings on its rotor. In addition, SynRM has constant efficiency and constant torque with independent speed. An MPPT algorithm was modified in order to continuously obtain maximum speed from the motor drive. This system has more efficiency, more compact and user friendly than other pump motor drive systems. Firstly, the effects of rotor shape were analyzed with 9 different types of the rotor in this paper. Then, optimal rotor type was analyzed with Finite Element Method by using Magnet/Infolytica. Effects of advance angle on performance of the designed motor were analyzed and suitable advance angle was selected for the motor. The proposed system can be operated by using only the solar-panel, selected optimal SynRM and drive without battery, battery management system and boost converter. The current commercial system and proposed system are given in Figure 1.

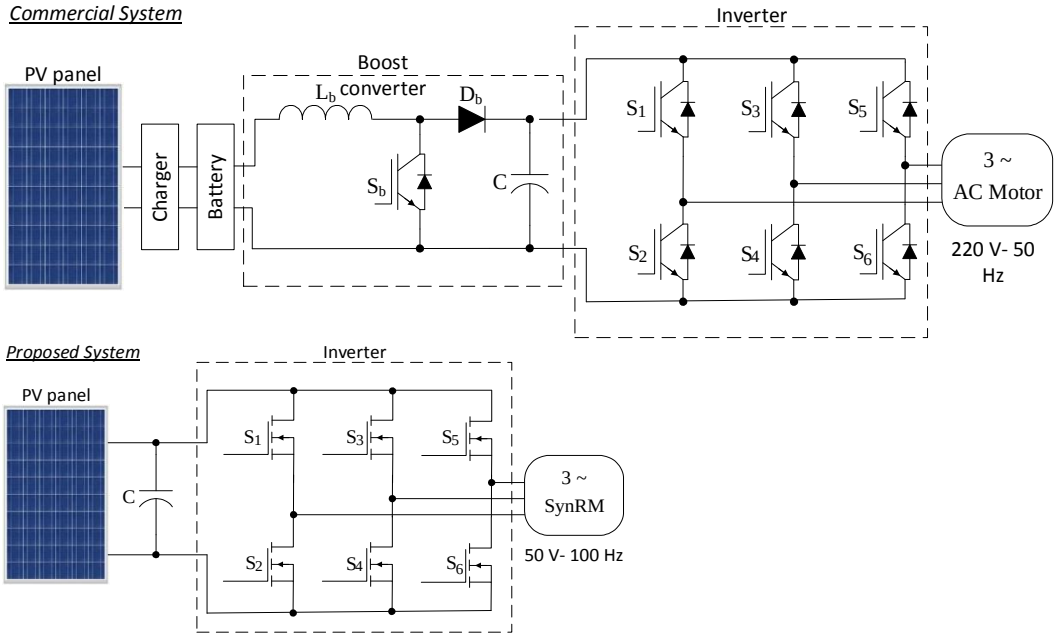

Figure 1. a) Commercial system, b) Proposed system with SynRM

Nowadays, pump systems which do not require battery, battery management system and boost converters are available in the market for PV systems. So far, SynRM has not been used for these pump systems in the market. The main contribution of this study is to obtain a high efficiency solar-based pump system instead of the traditional pump systems. Additionally, the purposed motor has a lower stator stack length and no copper losses on the rotor when compared with an induction motor.

2. Design of SynRM

In this paper, SynRM was designed as 30 slot stator and 4 barrier rotor. Other constant values of the motor parameters were taken in appendix. Rotor core has air barriers through the *q*-axis in order to both increase L_d inductance and decrease L_q inductance. Rotor rips were chosen as possible as narrow, so that flux generated in stator can be oriented to the rotor. Thus, the desired high reluctance torque was obtained. The outer diameter of designed motor was taken as 90 mm. Firstly, the effects of rotor shape were analyzed with 9 different types of the rotor in this paper. Barriers and rips of the rotor were arranged in order to show the effect on the motor performance of rotor shape. As shown in Figure 2, barriers, rips and iron bridge thickness of the rotors were named as ST, WT and BT, respectively. Besides, R_O and R_i are outer and inner radius of the rotor. Design parameters of the rotors are given in Table 1. All dimensions have been given in mm.

Table 1. Rotor Design Parameters

Design	ST1	ST2	ST3	ST4	WT1	WT2	WT3	WT4	WT5	T(Nm)
D1	2.82	2.03	1.27	1.04	2.38	2.92	1.79	2.08	4.70	**2.27**
D2	2.28	2.28	2.28	2.28	2.57	2.28	2.28	2.28	2.50	**2.22**
D3	2.94	2.90	2.90	2.90	2.57	1.45	1.45	1.45	2.50	**2.33**
D4	1.59	1.60	1.60	1.60	2.57	3.20	3.20	3.20	2.50	**2.10**
D5	3.06	2.82	2.58	2.35	2.57	1.56	1.72	1.88	2.50	**2.33**
D6	**3.62**	**3.04**	**2.47**	**1.90**	**2.57**	**1.26**	**1.65**	**2.03**	**2.50**	**2.29**
D7	3.08	2.46	1.84	1.23	2.57	3.07	2.46	1.84	2.50	**2.23**
D8	2.67	2.43	1.90	1.10	2.57	2.61	2.43	1.90	3.50	**2.23**
D9	3.89	3.52	2.50	1.11	2.17	2.42	2.42	2.42	0.50	**2.27**

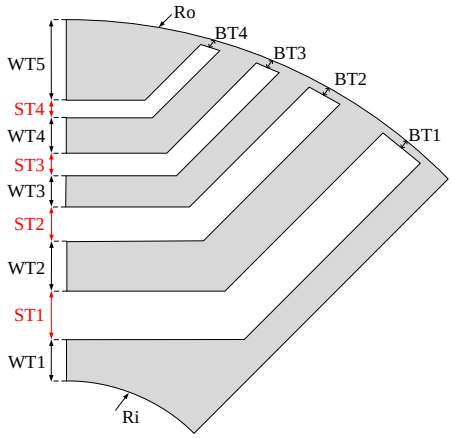

Figure 2. Rotor structure

The flux density distributions in the stator and the rotor of designed SynRMs are illustrated in Figure 3. The material of lamination was determined as M530-50. Additionally, speed-torque curves of the motors are given in Figure 4. Optimal rotor shape was determined by examining the flux density distributions and speed-torque curves. It can be said that all the structures of the designed motors have small differences with each other.

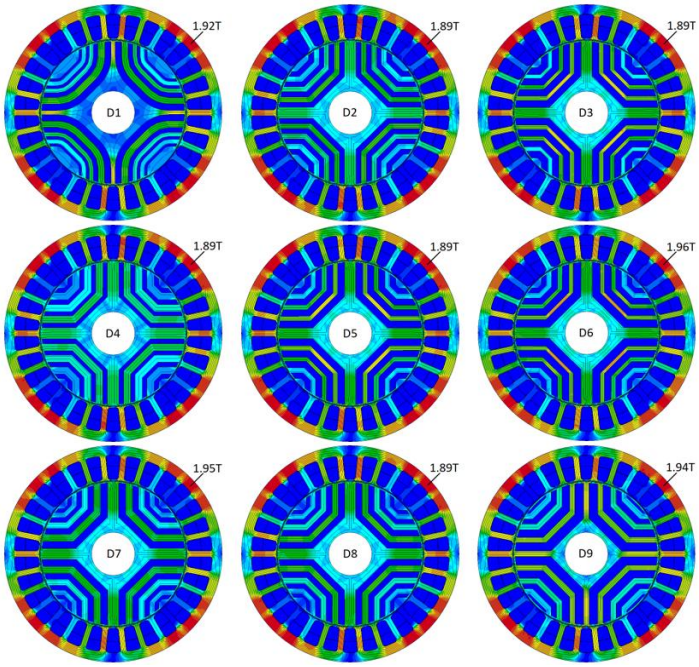

Figure 3. The flux density distribution of the designed motors

All designed motors are produced up to 2 Nm when the speed-torque curves of designed motor are compared each other as shown in Figure 4. It is observed that the flux in rotor types generating high torque is intensified throughout rotor rips. It is the right approach to make the rips as thin as possible in the rotor design. The flux of the D6 motor is more intensified than the other motors throughout rotor rips and D6 motor produces the highest flux according to others. Breakdown torque of the D6 motor is higher than other designed motors. Additionally, this motor has high torque at high speeds than the others. Therefore, D6 motor was selected as the most suitable motor to use in this paper, though average torque of the D6 motor is lower than D3 and D5 motors.

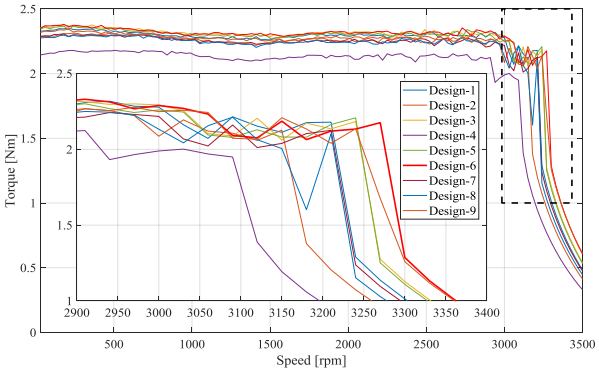

Figure 4. Speed-torque curves of the designed motor

The dimensions of the motor are shown in Table 1. It is aimed to operate in a constant torque region, which is between 0 and 3000 rpm. The advance angle is an important parameter in order to generate high torque. Effecting on the speed-torque curve of the advance angle is illustrated in Figure 5. It must be considered that the motor produces high torque at the nominal speed while the advance angle is determined. It can be seen that optimal advance angle of the motor is 54° as shown in Figure 5.

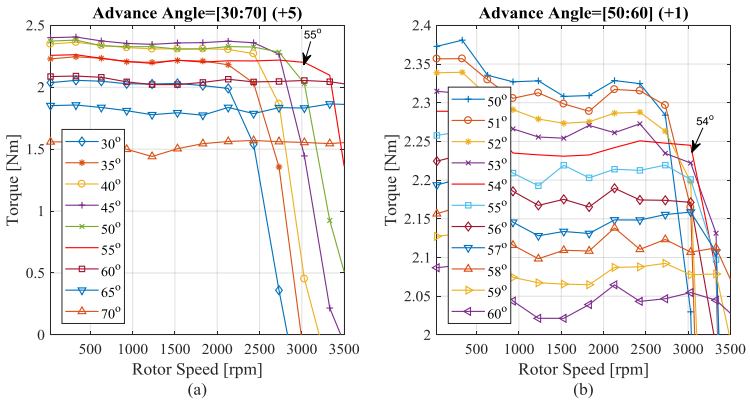

Figure 5. The effects on the speed-torque curve of the advance angle

D6 motor was analyzed with Finite Element Method (FEM)-Newton Raphson Iteration by using Magnet/Infolytica program. Maximum element size is 1 mm, maximum Newton iteration number is 50 and Newton iteration tolerance is 1% in FEM. Additionally, start, stop and step times have been taken as 0, 20 ms and 10 ms, respectively. The torque of the motor is shown in Figure 6. The motor produces nearly 2.4 Nm.

Mesh of the motor is given Figure 7a. Maximum element size of the mesh has been taken as 1 mm. The flux density distribution of the motor is obtained as illustrated in Figure 7b. The maximum motor flux is nearly 1.96 T.

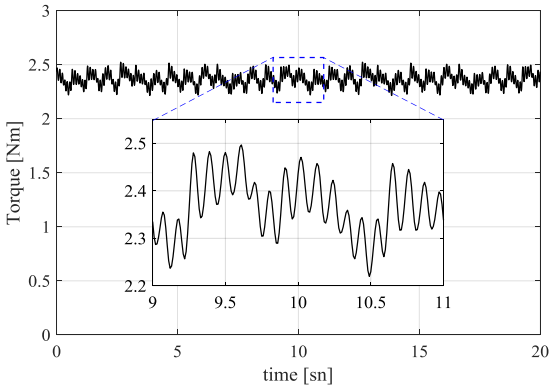

Figure 6. Torque curve of the optimal motor

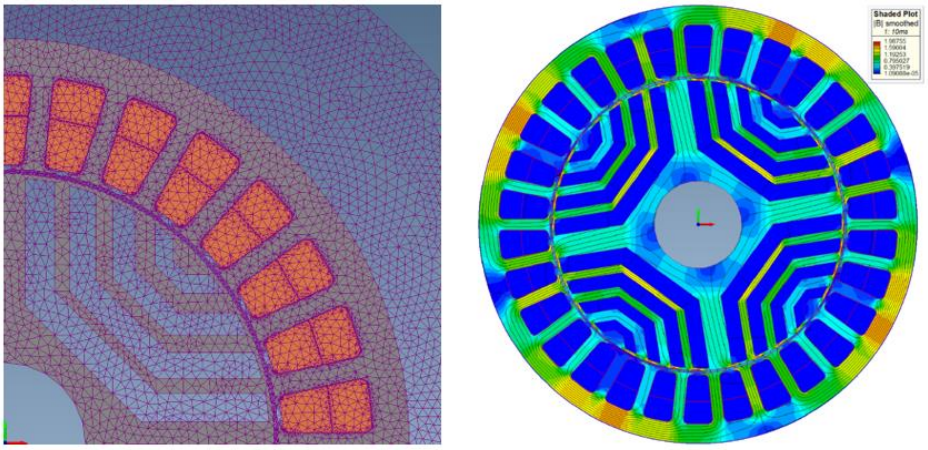

Figure 7. a) Mesh of the motor, **b)** The flux density distribution

The curves of torque, output power, efficiency and PF according to speed are illustrated in Figure 8. The motor is operated in the constant torque region. The obtained torque as 2.3 Nm is kept up from standstill to steady-state. The efficiency of the motor is obtained as 86.4% at the nominal speed. Also, the efficiency is approximately 75% at the half of the nominal speed. Output power is 715 W at the rated speed. PF is a disadvantage for SynRMs. It can be shown that the PF factor is lower than the equal AC motors.

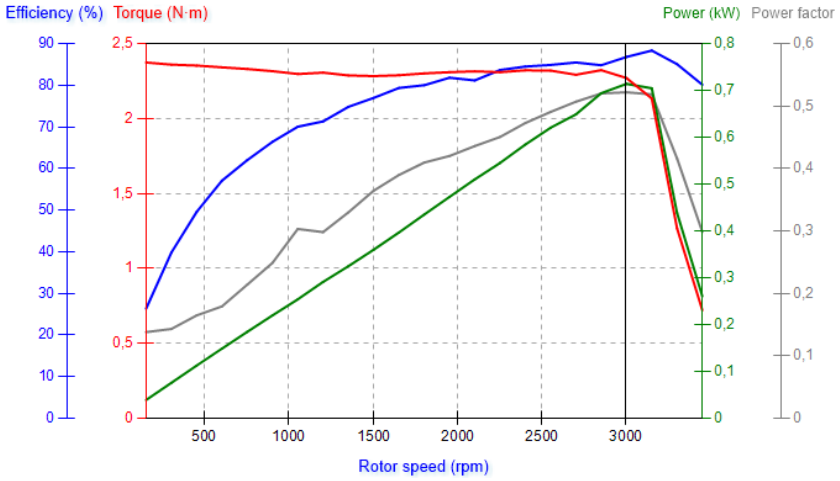

Figure 8. Torque, output power, efficiency and PF of SynRM

Parameters of designed SynRM are given in appendix. It shows that the value of K_t is zero because there is no magnet on the rotor. Increasing of the L_d/L_q is an important parameter in order to obtain high torque from motor. In this work, L_d/L_q is obtained as 3.74.

3. Control of SynRM

The SynRM has been controlled by using DTC algorithm and the control algorithm diagram is given in Figure 9. The stator flux vector plane ia divided into six sectors θ_1-θ_6. The switching logic of the traditional DTC is given in Table 2. This DTC algorithm needs information of the stator flux (λ_s) and the electromagnetic torque (T_e). The equations of torque and stator flux are given in Equations (1)-(4). The PI parameters of the speed controller are determined as k_p=0.25, k_i=5.

Table 2. Switching logic of the classical DTC

Sectors →		*θ1*	*θ2*	*θ3*	*θ4*	*θ5*	*θ6*
ξλ=1	*ξT=1*	V_2 (110)	V_3 (010)	V_4 (011)	V_5 (001)	V_6 (101)	V_1 (100)
	ξT=-1	V_6 (101)	V_1 (100)	V_2 (110)	V_3 (010)	V_4 (011)	V_5 (001)
ξλ=-1	*ξT=1*	V_3 (010)	V_4 (011)	V_5 (001)	V_6 (101)	V_1 (100)	V_2 (110)
	ξT=-1	V_5 (001)	V_6 (101)	V_1 (100)	V_2 (110)	V_3 (010)	V_4 (011)

$$\lambda_\alpha = \int \left(V_\alpha - i_\alpha R_s\right) dt \tag{1}$$

$$\lambda_\beta = \int \left(V_\beta - i_\beta R_s\right) dt \tag{2}$$

$$\left|\lambda_s\right| = \sqrt{\lambda_\alpha^2 + \lambda_\beta^2} \tag{3}$$

$$T_e = \frac{3}{2} P \left(\lambda_\alpha i_\beta - \lambda_\beta i_\alpha\right) \tag{4}$$

where λ_α and λ_β are flux of α and β axis, respectively. MTPA trajectory can be shown in Equation (5).

$$\left|\lambda s\right|^* = \sqrt{\frac{2}{3P} \frac{L_d^2 + L_q^2}{L_d - L_q} \left|T_e\right|^*} \tag{5}$$

where $|\lambda_s|^*$ and $|T_e|^*$ are stator flux reference and torque reference, respectively.

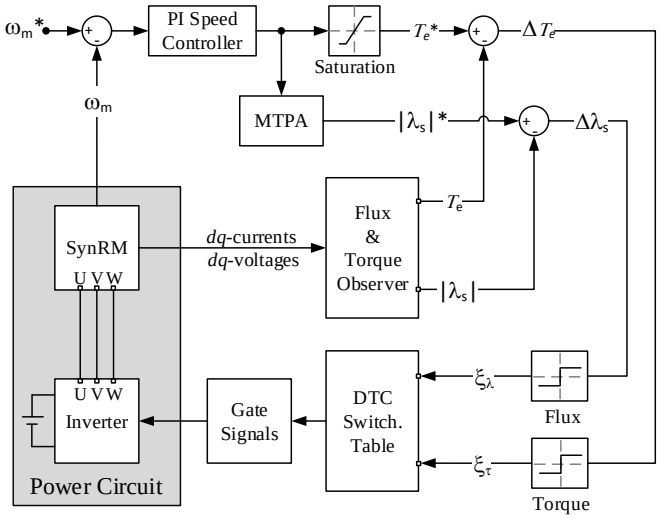

Figure 9. Block diagram of the SynRM control

MPPT algorithms are required for PV applications because the maximum power point (MPP) of the solar cells dependents on the unstable irradiation and temperature. Many MPPT algorithms are available in the literature. Perturb–Observe (P&O) and Incremental Conductance (IC) are widely used in nowadays. P&O algorithm is preferred as shown in Figure 10 in this study. The P&O algorithm has been modified for motor speed control. The reference motor speed is determined by using MPPT algorithm.

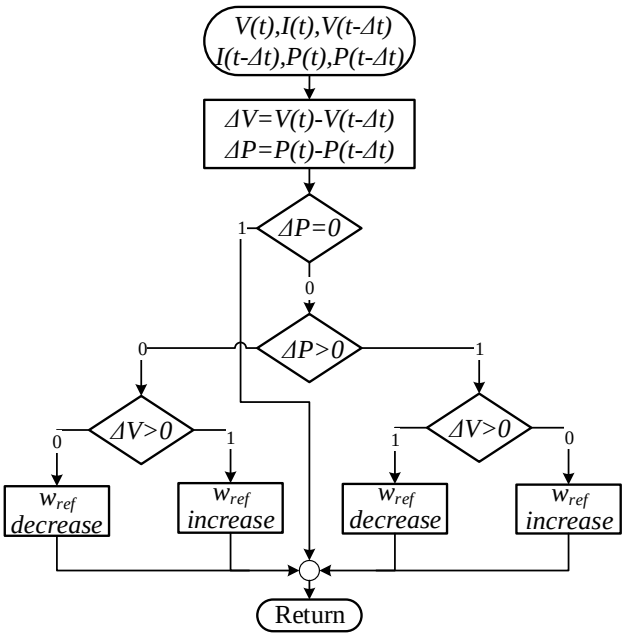

Figure 10. Modified P&O algorithm for the motor speed control

MPP is illustrated on V-I and V-P curves of the PV panel for different irradiation and temperature conditions in Fig. 11. The model of the PV panel having 2 series modules and 2 parallel strings is Soltech STH-245-WH. V-I and V-P curves of the PV panel are illustrated in Fig. 11a and Fig. 11b for 0.25 kW/m^2, 0.75 kW/m^2 and 1 kW/m^2 irradiation conditions at 25ºC. The panel current and power increase at MPP when irradiation value of the PV panel increases at the same temperature. Additionally, voltage and power of the panel decrease at MPP when the temperature value of the PV panel increases at the same irradiation condition as shown in Fig. 11c and Fig. 11d.

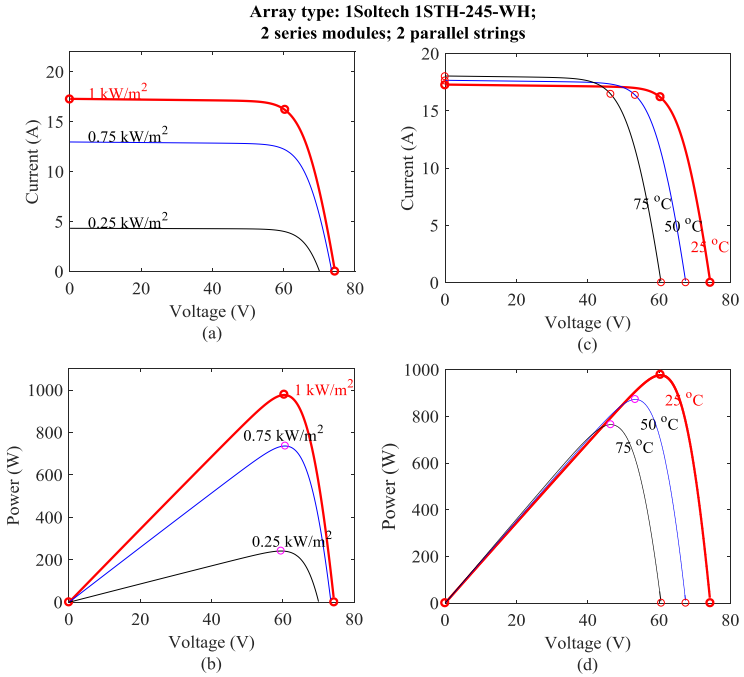

Figure 11. V-I and V-P curves of the PV panel for; **a/b)** different irradiation at 25ºC **c/d)** different temperature at 1kW/m^2

4. Simulation Results

The system consisting of MPPT, power circuit and DTC blocks is performed by using MATLAB as shown in Figure 12. MPPT algorithm determines the speed demanded for the operation of the SynRM by calculating MPP. Thus, the SynRM can be operated at the MPP via DTC. The simulation blocks are separated as digital and real systems to obtain close to real results. The sample time of the digital system is taken as 10 μs. The real system simulation blocks have 1 μs sample time. Therefore, the separated systems are connected via rate-transition block which is supported with MATLAB.

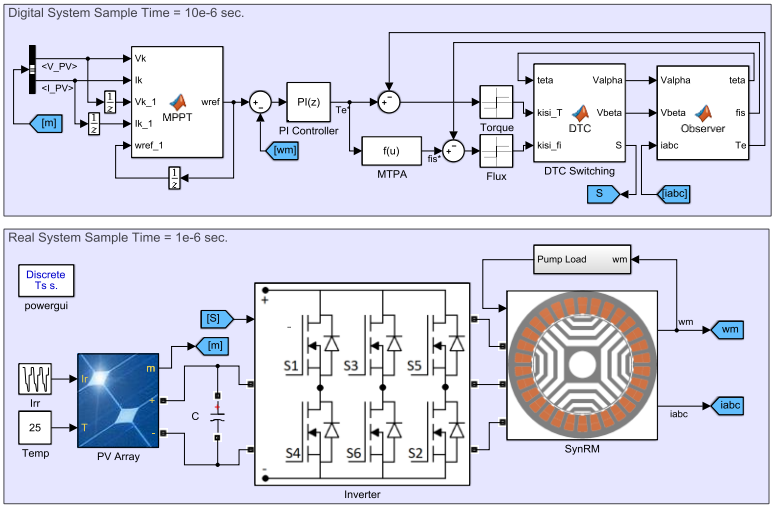

Figure 12. Control blocks of SynRM directly fed PV panel with MPPT algorithm

The system is tested for different irradiation conditions to analyze motor drive system having MPPT algorithm. Voltage, current and power of the PV panel have changed according to variation of the irradiation value at 25°C as shown in Figure 13 and Figure 14. The power of the motor must be reduced as PV panel power decreases. For this reason, the motor control system must be aware of these variable conditions. If this is not achieved, the motor synchronization will fail because enough power is not provided to motor. The results are illustrated to show the performance of the motor, DTC and MPPT under 25°C temperature and variable irradiation conditions in Figure 13.

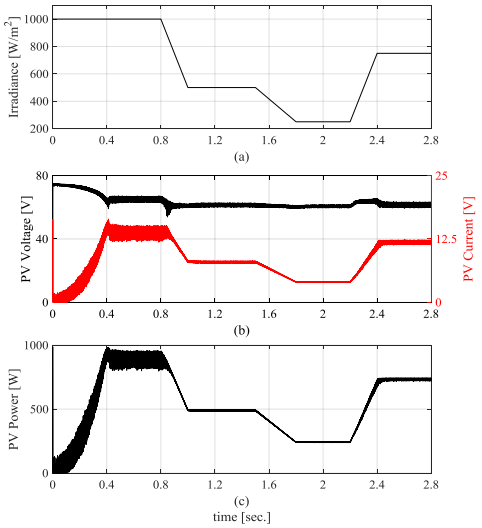

Figure 13. a) Irradiation conditions, **b)** I and V curves, **c)** PV Power

Three-phase stator currents, speed and electromagnetic torque of the motor are analyzed. Three-phase currents, nominal speed, frequency and produces torque of the motor are decreased when irradiation value decreases and vice versa. The detailed current waves are given in Figure 14a. It can be seen that the frequencies of the currents are changed according to motor reference speed. The motor speed is changed by the MPPT algorithm and the desired power rating of the motor is provided from the PV panels when the irradiation conditions change. In this study, the load torque is proportionally adjusted by motor speed.

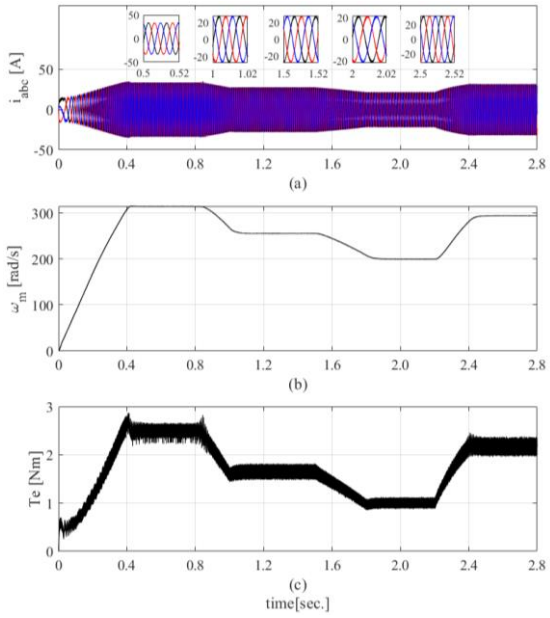

Figure 14. a) Stator currents**, b)** Motor speed, **c)** Electromagnetic torque

5. Conclusion

The majority of electrical energy is consumed by electric motors in industrial and other applications. The pump motor is the overriding of motor types used in industry. The increasing of pump motor efficiency plays an important role in the total energy consumption. The pump speed is so an important parameter to obtain high efficiency in the pump systems. Induction motors have lower speed than synchronous motors under the same conditions because induction motors have a slip between the angular speed of generated magnetic field and angular speed of the rotor. Therefore, using a synchronous motor is a better solution than an induction motor in order to obtain high speed and efficiency for pump systems.

In this paper, a SynRM and a drive system were developed as an alternative to the available systems to provide maximum benefit from the solar energy which is a renewable energy source. Firstly, 9 different motor were designed for this purpose. Rotor shapes of the designed 9 different motors are different each other while stator structures of these motors are same. Then, the effects of rotor shape were analyzed with 9 different rotor types. Barriers and rips of the rotor were changed in order to show the effect on the motor performance of rotor shape and performance curves of the designed motor were analyzed. As a result of the analysis, motor producing 2.3 Nm was selected for this study. Effects of advance angle on designed motor performance were analyzed and advance angle was selected as 54°for this motor. Output power, efficiency and torque of this motor are 715W, 86.4% and 2.3 Nm at rated speed. DTC and MPPT algorithms were used for motor drive system and 3-phase current, angular speed and torque have been analyzed. The efficiency of the designed SynRM is about 86% while the efficiency of a commercial 3-phase induction motor is about 71% for pump. Additionally, the stack length of the designed motor was obtained as 110 mm while stack length of the induction motor is 150 mm for the standard pump motor. Advantages of this work are given as follows; increasing efficiency of the solar pump system, reducing length of the stator stack according to induction motor, eliminating copper losses of the rotor, reducing the cost of the system, reducing the amount of devices (boost converter, magnet, battery, charger) used in the traditional pump systems. Consequently, a novel design is proposed as an alternative system to the low power solar pump systems instead of the traditional systems in this study.

Appendix A

dq-parameters of designed SynRM

K_t (Torque over RMS phase current) 0 N.m/A, L_d (d-axis inductance) 2.1 mH, L_q (q-axis inductance) 0.561 mH, L_d/L_q (aligned/unaligned) 3.74, L average1.33 mH, R_s (Stator phase resistance) 0.0602 Ω, I_{rms} (RMS current) 23.

Appendix B

Motor parameter values

Supply voltage 50 V, Rated current 23 A, Rated speed 3000 rpm, Rated frequency 100 Hz, Pole number 4, Number of phases 3, Number of slots 30, Outer diameter of the stator 90 mm, Air gap thickness 0.5 mm, Stack height 110 mm, Outer diameter of the rotor 60 mm, Inner diameter of the rotor 18 mm.

Acknowledgment

The authors would like to thank The Scientific and Technological Research Council of Turkey (TUBITAK) for financial support (Project No: 116E116)

References

[1] Kostko JK. Polyphase reaction synchronous motors. J Am Inst Electr Eng 1923; 42: 1162–1168.
[2] Lagerquist R, Boldea I, Miller TJE. Sensorless-control of the synchronous reluctance motor. IEEE Trans. Ind. Appl 1994; 30: 673-682.
[3] Xu L, Xu X, Lipo TA, Novotry DW. Vector Control of a Synchronous Reluctance Motor Including Saturation and Iron Loss. IEEE Trans Ind Appl 1991; 27: 977–985.
[4] Deniz E. ANN-based MPPT algorithm for solar PMSM drive system fed by direct-connected PV array. Neural Comput Appl 2017; 28: 3061–3072.
[5] Gündoğdu A, Güre B. Design, Construction and Implementation of Low Cost Photovoltaic Water Pumping System for Agricultural Irrigatin. Balk J Electr Comput Eng 2019:72–80.
[6] Aydogmus O. Design of a solar motor drive system fed by a direct-connected photovoltaic array. Adv Electr Comput Eng 2012; 12: 53–58.
[7] Kumar R, Singh B. Solar photovoltaic array fed water pump driven by brushless DC motor using Landsman converter. IET Renew Power Gener 2016; 10: 474–484.
[8] Aydogmus O, Deniz E, Kayisli K. PMSM Drive Fed by Sliding Mode Controlled PFC Boost Converter. Arab J Sci Eng 2014; 39: 4765–4773.
[9] Celikel R, Aydogmus O. A torque ripple minimization method for brushless DC motor in high speed applications using buck boost topology. J Eng Res 2019; 7: 200–214.
[10] Xu L, Xu X, Lipo TA, Novotry DW. Vector Control of a Synchronous Reluctance Motor Including Saturation and Iron Loss. In: Conference Record of the 1990 IEEE Industry Applications Society Annual Meeting; 7-12 Oct. 1990; Seattle, USA: IEEE. pp. 1–13.
[11] Piegari L, Rizzo R. Adaptive perturb and observe algorithm for photovoltaic maximum power point tracking. IET Renew Power Gener 2010; 4: 317-328.
[12] Femia N, Petrone G, Spagnuolo G, Vitelli M. Optimizing sampling rate of P&O MPPT technique. In: PESC Rec. - IEEE Annu. Power Electron. Spec. Conf., 20-25 June 2004; Aachen, Germany. pp. 1945–1949.
[13] Esram T, Chapman PL. Comparison of Photovoltaic Array Maximum Power Point Tracking Techniques. IEEE Trans Energy Convers 2007; 22: 439–449.
[14] Gao J, Wu X, Huang S, Zhang W, Xiao L. Torque ripple minimisation of permanent magnet synchronous motor using a new proportional resonant controller. IET Power Electron 2017; 10: 208–214.
[15] Shukla S, Singh B. Solar powered sensorless induction motor drive with improved efficiency for water pumping. IET Power Electron 2018; 11: 416–426.
[16] Hussein KH, Muta I, Hoshino T, Osakada M. Maximum photovoltaic power tracking: an algorithm for rapidly changing atmospheric conditions. Gener Transm Distrib IEE Proceedings- 1995; 142: 59–64.
[17] Gundogdu A, Dandil B, Ata F. Asenkron Motorun Histeresiz Denetleyici Tabanlı Doğrudan Moment Denetimi. Fırat Üniversitesi Mühendislik Bilim Derg 2017; 29: 197-205.
[18] Rahim NA, Che Soh A, Radzi MAM, Zainuri MAAM. Development of adaptive perturb and observe-fuzzy control maximum power point tracking for photovoltaic boost dc–dc converter. IET Renew Power Gener 2014; 8: 183–194.
[19] Rizzo SA, Scelba G. ANN based MPPT method for rapidly variable shading conditions. Appl Energy 2015; 145: 124–132.
[20] Elobaid LM, Abdelsalam AK, Zakzouk EE. Artificial neural network-based photovoltaic maximum power point tracking techniques: a survey. IET Renew Power Gener 2015; 9: 1043–1063.
[21] Noguchi T, Togashi S, Nakamoto R. Short-current pulse-based maximum-power-point tracking method for multiple photovoltaic-and-converter module system. IEEE Trans Ind Electron 2002; 49: 217–223.

[22] Staton DA, Miller TJE, Wood SE. Maximising the saliency ratio of the synchronous reluctance motor. IEE Proc B Electr Power Appl 1993; 140: 249-259.
[23] Lipo TA. Synchronous reluctance machines-a viable alternative for ac drives? Electr Mach Power Syst 1991; 19: 659–671.
[24] Kamper MJ, Van Der Merwe FS, Williamson S. Direct finite element design optimisation of the cageless reluctance synchronous machine. IEEE Trans Energy Convers 1996; 11: 547–553.
[25] Taghavi S, Pillay P. A Sizing Methodology of the Synchronous Reluctance Motor for Traction Applications. IEEE J Emerging Selected Topics in Power Elect. 2014; 2: 329-340.
[26] Ferrari M, Bianchi N, Doria A, Fornasiero E. Design of Synchronous Reluctance Motor for Hybrid Electric Vehicles. IEEE Trans. Ind. Appl., vol. 51, 2015, p. 3030–40. https://doi.org/10.1109/TIA.2015.2410262.
[27] Truong PH, Flieller D, Nguyen NK, Mercklé J, Sturtzer G. Torque ripple minimization in non-sinusoidal synchronous reluctance motors based on artificial neural networks. Electr Power Syst Res 2016; 140: 37–45.
[28] Moghaddam RR. Synchronous Reluctance Machine (SynRM) Design. MSc, Royal Institute of Technology, Stockholm, 2007.

Turkish Journal of Science & Technology
15(2), 61-70, 2020

Design and Optimization of a PMSM for Obtaining High-Power Density and High-Speed

Gullu BOZTAS[1*], Merve YILDIRIM[2], Omur AYDOGMUS[3]
[1]Electrical and Electronic Engineering, Technology Faculty, Firat University, Elazig, Turkey
[2]Electrical-Electronic Engineering, Engineering Faculty, Firat University, Elazig, Turkey
[3]Mechatronics Engineering, Technology Faculty, Firat University, Elazig, Turkey
[*1]gboztas@firat.edu.tr, [2]merveyildirim@firat.edu.tr, [3]oaydogmus@firat.edu.tr

(Geliş/Received: 30/04/2020; Kabul/Accepted: 30/07/2020)

Abstract: It is very important to obtain high power in a small volume for many applications. Especially, power/weight (W/kg) ratio needs to be well balanced in electric and aircraft vehicles, military and robotic applications. High power density can usually be obtained with a magnet-assisted motor. However, it is very difficult in terms of design for the motor to have both high power and low weight. Therefore, motor design should be supported by a good optimization. In this study, Multi-Objective Genetic Algorithm (GA) is used to obtain high power and low weight. Thus, targets are achieved by both optimizations at the same time. Rotor inner diameter, stack length, magnet insert, magnet thickness, and magnet angle are optimized in this paper. The motor is designed as 24 slots and 16 poles. 1100 generations are obtained by optimization and it has been decided that 1092th generation is the most suitable motor. Hence, motor having approximately 8 kW output power and 1.3 kg rotor mass is designed. The motor efficiency is obtained about 97% when friction and ventilation losses are neglected. As a result, it is observed that designed PMSM with high-power density and high speed can be used in the robotic and military applications.

Key words: Optimization, High Power Density, Genetic Algorithm, Motor Design, Permanent Magnet Synchronous Motor.

Yüksek Güç Yoğunluğu ve Yüksek Hız elde etmek için PMSM'nin Tasarımı ve Optimizasyonu

Öz: Birçok uygulama için küçük bir hacimde yüksek güç elde etmek oldukça önemlidir. Özellikle, elektrikli ve hava araçlarında, askeri ve robotik uygulamalarda güç/ağırlık (W/kg) oranının iyi dengelenmesi gerekmektedir. Yüksek güç yoğunluğu genellikle mıknatıs destekli bir motor ile elde edilebilir. Ancak motorun hem yüksek güce sahip, hem de düşük bir ağırlığa sahip olması tasarım açısından oldukça zordur. Bu yüzden iyi bir optimizasyon destekli tasarıma ihtiyaç duyulmaktadır. Bu çalışmada, yüksek güç ve düşük bir ağırlık elde etmek için Çok Amaçlı Genetik Algoritma kullanılmıştır. Böylece her iki optimizasyon hedefine aynı anda ulaşılması sağlanmıştır. Rotor iç çapı, paket boyu uzunluğu, mıknatıs derinliği, mıknatıs kalınlığı ve mıknatıs açısı bu makalede optimize edilmiştir. Motor 24 oluklu ve 16 kutuplu olarak tasarlanmıştır. Optimizasyon ile 1100 adet jenerasyon sonunda 1092. jenerasyonun en uygun motor olduğuna karar verilmiştir. Böylece yaklaşık 1,3 kg rotor ağırlığına ve yaklaşık 8 kW çıkış gücüne sahip bir motor tasarlanmıştır. Sürtünme ve vantilasyon kayıpları ihmal edildiğinde motor verimi %97 civarında bir verim elde edilmiştir**.**

Anahtar kelimeler: Optimizasyon, Yüksek Güç Yoğunluğu, Genetik Algoritma, Motor Tasarımı, Kalıcı Mıknatıslı Senkron Motor.

1. Introduction

In recently, Permanent Magnet Synchronous Motors (PMSMs) have been popular in many areas such as aerospace, automotive industry especially electric vehicles, and robots due to its high efficiency, fast torque response, and high power density [1–3]. Optimization methods in this motor design are also significant research areas. Especially, the design optimization of the PMSM has great importance in terms of the cost and energy saving [4]. Therefore, there are a lot of studies about this topic in the literature. First of all is optimal design of axial-flux PMSM by using GA in [5]. Air gap, permanent magnet flux density, current density and number of stator winding turns are examined by GA optimization method. Maxwell 3D analysis based on Finite Element Method (FEM) is realized to compare the design and optimization results. It is observed from the simulation results that a rms current value and copper loss causing the motor temperature at the rated torque are significantly decreased by reducing the input voltage. By using GA optimization, a five-phase slotless PMSM with an external rotor is designed for high torque density in [6]. A higher torque density for PMSM can be provided by having a trapezoidal back EMF. For this reason, back EMF waveform is optimized by a multi-objective GA optimization based on the analytical

* Corresponding author: gboztas@firat.edu.tr. ORCID Number of authors: [1] 0002-1720-1285, [2] 0003-1284-7324, [3]0001-8142-1146

model. FEM analysis is realized to verify the analytical results. Then, a prototype of the designed PMSM is manufactured and FEM analysis and analytical results are validated by the experimental results.

In [7], optimal design of PMSM is presented by utilizing GA to obtain high efficiency and low permanent magnet weight at the rated load and speed. Multi-objective functions in GA are taken as the sum of the PMSM efficiency and the inverse value of the permanent magnet total weight. After that, two PMSM models are handled and FEM analyses of the PMSMs are performed by comparing each other. Convenient motor model is selected to validate the PMSM design with GA. Authors in [8] propose an optimal GA design of PMSM with low speed and high torque used in unmanned ground vehicle. Maximum efficiency is selected as object function in GA. Stator and rotor lamination structures and stator windings are designed. The size of permanent magnet and the length of air gap are calculated. Then, the PMSM is analyzed by FEM solution. PMSM design without optimization is compared with that of the GA optimization method.[9] explains an optimal design of in-wheel PMSM by using GA to obtain high efficiency and low weight. The current density, the length ratio, the inductions in the air gap and stator teeth, stator yoke, and rotor core are taken as design parameters in the optimization. As a result, in-wheel PMSM is optimized by GA method. An optimal design of a surface-mounted PMSM is studied by using improved GA with subdomain model for multi-objective in [10]. The aim of this study is to improve the performance of surface-mounted PMSM in terms of the magnetic field distribution, efficiency, and cost and. Firstly, a subdomain model is created for the analysis of the flux density harmonics. After that, the multi-independent-population GA with time-saving subdomain model is designed for the Pareto optimal set solutions. Finally, FEM analysis of the optimized PMSM is realized and the optimized design results are compared with the first design results.

The rotor structure of PMSM is optimized by GA in [11]. Two kinds of stator windings and two types of current driving methods are examined for designing the rotor structures. It is seen that the PMSM having the best rotor structure has the largest average torque. A novel nine-phase PMSM with consequent pole rotor is designed for high-power traction applications in [12]. Multi-phase PMSMs are used in special areas desired higher torque/power density. The constant power–speed range of this motor is quite wide rather than the conventional PMSMs. FEM analysis of the motor is realized and the performance of nine-phase PMSM with consequent pole rotor is compared with a nine-phase surface mounted PMSM. It is observed that the proposed motor has simpler rotor structure and lower magnet cost and temperature than the surface mounted PMSM. In [13], the design of the high power-density PMSM and driving system is studied. The control parameters are given in the design and the system stability is researched. Then, FEM analysis of the PMSM is realized and the analysis results are compared with the experimental results in terms of the back-emf and the efficiency. It is obtained from the results that the high power density driving system is proper for the areas with high-performance required high speed. High power density PMSM with high electromagnetic load and lightweight structure is studied in [14]. However, there is a drawback about the iron core material to obtain high magnetic load and lightweight structure is only utilized in the rotor design. Four topologies are used to examine the lightweight structure applied in the stator for reducing the total weight. Besides, the high performance soft magnetic alloy core is preferred for high power density PMSM. The proposed method is validated by comparing the electromagnetic performances of four motors.

Design and optimization of high power density PMSM with surface mounted magnet is explained for pod propulsion system in [15]. Some constraints related with the dimensions of PMSM, the maximum acceptable current density, and the non-saturable operation conditions are considered in the design. After that, the PMSM is analyzed by FEM and it is seen that it has high efficiency and power factor, non-saturable operation, low current density, cogging torque and torque ripple. The optimized design results are also compared with the other studies in the literature. Authors in [16] propose a high power density PMSM drive design with flooded stator cooling. The aim of the study is to increase the efficiency and reduce the volume of the drive. The magnet losses and AC losses are also important problems in the PMSMs. Hence, the magnets are axially segmented to decrease the magnets losses caused from the harmonics. As a result, the efficiency of the PMSM is increased by this way. A paper [5] presents an optimization of an axial-flux PMSM design at high speed. PMSM is optimized by using GA for optimal design of the because of the demanded torque with minimum current and copper losses, and dimensions. The optimum value of the air gap, permanent magnet flux density, current density, and the number of stator winding turns are determined by GA. Maxwell 3D model of the PMSM based on FEM is created to compare the analytical results and optimization results. According to the simulation results, it is seen that the rms current value and the copper losses at rated torque reduce significantly.

In this study, the rotor structure of the PMSM is optimized in order to obtain high power density at high speeds with low rotor mass. Both the output power of the motor should be increased and the motor weight should

be decreased in order to achieve high power density. However, it is quite difficult to achieve this desired situation. Therefore, Multi-objective GA was used for the optimization in order to increase torque and reduce the rotor mass.

2. Mathematical Model of the PMSM

Dynamic equivalent circuits of the motor are presented in Figure 1 [17].

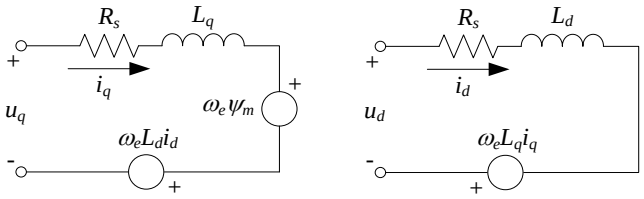

Figure 1. Equivalent circuit of a PMSM.

Voltage equations are obtained shown as Equation (1). Additionally, The linkage fluxes are shown in Equations (2)-(3).

$$\begin{bmatrix} u_d(t) \\ u_q(t) \end{bmatrix} = \begin{bmatrix} R_s & 0 \\ 0 & R_s \end{bmatrix} \begin{bmatrix} i_d(t) \\ i_d(t) \end{bmatrix} + \begin{bmatrix} 1 & 0 \\ 0 & 1 \end{bmatrix} \begin{bmatrix} \dot{\psi}_d(t) \\ \dot{\psi}_q(t) \end{bmatrix} + \begin{bmatrix} -\omega_e & 0 \\ 0 & \omega_e \end{bmatrix} \begin{bmatrix} \psi_q(t) \\ \psi_d(t) \end{bmatrix} \tag{1}$$

where, i_d and i_q are dq-axis currents. ω_e, R_s, ψ_d and ψ_q are the electrical rotor frequency, the stator winding resistance and linkage fluxes of dq-axis, respectively. ψ_m is the flux linkage due to the rotor magnets.

$$\psi_d = L_d i_d + \psi_m \tag{2}$$

$$\psi_q = L_q i_q \tag{3}$$

The electromagnetic torque equations are shown in Equations (4)-(5).

$$T_e = \frac{3}{2} p\left[\psi_d i_d - \psi_q i_q\right] \tag{4}$$

$$T_e = T_L + J\frac{d\omega_m}{dt} + B\omega_m \tag{5}$$

where, T_L, J, ω_m and B are the load torque , the inertia, the mechanical angular velocity of the rotor and the friction coefficient.

3-types rotor structure of the PMSM is given in Figure 2 according to placement on the rotor and different shape of magnets. PMSM having surface-mounted magnets is given in Figure 2a [17]. The stator inductance of this type motor is lower than the other rotor types. Therefore, control of the surface-mounted PMSM is simple. Additionally, the reluctance effect of the motor is small enough to neglect. However, field weakening and speed control over the nominal value are so difficult for this motor. The interior-mounted rotor structure is shown in Figure 2b. Stator inductance depends on rotor position in this type motor. The operation of over nominal speed is suitable for this motor type because reluctance torque is obtained during field weakening. Additionally, durable structure is mechanically obtained in high speed applications when the magnets are placed embedded in the rotor. Buried magnet PMSM is given in Figure 2c. Flux condensation can be obtained with buried magnets given in Figure 2c. Flux density in the air gap is higher compared to that of the magnet in the buried magnet PMSM. In

this study, interior mounted PMSM was designed and optimized for high speed applications. It is a motor that can be used in military applications, robotics and some industrial applications where high power density is important.

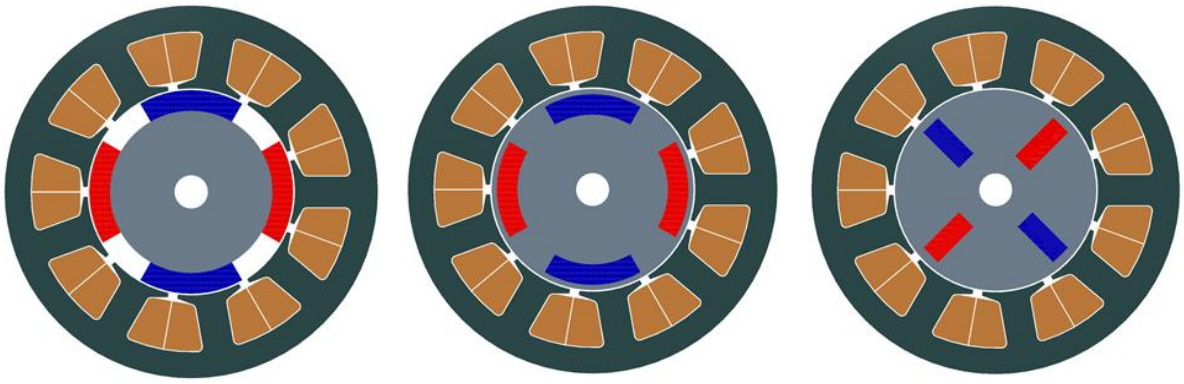

Figure 2. a) Surface-mounted PMSM, b) Interior mounted PMSM, c) Buried magnet PMSM.

3. Design and Optimization of the PMSM

In this study, an interior-mounted PMSM having 16 poles, 3 phases and 30 slots was designed by using MotorSolve/Infolytica program. Stator geometry, rotor outer radius, winding layout and pole number of the motor were kept constant for optimization. The materials of the stator and rotor cores were used as M530-50A. Values of motor parameters taken as constant are given in Table1. Rotor inner diameter, stack length, magnet insert, magnet thickness, and magnet angle were optimized in this paper. It is aimed to obtain maximum motor torque with minimum rotor mass in optimization progress. Thus, high power density motor will be obtained. Definition of the optimized motor parameters are shown in Figure 3.

Two fitness functions used for optimization are given in Equations (6)-(7). The fitness functions are optimized together by using MATLAB Genetic Algorithm toolbox and Multi-Objective Genetic Algorithm. The fitness functions were used in order to obtain maximum motor torque and the minimum motor mass. PMSM was analyzed using the Finite Element Method (FEM) -Newton Raphson iteration in the MAGNET program during the optimization steps The performance analyses of the Multi-Objective Genetic Algortihm are given in Figure 4. Each circle in the figure symbolizes an individual. During the optimization process, the motor torque was maximized as shown in Figure 4a. However, the rotor mass was slightly minimized as illustrated in Figure 4b because it is difficult to produce high torque with small rotor mass. 1092. iteration was determined for this study. Additionally, The change in the progress between motor torque-rotor mass is given in Figure 4c.

Table1. Values of motor parameters

Parameter	Value	Parameter	Value
pole	16	slot opening width	1 mm
number of slot	36	tooth tip thickness	1 mm
stator outer radius	55 mm	tooth width	3.5 mm
stator inner radius	35.5 mm	bottom fillet radius	0
air gap	0.5 mm	top fillet radius	0
slot depth	15 mm	number of turn	6

$$fitness(1) = -\overline{T_e} \tag{6}$$

$$fitness(2) = M_{rotor} \tag{7}$$

where $\overline{T_e}$ is average electromagnetic torque of the motor. The reason used negative torque in the function is to

convert minimization of optimization to maximization. M_{rotor} is mass of the rotor.

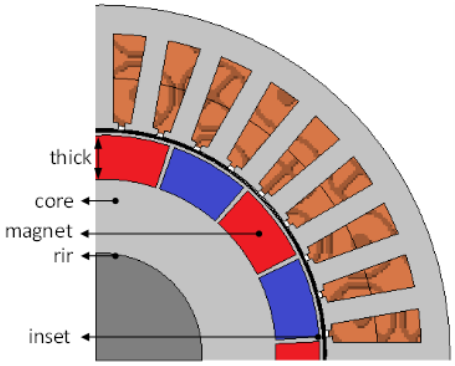

Figure 3. Definition of optimized motor parameter.

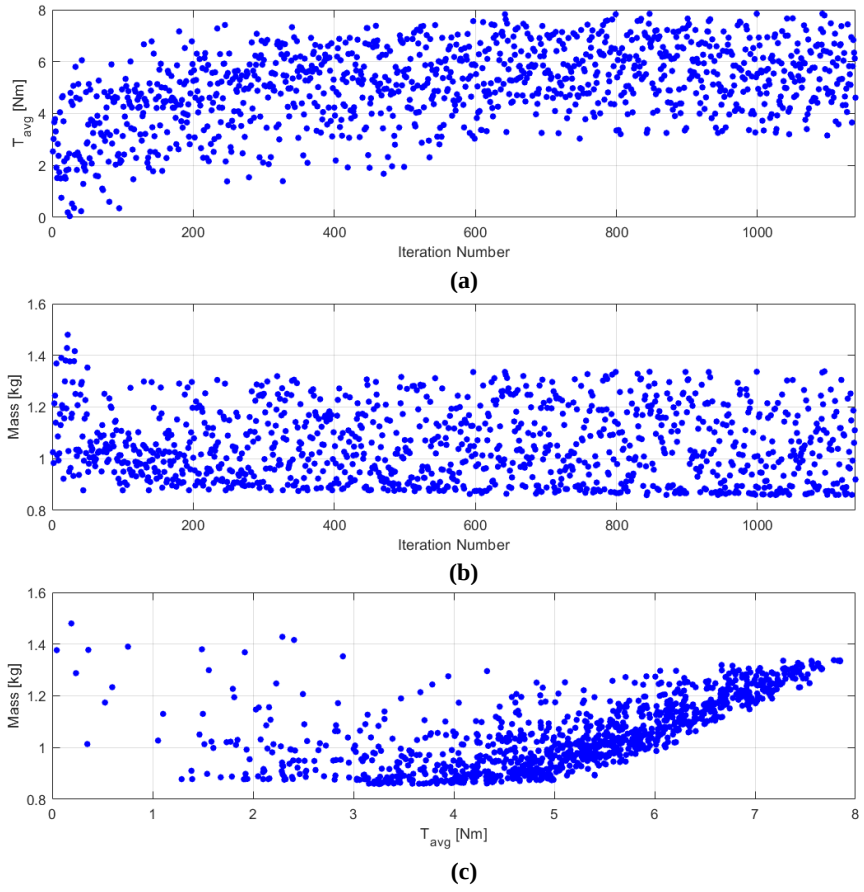

Figure 4. Performance analyses of the Multi-Objective Genetic Algorithm **a)** Motor torque, **b)** Rotor mass, **c)** Motor torque/Rotor mass.

The analysis results about variations in the motor power according to optimized parameters are illustrated in Figure 5. Rotor inner diameter, stack length, magnet insert, magnet thickness, and magnet angle were optimized in this study. The maximum and minimum values of the parameters to be optimized are determined as shown in Table 2 before starting the optimization step. Additionally, optimized motor parameters are given in Table 2. The rotor inner radius is optimized between 12 and 18 mm as shown in Figure 5a. High motor output power was obtained between 15 and 16 mm and the optimized rotor inner radius was chosen as 15.799 mm. It is seen that the

motor output power increases as the stack length increases when the region where the individuals is concentrated are analyzed as given in Figure 5b. However, the mass of the motor increases when the stack length of the motor increases. Therefore, the motor stack length is limited between 40 and 60 mm before optimization steps. The output power decreases as magnet inset depth increases as given in Figure 5c and optimized magnet inset depth is 0.539 mm. Individuals concentrate in the region where the power increased as given in Figure 5d and optimized magnet thick are 6.917 mm. It can be seen that the output power of the motor increases when the magnet angle increases when the region where the individuals is concentrated are analyzed as given in Figure 5e. A combination of motor torque, rotor mass and motor output power are presented in 3D is given in Figure 5f. Additionally, the stator and rotor structures of the optimized PMSM are given in Figure 6.

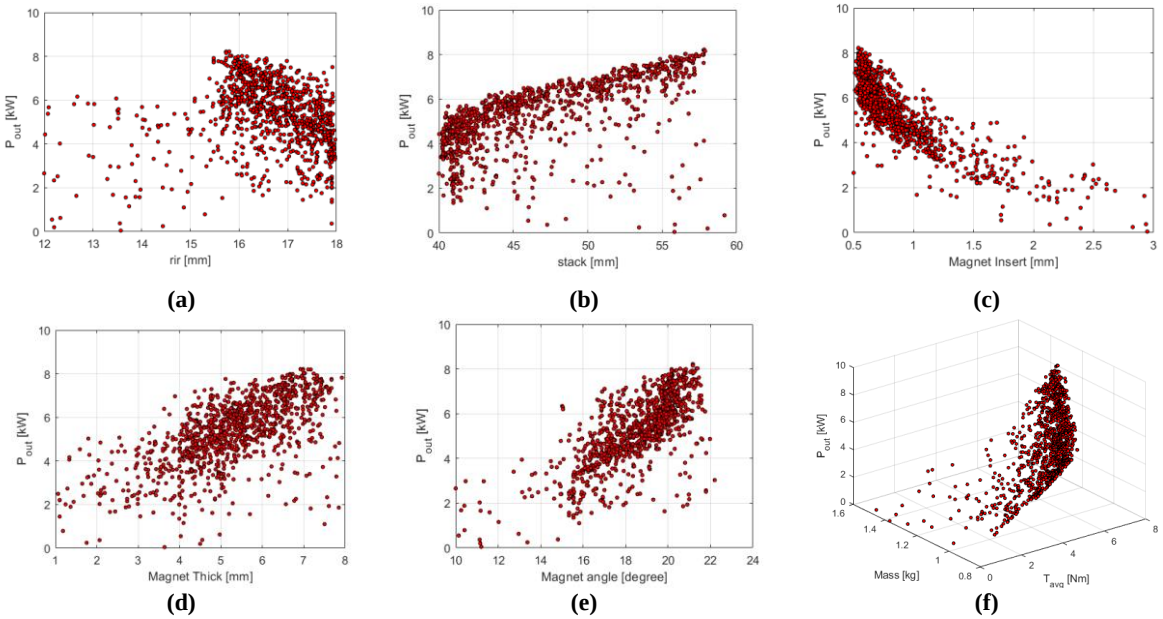

Figure 5. a-e) Change of optimization parameters according to output power, **f)** combination of motor torque, rotor mass and motor output power.

Table 2. Parameters of the optimized motor.

Parameter	Min. value	Max. value	Optimized Value
rotor inner radius	12 mm	18 mm	**15.799 mm**
stack	40 mm	60 mm	**57.816 mm**
magnet inset depth	0.5 mm	3 mm	**0.539 mm**
magnet thickness	1 mm	8 mm	**6.917 mm**
magnet angle	10°	22.5°	**21.168°**

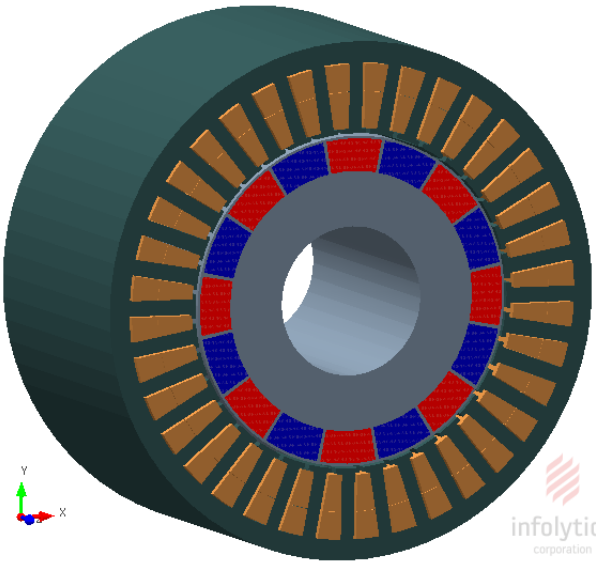

Figure 6. Stator and rotor structures of the optimized PMSM.

The mesh and solid view and flux density distribution of the optimized motor are shown in Figure 7. PMSM was analyzed using the Finite Element Method (FEM) -Newton Raphson iteration in the MAGNET program during the optimization steps. The maximum flux density of the motor in stator tooth and stator yoke is nearly 2.579 T.

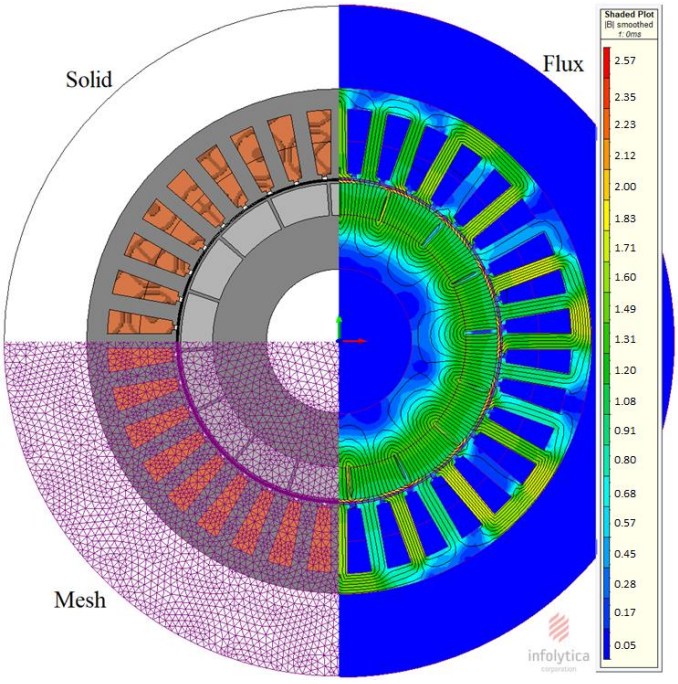

Figure 7. Mesh and solid view and flux density distribution of the optimized motor.

The back-EMF curve of the motor according to motor electric angle are shown in Figure 8a. A stator with a harmonic content in Figure 8b was obtained by selecting the stator 24 slots and 16-pole. It can be said that a suitable winding layout was chosen when analyzing the harmonic content.

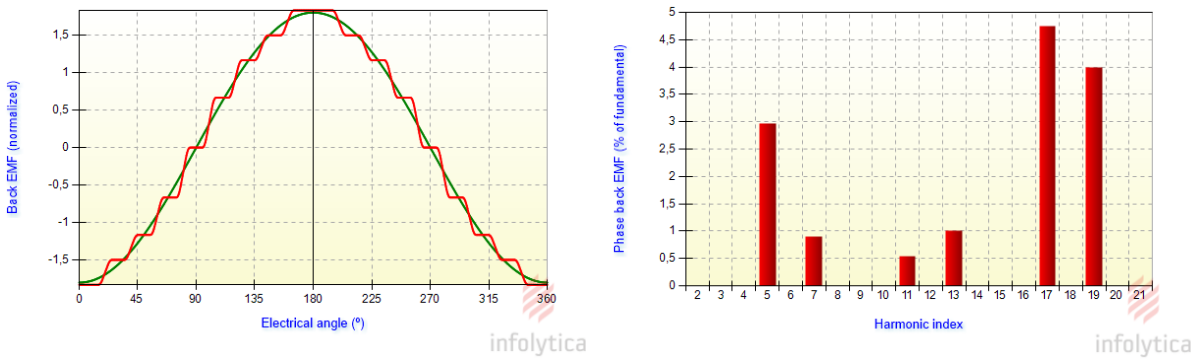

(a) **(b)**

Figure 8. a) back-EMF (normalized) of motor, **b)** Harmonic content for winding layout.

The curves of torque, output power, efficiency and power factor are analyzed in Figure 9 by using MotorSolve/Infolytica program. The rated speed of the motor is 10000 rpm and the motor frequency is 1333.33 Hz. The motor is operated in the constant torque region by using Pulse Width Modulation (PWM) bridge switched 10 kHz frequency. When the results are examined, there are small differences between MotorSolve and MAGNET. This is due to the fact that the analysis was carried out with an ideal source in MAGNET and PWM in MotorSolve. The motor torque is kept up about 8.80 Nm from standstill to steady-state operation. The output power of the motor is 9.24 kW at 10000 rpm. The motor efficiency is obtained as 96.8% without the friction and ventilation losses at the rated speed. Additionally, the motor power factor is 0.848 at 10000 rpm and the rated current of the motor is 15 A.

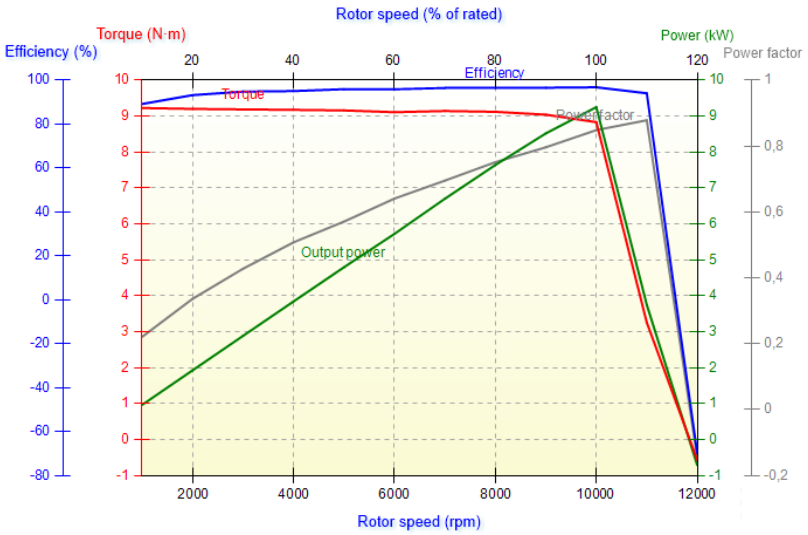

Figure 9. Torque, output power, efficiency and power factor of the optimized motor.

The efficiency map of the designed motor is given in Fig. 10. The efficiency decreases as the motor speed decreases at the same load torque. The efficiency of the motor is above 90% at load torque above 1.5 Nm and at rated speed. The optimized motor has an efficiency of approximately 97-98% at load torque above 5.8 Nm and at the motor rated speed.

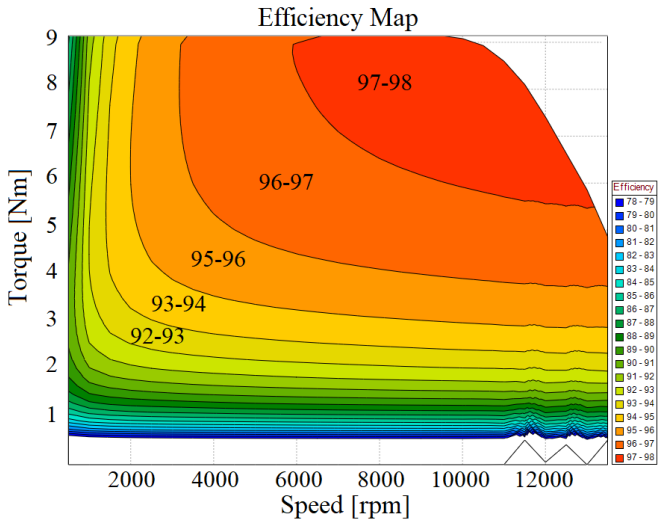

Figure 10. Efficiency map of the optimized PMSM.

4. Conclusion

The high output power and the low motor mass are desired from the motors that will be used in robotic, military and some industrial applications. Reactive power requirements of the PMSMs are as low as possible since these motors have magnets in their rotors. Therefore, it is possible to obtain much higher power density with PMSMs compared to other AC motors. Different performances can be obtained by depending on the geometry and position of the magnets used in this motor type. A PMSM having high power density is designed in this study. After the motor winding layout and stator geometry are analyzed by the MotorSolve Software, the PMSM is optimized by FEM developing an intermediate program that enables MATLAB and MAGNET Software to work together. The GA and FEM are run by MATLAB and MAGNET Software, respectively. A loop is created by giving the geometric parameters determined by MATLAB into the MAGNET Software and obtaining the motor torque and rotor weight by motion analysis and sending them to the MATLAB Software again. The number of the stator slot and pole of the PMSM are determined as 24 and 16, respectively. By keeping the stator geometry of this motor constant, an optimization study is performed on the rotor geometry. The optimization is realized by the aim of high torque and low rotor weight to obtain the desired motor by using the Multi-Objective GA method. By optimizing the rotor inner diameter, package length, magnet depth, magnet thickness, and magnet angle, the best rotor geometry is obtained as a result of a total of 1100 generations. It is observed from the optimization analysis results that the torque of the motor increases and the weight of the rotor decreases. However, it is not possible to decrease the rotor weight as the motor torque increases. Since the majority of the rotor consists of iron cores and magnets, reducing the weight is quite difficult. While the rotor weight varies between 0.9-1.4 kg, the motor torque is obtained in the range of 1-8 Nm in different generations. As a result of the optimization, it is decided that 1092th generation is the most proper motor. Thus, approximately 8 kW power could be obtained at a speed of 10.000 rpm for approximately 1.3 kg rotor weight. The package length of the optimized PMSM is obtained as 57.8 mm which is a very small value. The efficiency of the motor is also obtained as around 97% by neglecting the friction and ventilation losses. It has remained above 90% at all speed values. Therefore, it can be seen that the sizes of this designed PMSM are convenient for the robotic and military purposes.

References

[1] Zhong L, Rahman MF, Hu WY, Lim KW. Analysis of direct torque control in permanent magnet synchronous motor drive. IEEE Trans Power Electron 1997; 12(3): 528–536.

[2] Yildirim M, Polat M, Kurum H. A survey on comparison of electric motor types and drives used for electric vehicles. In 2014 16th International Power Electronics and Motion Control Conference and Exposition; 21-24 Sept. 2014; Antalya, Turkey, pp. 218–223.

[3] Yildirim M, Kurum H, Miljavec D, Corovic S. Influence of Material and Geometrical Properties of Permanent Magnets on Cogging Torque of BLDC. Engineering, technology & amp; applied science research 2018; 8(2): 2656-2662.

[4] Mutluer M, Bilgin O. Design optimization of PMSM by particle swarm optimization and genetic algorithm. In 2012

International Symposium on Innovations in Intelligent Systems and Applications; 2-4 July2012;Trabzon,Turkey, pp.1–4.
[5] Seadati SAS, Niasar AH. Optimal design and finite element analysis of a high speed, axial-flux permanent magnet synchronous motor. In 2018 9th Annual Power Electronics, Drives Systems and Technologies Conference; 13-15 Feb. 2018; Tehran, Iran, pp. 133–138.
[6] Sadeghi S, Mohammadpour A, Parsa L. Design optimization of a high performance five-phase slotless PMSM. In 2014 International Symposium on Power Electronics, Electrical Drives, Automation and Motion; 18-20 June 2014; Ischia, Italy, pp. 6–11.
[7] Cvetkovski G, Petkovska L. Multi-objective optimal design of permanent magnet synchronous motor. In 2016 IEEE International Power Electronics and Motion Control Conference; 25-28 Sept. 2016; Varna, Bulgaria, pp. 605–610.
[8] Zhu, W, Yu Z, Zhou W, Shi J, Yin Y. Design of permanent magnet synchronous motor based on genetic algorithm in unmanned ground vehicles. In 2017 IEEE International Conference on Unmanned Systems (ICUS); 27-29 Oct. 2017; Beijing, China, pp. 572–575.
[9] Hejra M, Mansouri A, Trabeisi H. Optimal design of a permanent magnet synchronous motor: Application of in-wheel motor. In 2014 5th International Renewable Energy Congress; 25-27 March 2014; Hammamet, Tunisia, pp. 1–5.
[10] Gao J, Zhang W. Improved genetic optimization algorithm with subdomain model for multi-objective optimal design of SPMSM. -CES Journals & Magazine 2018; 20(1): 160-165.
[11] Ishikawa T, Nakayama K, Kurita N, Dawson FP. Optimization of Rotor Topology in PM Synchronous Motors by Genetic Algorithm Considering Cluster of Materials and Cleaning Procedure. IEEE Trans Magn 2014; 50(2): 637–640.
[12] Onsal M, Demir Y, Aydin MA. New Nine-Phase Permanent Magnet Synchronous Motor With Consequent Pole Rotor for High-Power Traction Applications. IEEE Trans Magn 2017; 53(11): 1–6.
[13] Lei Z, Xuhui W, Jian Z, Youlong W. Research of high power-density permanent magnet synchronous motor and driving system. In 2011 International Conference on Electric Information and Control Engineering; 15-17 April 2011; Wuhan, China, pp. 6052–6055.
[14] Fang S, Liu H, Wang H, Yang H, Lin H. High power density PMSM with lightweight structure and high-performance soft magnetic alloy core. IEEE Trans App. Supercond 2019; 29(2): 1-5.
[15] Chasiotis ID, Karnavas YL. A Study on Design and Optimization of High Power Density PMSM for Pod Propulsion System. In 2018 XIII International Conference on Electrical Machines; 3-6 Sept. 2018; Alexandroupoli, Greece, pp. 534–540.
[16] Ullah S, Winterborne D, Lambert SM. Next-generation integrated drive: A high power density permanent magnet synchronous drive with flooded stator cooling. J Eng 2019; 2019(17): 4231–4235.
[17] Aydogmus O, Boztas G. Control and design of a high power density PMSM. Mechatronics 2017; 644: 273-280.

Turkish Journal of Science & Technology
15(2), 71-78, 2020

On the Robust Estimations of Location and Scale Parameters for Least Informative Distributions

Mehmet Niyazi ÇANKAYA[1*]
[1] Department of International Trading and Finance, Applied Science School, Uşak University, Uşak, Turkey
[1]Department of Statistics, Faculty of Arts and Science, Uşak University, Uşak, Turkey
[*1] mehmet.cankaya@usak.edu.tr

(Geliş/Received: 12/02/2020; Kabul/Accepted: 09/05/2020)

Abstract: M-estimation as generalization of maximum likelihood estimation (MLE) method is well-known approach to get the robust estimations of location and scale parameters in objective function ρ especially. Maximum $\log_q$ likelihood estimation (MLqE) method uses different objective function called as $\rho_{\log_q}$. These objective functions are called as M-functions which can be used to fit data set. The least informative distribution (LID) is convex combination of two probability density functions f_0 and f_1. In this study**,** the location and scale parameters in any objective functions $\rho_{\log}$, $\rho_{\log_q}$ and $\psi_{\log_q}(f_0, f_1)$ which are from MLE, MLqE and LIDs in MLqE are estimated robustly and simultaneously. The probability density functions which are f_0 and f_1 underlying and contamination distributions respectively are chosen from exponential power (EP) distributions, since EP has shape parameter α to fit data efficiently. In order to estimate the location μ and scale σ parameters, Huber M-estimation, MLE of generalized t (Gt) distribution are also used. Finally, we test the fitting performance of objective functions by using a real data set. The numerical results showed that $\psi_{\log_q}(f_0, f_1)$ is more resistance values of estimates for μ and σ when compared with other ρ functions.
Key words: Least informative distributions, maximum $\log_q$ likelihood estimation method, robustness.

En Az Bilgilendirici Dağılımlar için Konum ve Ölçek Parametrelerinin Sağlam Tahminleri Üzerine

Öz: En çok olabilirlik tahmin (MLE) yönteminin genelleştirilmesi olarak M-tahmini, özellikle amaç fonksiyonda ρ konum ve ölçek parametrelerinin sağlam tahminlerini elde etmek için iyi bilinen bir yaklaşımdır. En çok $\log_q$ olabilirlik tahmini (MLqE) yönteminde $\rho_{\log_q}$ adı verilen farklı amaç fonksiyonu kullanır. Bu amaç fonksiyonlarına, veri kümesine uyması için kullanılabilen M-fonksiyonları denir. En az bilgilendirici dağılımlar, f_0 and f_1 olasılık yoğunluk fonksiyonlarının konveks kombinasyonudur. Bu çalışmada, MLqE'de LID, MLqE ve MLE yöntemleri ile herhangi bir amaç fonksiyonda $\rho_{\log}$, $\rho_{\log_q}$ ve $\psi_{\log_q}(f_0, f_1)$ konum ve ölçek parametreleri dayanıklı ve aynı anda tahmin edilmektedir. Dağılımın büyük bir çoğunluğu f_0 ve kontaminasyon dağılımı f_1 olmak üzere üstel kuvvet (EP) dağılımından seçilmektedir; çünkü EP, verilere verimli bir şekilde uyacak şekil parametresi α'ya sahiptir. Konum μ ve ölçek σ parametrelerini tahmin etmek için Huber M-tahmini, genelleştirilmiş t (Gt) dağılımının MLE'si de kullanılmıştır. Böylelikle, gerçek bir veri seti kullanarak amaç fonksiyonların uyum performansını test etmekteyiz. Sayısal sonuçlar aracılığı ile $\psi_{\log_q}(f_0, f_1)$ amaç fonksiyonu diğer ρ fonksiyonları karşılaştırıldığında, μ ve σ için tahminlerin daha fazla direnç değerine sahip olduğu gösterilmiştir.

Anahtar kelimeler: En az bilgilendirici dağılımlar, maksimum $\log_q$ olabilirlik tahmin yöntemi, dayanıklılık.

1. Introduction

In a dataset, it is possible to observe non-identical behavior. In other words, the working principle of a real world cannot be modeled by a hypothetical parametric model. Even if we assume that a dataset is a member of a parametric model with its true parameter values, a contamination into underlying distribution can be observed. In this case, robust estimation of true values of parameters of underlying distribution is a crucial role in the estimation theory. For this purpose, M-estimation method and the recently maximum $\log_q$ likelihood estimation method are commonly used by [1-9].

The deformed logarithms are member of fractional polynomial functions. However, as it is clearly known, the estimation is a process which performs the numerical integration. The numerical integration which is based on Riemann integration rule works on the difference principle [10]. These differences can be represented by functions. If we can accomplish to construct the neighborhood of a function, then we will be capable to make

* Corresponding author: mehmet.cankaya@usak.edu.tr. ORCID Number of authors: [1] 0000-0002-2933-857X

different forms of non-identicality in a dataset, which shows us that the functions in the M-estimation principle is not enough reach to model not only versatile forms of non-identicality but also the different values of parametric model which represents the underlying distribution. Thus, we can make a bridge to touch the non-identical case efficiently. M-estimation method is commonly used for the estimation of location and scale parameters, because the functions in this method can be appropriate for modeling datasets which accommodate with the structure of these functions. They are generally used for the estimations of location and scale parameters. The efficiency in the M-estimation method for the estimations of the different values of parameters of underlying distribution will be a deficiency, because the structure of function for the different values of parameters cannot be modeled efficiently. Then, the functions used to estimate some parameters cannot be successful for different values of parameters in the underlying distribution in the M-estimation method that is generalization of maximum likelihood estimation (MLE) [1-9].

M-estimation is used to produce robust estimators for parameters of a probability density (p.d.) function $f_0(x;\boldsymbol{\theta})$. M-estimators are defined through an objective functions minimizing $\rho(x;\boldsymbol{\theta}) = \sum_{i=1}^{n} \Lambda[f_0(x_i;\boldsymbol{\theta})]$ over $\boldsymbol{\theta}$ [1-4]. Here, Λ is a concave function that is capable of making one to one mapping from $f_0(x;\theta)$ to Λ. M-estimators are derived by fixed functions, such as Huber, Tukey, etc. LIDs are used to produce Huber, Tukey, etc [3,11]. MLE as a special case of M-estimation is a method for estimations of parameters in a p.d. function. It is based on logarithm and does not work properly to estimate parameters in a p.d. function efficiently and robustly when data set including outlier(s) are non identically distributed, therefore we will use function $\log_q$ that mimics MLE method [5,11,12]. In our proposition, the benefit of LIDs and a p.d. function in Λ is that one can propose the objective functions from arbitrary p.d. functions to get more precise estimators for parameters in p.d. functions. The more precision can be accomplished by the parameter q and also LID in MLqE method. In the M-estimation principle, there are different functions used to fit datasets. Computational stage in the M-estimation method should be adopted according to the differentiability property of functions such as generalized divergences and deformed logarithms. For this aim, M-estimations are optimized according to parameters by using the Genetic Algorithm (GA). Thus, the local points in the optimization for the objective functions based on M-estimation can be discarded as it is pointed out that GA convergences to global points [13,14].

The aim of this study is to obtain robust estimators of location μ and scale σ parameters for LID by using MLqE and to compare with the fitting performances of objective functions for the robust estimators obtained by MLE for Generalized t (Gt) distribution and Huber M-estimation [3,11]. While performing the robust estimation procedure, we aim to get the efficient estimators as well by using another well-known robust estimation method called as MLqE. We make a comparison among the objective functions or M-functions used in the robust M-estimation method if we add the outliers into real datasets. The main motivation in LID is based on the convex combination of two functions which are f_0 and f_1 representing the underlying and contamination distributions, respectively. We use EP distribution to apply the LID in MLqE, because EP distribution has a shape parameter α which can model the peakedness of function. So, the efficiency of estimators can be performed not only the used shape parameter with fixed values but also f_1 which will be responsible to model the outliers as well [11,15-16].

The organization of this paper is as follow: Section 2 gives the preliminaries about the maximum likelihood estimation method and its generalized forms. The LIDs in MLqE are introduced. Different objective functions which will be used to fit data are given. Section 3 introduces the information criteria (IC). Section 4 is devoted to numerical illustration. Conclusions are given in the last section.

2. Preliminaries

2.1. Maximum likelihood estimation method

As it is-well-known, MLE is asymptotically unbiased with minimum variance of estimators and references therein [2,3]. Let $X_1, X_2, \cdots, X_n$ be independent and identically distributed random variables, i.e., $X_i \sim f(x;\boldsymbol{\theta}), i = 1,2,\dots,n$ shows that $X_1, X_2, \cdots, X_n$ have identical distributions. n represents the number of sample size as a sampling version of a p.d. function f as a population. In this case, the maximum likelihood estimators (MLE) of the parameters $\boldsymbol{\theta} = (\theta_1, \theta_2, \dots, \theta_p)$

$$L(\boldsymbol{\theta};x) = \prod_{i=1}^{n} f(x_i;\boldsymbol{\theta}) \tag{1}$$

is obtained by optimizing the likelihood function according to parameters $\boldsymbol{\theta} = (\theta_1, \theta_2, \dots, \theta_p)$. $x = (x_1, x_2, \dots, x_n)$ is a vector of observations and the likelihood function is a function of the parameters $\theta_1, \theta_2, \dots, \theta_p$. When the log function of both sides of the given expression in equation (1) is taken to get a tractable expression, the following expression is obtained as follow:

$$\log\big(L(\boldsymbol{\theta}; x)\big) = \sum_{i=1}^{n} \log\big(f\ (x_i; \boldsymbol{\theta})\big). \tag{2}$$

2.2. Maximum $\log_q$ likelihood estimation method

In the case of contamination, the robust and efficient estimations of the parameters of the f_0 distribution are performed by using the maximum likelihood $\log_q$ estimation (MLqE) method, which is a generalization of the likelihood estimation method and is also included in the M-functions [2,3], and

$$\log_q(L(\boldsymbol{\theta}; x))\ = \sum_{i=1}^{n} \log_q(f\ (x_i; \boldsymbol{\theta})) \tag{3}$$

is defined. $\log_q(f) = \frac{f^{1-q}-1}{1-q}$, $0 < q < 1$. The $\log_q$ function is called the q-deformed logarithm function. q is a tuning constant used to adjust robustness and efficiency [5,11].

2.3. Least informative distributions based on $\log_q$

Let the random variables $X_1, X_2, \cdots, X_n$ be independent and non-identically distributed. In this case, there is a contaminated distribution and

$$f_\varepsilon(x_i; \boldsymbol{\theta}) = (1-\varepsilon) f_0(x_i; \boldsymbol{\theta}) + \varepsilon f_1(x_i; \boldsymbol{\theta}) \tag{4}$$

is expressed as f_ε which indicates the contaminated distribution and is called as the least informative distribution (LID). The constant ε is the contamination rate. f_0 is the underlying distribution and the estimation values of the parameters of f_0 are tried to be obtained under f_1 which is the contamination into underlying distribution f_0.

The deformed entropies and deformed logarithms derived from these entropies have found many applications in physics and many corresponding fields [22-32]. Let us rewrite the definition of LID given by

$$f_\varepsilon = (1-\varepsilon) f_0 + \varepsilon f_1. \tag{5}$$

LIDs based on the maximum q-log-likelihood was proposed to find the optimal parameters $\boldsymbol{\theta}$ in the function f_ε by [11]. The variational calculus is used to get a case in which the objective function ρ sets out a minimal change with respect to the parameter ε when there exists a contamination into the underlying distribution f_0 by a small amount of outlier distribution f_1, i.e., we set ε in f_ε as a small value close to zero. In order to remove the role of f_1, the function $\rho(f_\varepsilon)$ is derived with respect to ε and set ε to zero. Thus, we can find the estimators of parameters μ and σ by using the following equation

$$\psi_{\log_q}(f_0(x; \mu, \sigma), f_1(x; \mu, \sigma)) = \sum_{i=1}^{n} f_0\ (x_i; \mu, \sigma)^{-q} [f_1(x_i; \mu, \sigma) - f_0(x_i; \mu, \sigma)]. \tag{6}$$

$\psi_{\log_q}(f_0(x; \mu, \sigma), f_1(x; \mu, \sigma))$ is called as a new objective function to fit data sets. The LIDs in MLqE are used for the estimations of parameters. The distribution f_1 in LIDs can have a role in fitting the data set as a flexible way to drive the efficiency in the estimation [3,11,12].

2.4. M-estimation method

The main idea of M-estimation method is based on the minimizing an objective function ρ with respect to parameters which will be estimated. The M-estimation method is introduced by the following equation:

$$(\hat{\mu}, \hat{\sigma}) \coloneqq \underset{\mu,\sigma}{\arg\min} \sum_{i=1}^{n} \rho(x; \mu, \sigma)) \tag{7}$$

$x = (x_1, x_2, \ldots, x_n)$ is a vector of observations. μ and σ are location and scale parameters respectively. After minimizing the mathematical expression in equation (7), the M-estimators of parameters μ and σ are obtained. The analytical tractability of the function ρ is necessary if we get the M-estimators which will be functions of random variables such as arithmetic mean which is well-known location estimator from MLE of location parameter μ in normal distribution [3].

As it is well-known, these two parameters can be added to any arbitrary function. In our case, we consider to add these parameters into objective function ρ. The following subsection is divided for introducing how we give the mathematical expression for the objective functions which will be used to fit the data.

2.5. Objective functions as M-functions and their M-estimations

The objective functions are very popular in robustness literature to fit the data sets. They were proposed by Huber and his coworkers. The objective function ρ notated by Huber and its derived form with respected to parameters is called as the function ψ. ψ is based on the estimating equations originally proposed by Godambe [9]. Throughout this paper, we consider to use the function ψ for representing LIDs in MLqE method. Thus, we have three objective functions in this paper. These are notated by $\rho_{\log}(f_0)$, $\rho_{\log_q}(f_0)$ and $\psi_{\log_q}(f_0, f_1)$.

Let us introduce their analytical expression given below:

$$\rho_{\log}(f_0) = \sum_{i=1}^{n} \log(f_0(x; \mu, \sigma)) \tag{8}$$

is from MLE taken by log function.

$$\rho_{\log_q}(f_0) = \sum_{i=1}^{n} \log_q(f_0(x; \mu, \sigma)) \tag{9}$$

is from MLqE taken by $\log_q$ function.

The following objective function is derived by using LIDs and MLqE method, as introduced by subsection 2.3 [11].

$$\psi_{\log_q}(f_0, f_1) = \sum_{i=1}^{n} f_0(x; \mu, \sigma)^{-q} [f_1(x; \mu, \sigma) - f_0(x; \mu, \sigma)], \tag{10}$$

where f_0 and f_1 are chosen from exponential power (EP) distribution. EP is defined by

$$f_{\mathrm{EP}}(x;\ \mu, \sigma, \alpha) = \frac{\alpha}{2\sigma\Gamma\left(\frac{1}{\alpha}\right)} \exp\{-\left(\frac{|x-\mu|}{\sigma}\right)^{\alpha}\}, \tag{11}$$

where α is shape parameter to arrange the peakedness of function and references therein [15,16].

The Gt distribution is given by

$$f_{\mathrm{Gt}}(x;\ \mu, \sigma, \alpha, \nu) = \frac{\alpha}{2\mathrm{B}\left(\frac{1}{\alpha}, \nu\right)\nu^{1/\alpha}\sigma} \left(1 + \left(\frac{|x-\mu|}{\nu^{\frac{1}{\alpha}}\sigma}\right)^{\alpha}\right)^{-(\nu+1/\alpha)}, \tag{12}$$

where α and ν are parameters for the shape of peakedness and the tail behaviour of function respectively. If the parameter ν goes to small values, then Gt distribution becomes heavy-tailed distribution. If we use a heavy-tailed

distribution to fit data set, then MLEs of the parameters μ and σ will be robust. The estimation of these parameters are not performed due to fact that we need to get the robust estimations of the parameters μ and σ [17] and references therein.

3. Information Criterions for Objective Functions

Information criterion (IC) is a tool to test the fitting performance of functions. Different tools are proposed by [18,19]. After proposing objective functions, we will have another problem to test the fitting performance of $\rho_{\log}$ from MLE, $\rho_{\log_q}$ from MqLE, ψ from Huber M-Estimation and $\psi_{\log_q}(f_0, f_1)$ from LID. For this aim, robust information criterion (RIC) formulae are used to determine the value of tuning parameter q. We can consider the equations (11) and (12) including the function log from objective function in equation (2). Since we use equation (2), the lack of fit part of IC with the penalty term c_k is given by

$$IC(f_0, c_k) = -2\rho_{\log}(f_0) + c_k. \tag{13}$$

IC in equation (13) have two parts that are the lack of fit and the penalty term. The difference between AIC and BIC is due to the penalty term c_k. The correct evaluation of AIC depends on the penalty term $c_k = 2k$, which is a deficiency of AIC [18]. As an alternative to AIC, BIC was proposed when $c_k = \log(\mathrm{n})k$. We propose robust version of ICs by replacing the objective function $\rho_{\log}$ with another objective function $\psi_{\log_q}(f_0, f_1)$. Thus, we have robust versions of ICs which can be reconsidered as the following form for the objective function $\psi_{\log_q}(f_0, f_1)$ from LID

$$RIC_q(f_0, f_1, c_k) = -2\,\psi_{\log_q}(f_0, f_1) + c_k, \tag{14}$$

We make a comparison among LID in MLqE, MLqE, Huber M-estimation and MLE of location and scale parameters of Gt distribution. Note that the value of q as a tuning constant must be taken to be fixed in order to get robust estimators. For example, for a given value of q, the fitting performances of $\psi_{\log_q}(f_0, f_1)$ and $\rho_{\log_q}(f_0)$ are tested until the smallest values of IC is obtained. For the Huber M-estimation and MLE method, the lack of fit part $-2\log L$ or $-2\log f$ for one sample case, i.e., $\mathrm{n} = 1$ are used, because they are based on the known logarithm function, i.e., log [11,22-32].

Since the LID has shape parameter α of EP distribution, it is logical to expect that the estimates are better than Huber's ρ function. Note that Huber's M-function is based on $\alpha = 2$ for $|y| \le k$ and $\alpha = 1$ for $|y| > k$. In other words, Huber M-estimation is normal distribution in middle, i.e. $|y| \le k$ and Laplace distribution in tail, i.e. $|y| > k$. Since Huber's M-function has the fixed values of shape parameters, there is no flexibility of Huber's M-function. For the determining of values of shape parameter α in EP distribution and tail parameter ν in Gt distribution, IC is used for the objective function $\rho_{\log}$, i.e., $\rho_{\log}(f_{EP})$ and $\rho_{\log}(f_{Gt})$ respectively. Choosing the best values of these parameters α and ν is processed while we are trying their different values of α and ν until the smallest values of IC are obtained. These parameters are also considered as tuning parameters for the sake of conducting the robust estimation procedure. For this reason, they will not be estimated [3,17].

4. Computation and Real Data Application

Optimizing $\psi_{\log_q}(f_0, f_1)$ in equation (10) according to parameters in p.d. functions f_0 and f_1 produces M-estimators $\hat{\mu}$ and $\hat{\sigma}$ from LID

$$(\hat{\mu}_\psi, \hat{\sigma}_\psi) := \underset{\mu \text{ and } \sigma}{\arg\max}\ \psi_{\log_q}(f_0, f_1) \tag{15}$$

If only f_0 is chosen for $\rho_{\log_q}$, then M-estimators $\hat{\mu}$ and $\hat{\sigma}$ will be obtained from a p.d. function f. Since $\psi_{\log_q}(f_0, f_1)$ and $\rho_{\log_q}$ are nonlinear functions according to the parameters in the p.d. function f, an optimization method as a maximization or minimization is essential to get the estimates of these parameters [2,3,11].

A data set is NCI60 cancer cell line panel. A protein data coded as BR:T-47D from Lysate Array at a website https://discover.nci.nih.gov/cellminer/ was analysed. The parameters μ and σ are estimated by using

objective functions to see tendency (location parameter μ) and spread (scale parameter σ) of protein in cancer cell. The maximum and minimum values which are added as two outliers are 12.5160 at positive and -12.5160 at negative sides of the real line, respectively. Thus, the symmetry of data has been kept. The search region in HGA at a module in MATLAB 2013a for the parameters μ and σ are taken as $[-50, 50]$ and $[0, 50]$, respectively. After running GA module in MATLAB 2013a, the estimates of parameters μ and σ are obtained as given in Table 1.

Table 1 has the M-functions from LID in MLqE, i.e., $\psi_{\log_{q=0.008}}(f_0 = EP(\alpha_0 = 2.15), f_1 = EP(\alpha_1 = 1.4))$ from EP distributions with fixed values of shape parameters $\alpha_0 = 2.15$ and $\alpha_0 = 1.4$, the estimates from MLqE for the parameters μ and σ in EP distribution with fixed value of shape parameter $\alpha = 2.51$ and Huber M-function with tuning parameter $k = 1.02$. When the estimates of two parameters are compared, it is observed that the estimate of $\hat{\mu}$ from LID in MLqE as a bold does not change if two outliers are added. The estimate of $\hat{\sigma}$ has a small changing from LID in MLqE. However, Huber M-estimation and MLEs of parameters μ and σ in Gt distribution cannot have a resistance to outliers and the values of estimates of two parameters have changed. As a result, LID in MLqE has robust estimates when it is compared with other objective functions in Table 1.

Table 1. Estimates of parameters μ and σ by using different objective functions without and with two outliers for protein data in cancer cell

M-functions: Objective functions based on $\log_q$	$\hat{\mu}$	$\hat{\sigma}$	$RAIC_q$	$RBIC_q$
$\psi_{\log_{q=0.008}}(f_0 = EP(\alpha_0 = 2.15), f_1 = EP(\alpha_1 = 1.4))$	**1.5752**	1.5585	13.8654	20.0406
Two Outliers	**1.5752**	1.5578	13.8650	20.0647
$\rho_{\log_{q=0.5}}(f_0 = EP(\alpha = 2.51))$	1.3616	**1.3237**	398.7907	404.9659
Two Outliers	1.3617	**1.3237**	406.7909	412.9906
M-functions: Objective functions based on log	$\hat{\mu}$	$\hat{\sigma}$	AIC	BIC
$\psi(f_0 = EP(\alpha = 2), f_1 = EP(\alpha = 1), k = 1.02)$	1.3532	1.3851	657.3162	663.4914
Two Outliers	1.3552	1.4933	695.6350	701.8348
$\rho_{\log}(f_0 = Gt(\alpha = 2.36, \nu = 1.95))$	1.2039	2.0388	677.1910	683.3662
Two Outliers	1.2027	2.0947	706.8218	713.0215

Table 1 also shows the information criteria such as Akaike and Bayesian. $RAIC_q$ and $RBIC_q$ are abbrevations for the robust Akaike and robust Bayesian criteria in which the lack of fit part is based on q in $\log_q$[11]. They are based on q in $\log_q$. The values of $RAIC_q$ and $RBIC_q$ in two cases which are without outliers and two included outliers can be very near to each other when the objective function is $\psi_{\log_{q=0.008}}(f_0 = EP(\alpha_0 = 2.15), f_1 = EP(\alpha_1 = 1.4))$. However, when the objective function is $\rho_{\log_{q=0.5}}(f_0 = EP(\alpha = 2.51))$, the values of $RAIC_q$ and $RBIC_q$ has been changed if there exist two outliers. As a result, the LID in MLqE can have robust information criteria as well due to the fact that the estimates obtained by objective functions based on $\log_q$ could not change more when we compare the values of AIC and BIC in Table 1.

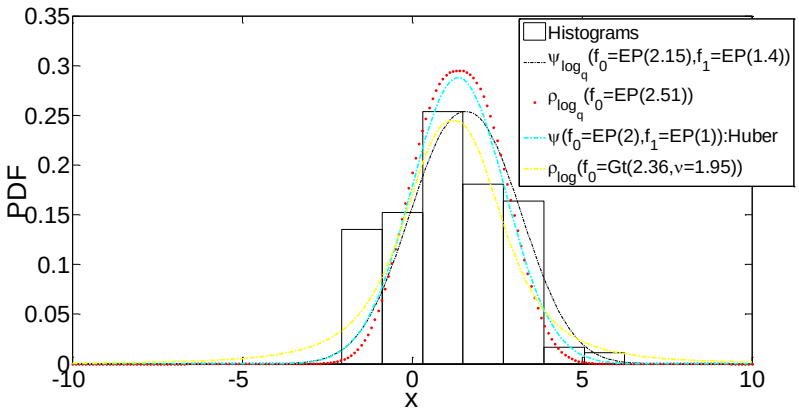

Figure 1. Robust M-estimators and MLE of parameters in f_0 and LIDs if outliers do not exist.

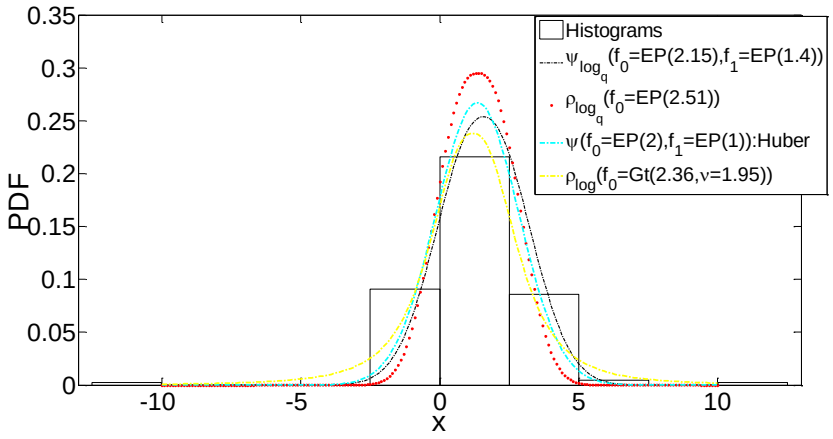

Figure 2. Robust M-estimators and MLE of parameters in f_0 and LIDs if there are two outliers.

Figures 1 and 2 are given for illustrative purpose. Four objective functions depicted by Figures 1 and 2 are used to estimate the parameters μ and σ. The p.d. functions abbreviated as PDF superimposed onto histograms are given by EP distributions with their corresponding fixed shape parameter α. Since the main aim was to plot the underlying distribution, we use the parameter α_0 from p.d. function f_0. There is also p.d. function of Gt distribution which has been used for plotting in Figures 1 and 2. After plotting the p.d. functions of EP with the estimates of M-estimators for the parameters μ and σ and the fixed values of shape and tail parameters of corresponding distribution, we can observe that $f_0 = EP(x; \hat{\mu} = 1.5752, \hat{\sigma} = 1.5585, \alpha_0 = 2.15)$ has a good competance on fitting the data set well when it is compared by the others that are $f_0 = EP(x; \hat{\mu} = 1.3616, \hat{\sigma} = 1.3237, \alpha_0 = 2.51)$, $f_0 = EP(x; \hat{\mu} = 1.3532, \hat{\sigma} = 1.3851, \alpha_0 = 2)$ and $f_0 = Gt(x; \hat{\mu} = 1.2039, \hat{\sigma} = 2.0388, \alpha_0 = 2.36, \nu = 1.95)$.

5. Conclusion

LIDs are obtained by using convex combinations of two p.d. functions for the estimations of location and scale parameters. Thus, the robust estimations of them have been performed by using the M-functions originally based on the M-estimation method. LIDs in MLqE, MLqE, M-estimation of Huber for the robust estimations of the parameters μ and σ and also MLEs the parameters μ and σ of Gt distribution have been compared if there exist two outliers into data set. So the resistance of these M-functions while conducting the robustness procedure has been observed. The role of MLqE method for LIDs have been examined when the parameters μ and σ are estimated simultaneously. The results showed the LID in MLqE can have robust to outliers not only for the estimates of two parameters but also information criteria. However, $\rho_{\log_q}$ with only one p.d. function f, Huber M-estimation and MLEs of the parameters μ and σ of Gt distribution with fixed values shape parameter α and the tail parameter ν determined by using the information criteria gave the estimates that cannot be resistance to outliers even if they are the M-functions used to get robust M-estimates of parameters. Since LIDs have two distributions f_0 and f_1 at the same time, the efficiency was observed for case in which two outliers are added into a real data set. The robustness properties of the objective function $\psi_{\log_q}(f_0, f_1)$ for all parameters in a p.d. function f will be a study in the future.

References

[1] Ni XS, Huo X. Another look at Huber's estimator: A new minimax estimator in regression with stochastically bounded noise. Journal of statistical planning and inference. 2009; 139(2):503-515.

[2] Huber PJ. Robust estimation of a location parameter. In Breakthroughs in statistics. Springer. New York, NY. 1992: 492-518.

[3] Huber PJ, Ronchetti EM. Robust statistics. John Wiley & Sons. New York. 1981.

[4] Shevlyakov G, Morgenthaler S, Shurygin A. Redescending M-estimators. Journal of Statistical Planning and Inference. 2008; 138(10): 2906-2917.
[5] Ferrari D, Yang Y. Maximum Lq-likelihood estimation. The Annals of Statistics. 2010; 38(2): 753-783.
[6] Giuzio M, Ferrari D, Paterlini S. Sparse and robust normal and t-portfolios by penalized Lq-likelihood minimization. European Journal of Operational Research. 2016; 250(1): 251-261.
[7] Andrews DF, Hampel FR. Robust estimates of location: Survey and advances. Princeton University Press. 2015
[8] Hampel FR, Ronchetti EM, Rousseeuw PJ, Stahel WA. Robust statistics: the approach based on influence functions. John Wiley & Sons. 2011. Vol. 196.
[9] Godambe VP. An optimum property of regular maximum likelihood estimation. The Annals of Mathematical Statistics,. 1960; 31(4):1208-1211.
[10] Malik SC, Arora S. Mathematical analysis. New Age International. 1992.
[11] Çankaya MN, Korbel J. Least informative distributions in maximum q-log-likelihood estimation. Physica A: Statistical Mechanics and its Applications. 2018; 509: 140-150.
[12] Gelfand I, Fomin S. Calculus of Variations. Prentice-Hall Inc. Englewood Cliffs. NJ.1963.
[13] Örkcü HH, Özsoy VS, Aksoy E, Dogan MI. Estimating the parameters of 3-p Weibull distribution using particle swarm optimization: A comprehensive experimental comparison. Applied Mathematics and Computation. 2015; 268: 201-226.
[14] Yalçınkaya A, Şenoğlu B, Yolcu U. Maximum likelihood estimation for the parameters of skew normal distribution using genetic algorithm. Swarm and Evolutionary Computation. 2018; 38:127-138.
[15] Çankaya MN, Bulut YM, Doğru FZ, Arslan O. A bimodal extension of the generalized gamma distribution. Revista Colombiana de Estadistica. 2015; 38(2): 353-370.
[16] Çankaya MN. Asymmetric bimodal exponential power distribution on the real line. Entropy. 2018; 20(1): 1-23.
[17] Arslan O, Genç Aİ. The skew generalized t distribution as the scale mixture of a skew exponential power distribution and its applications in robust estimation. Statistics. 2009; 43(5): 481-498.
[18] Bozdogan H. Model selection and Akaike's information criterion (AIC): The general theory and its analytical extensions. Psychometrika. 1987; 52(3):345-370.
[19] Ronchetti E. Robustness aspects of model choice. Statistica Sinica. 1997: 327-338.
[20] Çankaya MN, Yalçınkaya A, Altındağ Ö, Arslan O. On the robustness of an epsilon skew extension for Burr III distribution on the real line. Computational Statistics. 2019; 34(3): 1247-1273.
[21] Çankaya MN, Arslan O. On the robustness properties for maximum likelihood estimators of parameters in exponential power and generalized T distributions. Communications in Statistics-Theory and Methods. 2020; 49(3): 607-630.
[22] Tsallis C. Possible generalization of Boltzmann-Gibbs statistics. Journal of statistical physics. 1988; 52(1-2): 479-487.
[23] Machado JT. Fractional order generalized information. Entropy. 2014; 16(4): 2350-2361.
[24] Suyari H. Mathematical structures derived from the q-multinomial coefficient in Tsallis statistics. Physica A: Statistical Mechanics and its Applications. 2006; 368(1): 63-82.
[25] Hadjiagapiou IA. The random field Ising model with an asymmetric and anisotropic bimodal probability distribution. Physica A: Statistical Mechanics and its Applications. 2011; 390(20): 3204-3215.
[26] Hadjiagapiou IA. (2012). The random field Ising model with an asymmetric and anisotropic trimodal probability distribution. Physica A: Statistical Mechanics and its Applications, 391(13), 3541-3555.
[27] Çankaya MN, Korbel J. On statistical properties of Jizba–Arimitsu hybrid entropy. Physica A: Statistical Mechanics and its Applications. 2017; 475: 1-10.
[28] Korbel J. Rescaling the nonadditivity parameter in Tsallis thermostatistics. Physics Letters A. 2017; 381(32): 2588-2592.
[29] Jizba P, Korbel J, Zatloukal V. Tsallis thermostatics as a statistical physics of random chains. Physical Review E. 2017; 95(2): 022103.
[30] Elze HT. Introduction: Quantum Theory and Beneath?. In Decoherence and Entropy in Complex Systems. Springer. Berlin, Heidelberg. 2004: 119-124.
[31] Jizba P, Korbel J. On q-non-extensive statistics with non-Tsallisian entropy. Physica A: Statistical Mechanics and its Applications. 2016; 444: 808-827.
[32] Csaki, F. Second international symposium on information theory. Académiai Kiadó, Budapest, 1981.

Turkish Journal of Science & Technology
15(2), 79-84, 2020

The Effect of Photoperiod on Growth, and Protein, Lipid and Chlorophyll Content in *Scenedesmus Acutus*

Nur AGIRMAN KAYMAZ, A. Kadri CETIN*
Department of Biology, Faculty of Science, Firat University, Elazig, Turkey
dna_nur@hotmail.com, akadricetin@gmail.com

(Geliş/Received: 17/03/2020; Kabul/Accepted: 08/08/2020)

Abstract: The effect of photoperiod on the growth, protein, lipid and pigment content in *Scenedesmus acutus* was examined on cultures exposed to 23 ± 1 °C for ten days at the light intensity of 55 µmol photon $m^{-2}s^{-1}$. Results showed that photoperiods had an effect on cell number, and protein and chlorophyll content. The growth, protein, lipid and chlorophyll levels in *Scenedesmus acutus* cultures reached maximum in different days and photoperiods. The number of cells of the continuously illuminated cultures was highest on day seven after inoculation. The total protein and total lipid content were highest on day eight under the light/dark photoperiod of 20/4 h while total chlorophyll content was highest on day ten under the light/dark photoperiod of 24:0 h. The cultures continuously illuminated for cell growth had the highest specific growth rate (µ=0.2304). Protein content had a specific growth rate of µ=0.0725 under the light/dark photoperiod of 20/4 h while total chlorophyll content had a specific growth rate of µ=0.0890 under the light/dark photoperiod of 12:12-h.

Key words: Green algae, *Scenedesmus acutus*, photoperiod, growth, lipid

Scenedesmus acutus'un Gelişim, Protein, Lipid ve Pigment Miktarı Üzerindeki Fotoperiyodun Etkisi

Öz: Fotoperiyodun *Scenedesmus acutus*'un gelişim, protein, lipid ve pigment miktarı üzerindeki etkileri, 55 µmolphoton m-2s-1 ışık yoğunluğunda 23±1 °C sıcaklığa maruz bırakılan kültürlerde on gün süresince incelendi. Sonuçlar hücre sayısı, protein ve klorofil miktarı üzerinde fotoperiyodun etkili olduğunu gösterdi. *Scenedesmus acutus* kültürlerinde gelişme, protein, lipid ve klorofil miktarlarının farklı gün ve fotoperiyotta maksimuma ulaştığı tespit edildi. Sürekli aydınlatılan kültürlerde hücre sayısı inokülasyonu takip eden yedinci günde maksimuma ulaşırken, toplam protein ve total lipid miktarının 20:4-h aydınlık/karanlık fotoperiyodunda sekizinci günde, toplam klorofil miktarının da 24:0-h aydınlık/karanlık fotoperiyodunda onuncu günde maksimum olduğu görüldü. Spesifik büyüme oranı hücre gelişimi için sürekli aydınlatılan kültürlerde µ=0.2304 ile maksimum olurken protein miktarındaki spesifik büyüme oranı 20:4-h aydınlık/karanlık fotoperiyodunda µ=0.0725 ve toplam klorofil miktarındaki spesifik büyüme oranı ise 12:12-h aydınlık/karanlık fotoperiyodunda µ=0.0890 olduğu tespit edildi.

Anahtar kelimeler: Yeşil alg, *Scenedesmus acutus*, fotoperiyot, büyüme, lipit

1. Introduction

The growing demand for alternative energy sources results in an increased interest in biofuel production. Biofuel production from microalgae is one of the most interesting research topics. Microalgal can be converted into various biofuels such as biomass, biomethane, bioethanol and bio-oil. Due to lipids, microalgae are the most useful sources of biodiesel. Microalgal biomass is superior to other biomass-based energy resources because it grows rapidly and has high concentrations of carbohydrate and lipid. Microalgae can accumulate carbohydrates and lipid as well as secondary metabolites and are therefore useful organisms for biotechnological research. Microalgae are biotechnologically important because their biomass contains valuable components including starch, protein, lipids and a wide variety of alkanes [1]. Microalgae are used in the production of a wide variety of compounds, such as dyes, antioxidants, gelling agents, amino acids, emulsifiers and omega 3. Microalgal proteins and pigments have great potential in medical applications as well.

Numerous factors such as nutrients, pH, temperature, light and salinity affect on microalgal growth. Light is the main factor controlling the biochemical and physiological processes of microalgae [2]. Intensity, wavelength and photoperiods are of paramount significance for photosynthesis. Light/dark photoperiods significantly affect algal growth and biomass. Light intensity and regime constantly change in natural environments [2]. Changes in light/dark photoperiods change the carbohydrate, protein and lipid concentrations of microalgae cells [3-6]. Krzeminska et al. investigated the effect of photoperiod on the growth rate and biomass productivity of *Botryococcus braunii*, *Scenedesmus obliquus*, *Neochloris conjuncta*, *Neochloris Terrestris* and *N. texenis* [1]. Wahidin et al. examined the effect of light intensity and photoperiod on the growth and lipid content in

*Corresponding author: kcetin@firat.edu.tr, ORCID Number of autors:[1]0000-0002-4974-4858, [2] 0000-0002-8687-2912

Nannochloropsis sp. and reported that algae species exhibited different growth models [7]. Numerous studies have investigated the effect of photoperiod on cell growth and lipid and protein content. Algae species differ in light requirements, reproduction patterns and life cycles. *S. acutus* is a cosmopolitan green microalgae composed of two, four or eight ellipsoid or oval cells arranged in one or two rows. *S. acutus* has been extensively studied concerning valuable chemicals and healthy nutrition. *S. acutus* is an important member of the aquatic food chain and is widely used in aquaculture as an alternative source of protein for food and feed purposes [8].

This study investigated the effect of photoperiod on the growth, and total protein, lipid and pigment content in *S. acutus*, which was grown under three photoperiod cycles for 10 days. Cell count was performed, and lipid, protein and pigment content was determined in the cultures every day.

2. Material and Methods

S. acutus samples were collected from Keban Dam Lake and isolated in the algal biotechnology laboratory of Fırat University and cultivated in Jaworski's medium, which contained 80 mg $NaNO_3$, 36 mg $Na_2HPO_4.12H_2O$, 20 mg $Ca(NO_3)_2.4H_2O$, 12.4 mg KH_2PO_4, 50 mg $MgSO_4$. $7H_2O$, 2.25 mg EDTAFeNa, 2.25 mg $EDTANa_2$, 2480 µg H_3BO_3, 15.9 mg $NaHCO_3$, 1390 µg $MnCl_2.4H_2O$, 1000 µg $(NH_4)_6Mo_7.4H_2O$, 40 µg biotin, 40 µg cyanocobalamin (B_{12}) and 40 µg thiamin (B_1). The medium was sterilized at 121 °C for 1 min at 1 atmosphere pressure. *S. acutus* samples were inoculated into 250 mL Erlenmeyer with 100 mL Jaworski's medium. The Erlenmeyers were incubated in an air conditioning unit for 10 d at 23 ± 1 °C and light intensity of 55 µmol photon $m^{-2}s^{-1}$. 10 mL of the cultures that reached a certain density was sampled and placed in the Erlenmeyers, which were then placed in the air conditioning unit for incubation at 23 ± 1 °C and light intensity of 55 µmol photon $m^{-2}s^{-1}$ under different photoperiods. The Erlenmeyers were shaken three times a day. Samples were collected from the Erlenmeyers exposed to different photoperiods. The samples were analyzed for ten days to determine the cell number, and total protein, lipid and total chlorophyll content in *S. acutus*.

Growth Measurement

S. acutus was counted under a microscope using a plankton counting chamber. Algal biomass concentration was measured at an optical density of 680 using visible density spectrophotometer. Spectrophotometer measurements were compared with microscopic counts. A standard curve was plotted with optical density to calculate the number of individuals. All calculations were performed in triplicate.

Total Protein Measurement

Total protein content was determined using Lowry method. 0.1-ml DOC solution was added onto a 1-ml sample, which was then kept at room temperature for 10 min. Afterwards, 0.1 mL TCA was added onto the sample, which was then centrifuged at 7500 rpm for 10 min. Following the removal of the supernatant, 1 mL Lowry solution was added onto the precipitate, which was then kept at room temperature for 20 min. Later on, 1 mL fooling reagent was added onto the sample, which was then kept for 30 min. Lastly, absorbance was measured at 750 nm and results were evaluated based on the standard curve [9].

Total Lipid Measurement

Total lipid content was determined using the Bligh and Dyer method [10]. A mixture of 40 mL methanol and 80 mL chloroform was added onto a 0.2-g sample, and then, 20 mL $CaCl_2$ (4%) was added onto it. The mixture was filtered through filter paper and allowed to stand overnight in the dark. The following day, methanol and water were separated using a separatory funnel, and chloroform was evaporated in a water bath at 60 °C. Chloroform was completely evaporated by allowing the remaining part to stand for 1 h at 90 °C. Afterwards, the sample was weighed.

Chlorophyll analysis

Chlorophyll content was determined using the method of Strickland and Parsons [11]. A 5-mL culture was filtered through GF/C filter papers to determine pigment concentrations. Each filter paper was placed in 90% acetone at +4 °C, kept in the dark for 24 h, centrifuged at 3500 rpm for 5 min and analyzed for chlorophyll content by measuring the absorbances at 630, 645, 665 and 750 nm using the spectrophotometer.

2. Results

This study investigated the growth, and protein, lipid and pigment content in *S. acutus* at the light intensity of 55 µmol photon $m^{-2}s^{-1}$ and under four photoperiods (24:0, 20:4, 18:6 and 12:12-h light:dark). Figure 1 shows the effect of photoperiod on the growth in *S. acutus*. *S. acutus* had maximum growth at the light intensity of 55 µmol photon $m^{-2}s^{-1}$ under the light/dark photoperiod of 24:0 h. The number of cells increased from 850730 cell/ml (onset of inoculation) to 6.7 $x10^6$ cell/ml (day 7). Maximum growth under the light/dark photoperiods of 12:12 h and 20:4 h was, respectively, 6.4 $x10^6$ cell/ml and 5.3 $x10^6$ cell/ml on day eight (Figure 1). The highest (µ=0.2304) and lowest (µ=0.1939) specific growth rates in *S. acutus* were observed under the light/dark photoperiods of 24:0 h and 18:6 h, respectively.

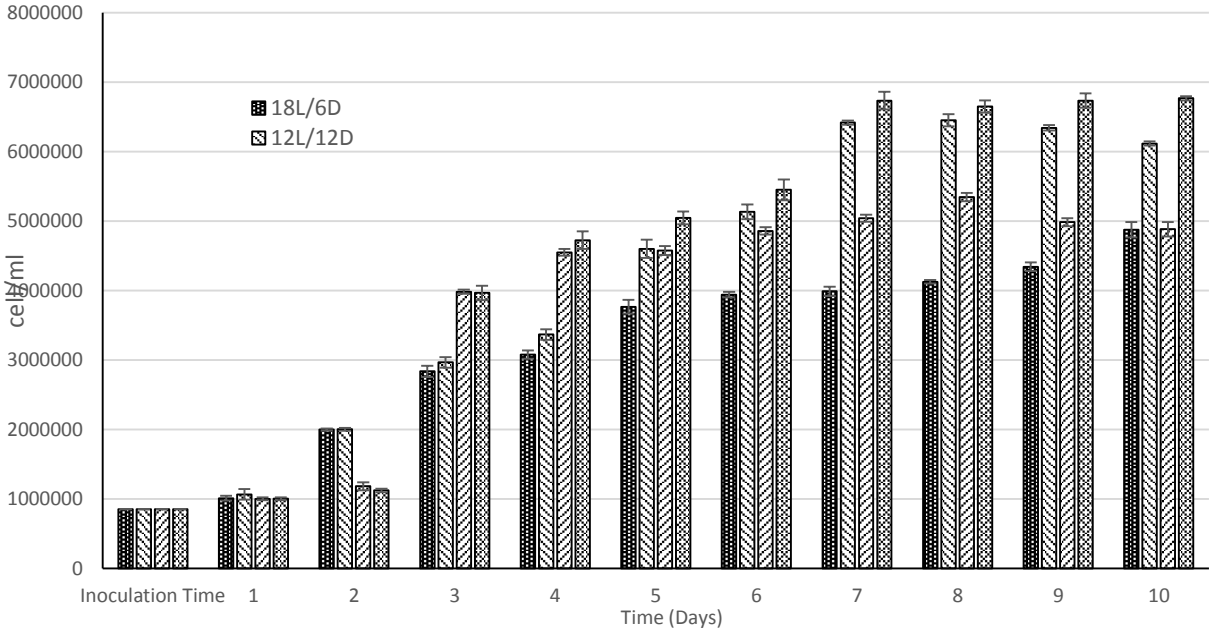

Figure 1. Cell number of *S. acutus* cultured at different photoperiods

Figure 2 shows the effect of photoperiod on the protein content of *S. acutus*. The protein content increased from 39.473µg/ml (onset of inoculation) to 65.610µg/ml (day eight under the light/dark photoperiod of 20:4 h). The highest protein content (65.486µg/ml) under the light/dark photoperiods of 24:0 h and 18:6 h was, respectively, 65.486µg/ml and 65.030 µg/ml on day ten. The highest protein content (64.356 µg/ml) under the light/dark photoperiod of 12:12 h was observed on day eight. The rate of increase in protein content in *S. acutus* cultures exposed to different photoperiod cycles also differed. The rate of increase in protein content under the light/dark photoperiods of 20:4 h and 12:12 h was, respectively, µ=0.0725 and µ=0.0698. The protein content under the light/dark photoperiod of 24:0 h was highest on day ten, and the rate of increase was µ=0.0562. The protein content under the light/dark photoperiod of 18:6 h was highest on day ten, and the rate of increase was µ=0.554. The rate of increase in protein content was highest under the light/dark photoperiod of 20:4.

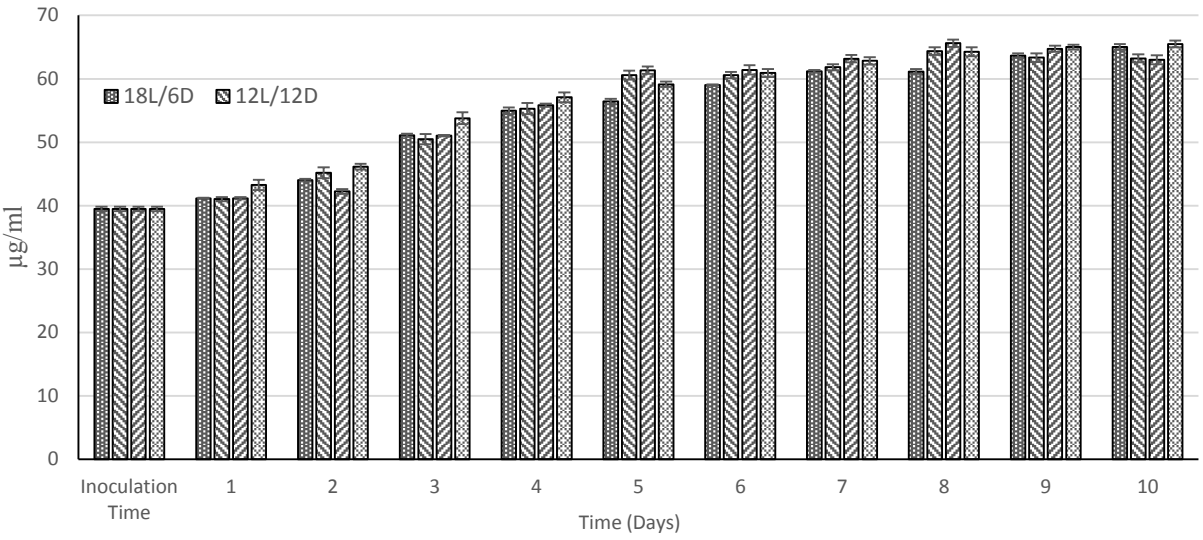

Figure 2. Protein contents of *S. acutus* cultured at different photoperiods

Figure 3 shows the effect of photoperiod on the lipid content of *S. acutus*. The total lipid content continuously increased from 4% (onset of inoculation) to 10.6% (day nine under the light/dark photoperiod of 18:6 h). The highest lipid content under the light/dark photoperiods of 12:12 h, 20:4 h and 24:0 h was, respectively, 10.77%, 11.5% and 11.71% on day eight. The highest increase in lipid content was observed in 24:0 h cultures on day eight.

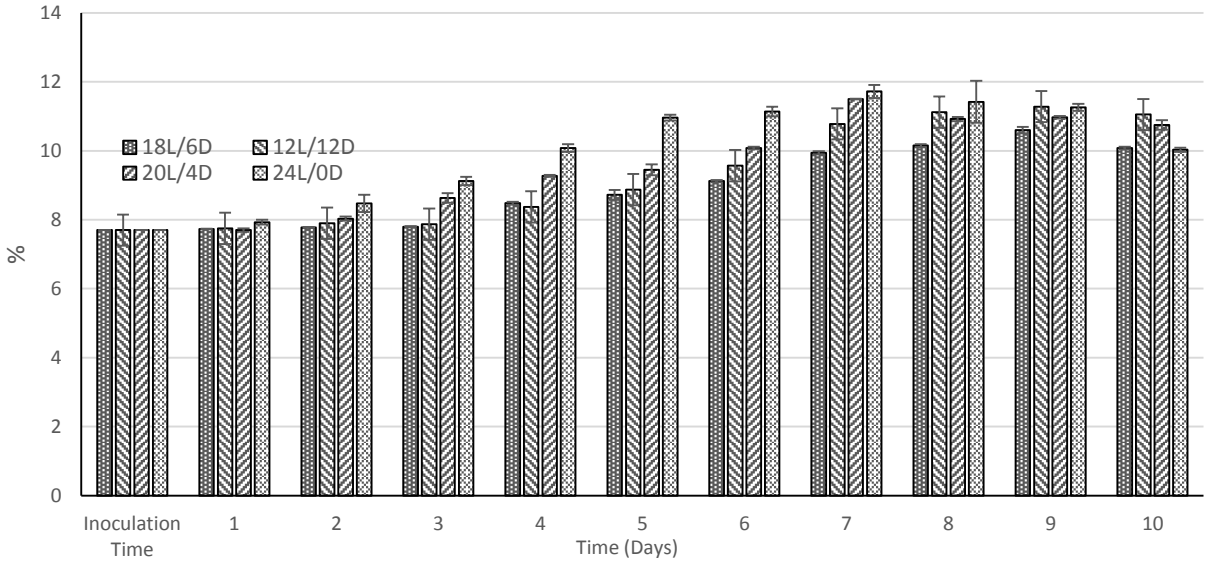

Figure 3. Lipid contents of *S. acutus* cultured at different photoperiods

This study investigated the effect of photoperiod on the total chlorophyll content of *S. acutus* for ten days. Figure 4 shows the results. The highest total chlorophyll content under the light/dark photoperiods of 24:0 h and 20:4 h was, respectively, 6.123 mg/ml and 4.970 mg/ml on day ten. The highest total chlorophyll content under the light/dark photoperiods of 18:6 h and 12:12 h was, respectively, 4.80 mg/ml and 5.550 mg/ml on day eight. *S. acutus* cultures had the highest (µ=0.0890) and lowest (µ=0.0531) specific growth rate under the light/dark photoperiods of 12:12 h and 18:6 h, respectively.

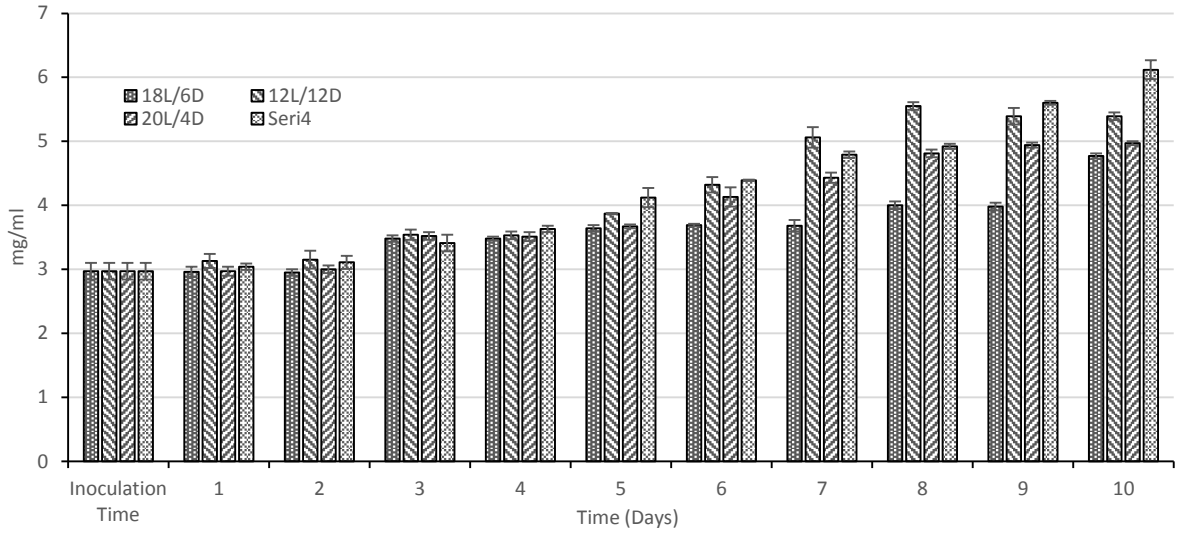

Figure 4. Chlorophyll contents of *S. acutus* cultured at different photoperiods

3. Discussion

Research shows that changes in light regimes reveal differences in the pigment and biochemical composition of microalgae [5, 12, 13, 14]. The growth rate in many microalgae occurs under high light conditions [15-17]. Photosynthetic responses to photoperiod vary across microalgae species [8, 15]. However, photoperiod affects not only the growth rate but also the composition and quantity of high-value microalgal products in algae species [2, 5, 7]. The total protein, pigment and fatty acid content in *C. vulgaris* [14], the growth and lipid production in *Porphyridium cruentum* ([18] and *B. braunii* [19] and the cell density, cell growth rate and total lipid content in *Nannochloropsis* sp [7] are affected by changes in photoperiod. Photoperiod culture studies in microalgae cultures illuminated by artificial light are cost-effective. Some studies are investigating the effect of photoperiod on microalgae biomass [2, 19, 20]. Our results show that photoperiod affect on cell growth, and protein and chlorophyll content in *S. acutus*. Khoeyi et al. reported that photoperiod is one of the most important factors affecting the biomass growth in *Chlorella vulgaris* [2]. Especially long light duration increase biomass and specific growth rate. In our study, the highest specific growth rate was observed under the light/dark photoperiod of 20:0 h, which has also been reported by previous studies. Seyfabadi et al. reported that long light duration increase in the protein content in *C. vulgaris* [2]. In our study, *S. acutus* cultures had the highest protein content and quite high specific growth rate (μ=0.0725) on day eight under the light/dark photoperiod of 20:4 h, followed by 12:12 h, 24:0 h and 18:6 h. This result indicates that light duration increases the protein content of microalgae. Numerous studies show that photoperiod at different developmental phases affect the total lipid content and lipid composition of microalgae [2, 7, 14, 21]. Raungsomboo (2012) reported that *Botryococcus braunii* had the highest lipid content under the light/dark photoperiod of 16: 8 h. In our study, the highest lipid content was observed under the light/dark photoperiod of 24:0 h on day eight. Ruangsomboon, Seyfebadi et al., Singh and Singh, reported the effect of photoperiod on pigment content [19, 14, 22] . In our study, the total chlorophyll content regularly increased from the onset of inoculation. The highest rate of increase was observed under the light/dark photoperiod of 20:4 h. However, the highest specific growth rate was observed under the light/dark photoperiod of 12:12 h.

Our results showed that an increase in photoperiod increased the cell number, and thus, biomass of *Scenedesmus acutus*. We believe that increasing cell concentrations under light/dark photoperiods can reduce production costs. The necessity of a dark phase in culture studies is accounted for by that of light and dark phase in photosynthesis. Compounds produced in a light phase (ATP, NADPH) are used in the dark phase to synthesize the metabolic molecules necessary for growth. Our results showed that photoperiod had affect the growth and chlorophyll, protein and lipid content in *S. acutus*.

References

[1] Krzemińska I., Pawlik-Skowrońska B., Trzcinska M. and Tys J. (2014). Influence of photoperiods on the growth rate and biomass productivity of green microalgae. Bioprocess. Biosyst. Eng. 37: 735-741.

[2] Khoeyi ZA., Seyfabadi J. and Ramezanpour Z. (2012). Effect of light intensity and photoperiod on biomass and fatty acid composition of the microalgae, *Chlorella vulgaris*. Aquacult. Int. 20:41-49.

[3] Tzovenis I., Pauw ND. and Sorgeloos P. (1997). Effect of different light regimes on the docosahexaenoic acid (DHA) content of *Isochrysis* aff. *galbana* (clone T-ISO). Aquaculture International. 5: 489-507.

[4] Price LL., Yin K. and Harrison PJ. (1998). Influence of continuous light and L:D cycles on the growth and chemical composition of *Prymnesiophyceae* including coccolithophores. J Exp. Biol. Ecol. 223: 223-234.

[5] Fabregas J., Maseda A., Dominquez A., Ferreira M. and Otero A. (2002). Changes in the cell composition of the marine microalga, *Nannochloropsis gaditana*, during a light:dark cycle. Biotechnoll. Let. 24: 1699-1703.

[6] Kendirlioglu G., Agirman N. and Cetin A.K. (2015). The Effects of Photoperiod on The Growth and Pigment Content of *Chlorella vulgaris*. F.U.Turkish Journal of Science & Technology, 10 (2), 7-10.

[7] Wahidin S., Idris A. and Shaleh SRM. (2013). The influence of light intensity and photoperiod on the geowth and lipid content of microalgae *Nannochloropsis* sp. Bioresour. Technol. 129: 7-11.

[8] Richmond A. (2004). Biological principles of mass cultivation. In Richmond A (ed) Handbook of microalgal mass, culture: biotechnology and applied phycology. CRC Press, Blackwell Publishing Company, Oxford, pp 566.

[9] Lowry OH, Rosebrough NJ, Farr AL, Randall RJ. Protein measurement with the folin phenol regent. J. Biol. Chem. 1951; 193:265-75.

[10] Bligh EG, Dyer WJ. A rapid method for total lipid extraction and purification. Can. Biochem. Physiol. 1959; 37:911-917.

[11] Strickland J. and Pearson TR. (1972). A Pratical Handbook of Seawater Analysis, second ed. Fish Res. Can. Bull.

[12] Renaud SM., Parry DL., Thinh LV, Kuo C., Padovan A. and Sammy N. (1991). Effect of light intensity on the proximate biochemical and fatty acid composition of *Isochrysis* sp. and *Nannochloropsisi oculata* for use in tropical aquaculture. J. Appl. Phycol. 3: 43-53.

[13] Sanchez-Saavedra MP. and Voltolina D. (2002). Effect of photon fulence rates of hite and blue-green light on growth efficiency and pigment content of three diatom species in batch cultures. Cienc. Mar. 28: (3): 273-279.

[14] Seyfabadi J. Ramezanpour Z. and Khoeyi ZA. (2011). Protein, fatty acid, and pigment content of Chlorella vulgaris under different light regimes. J Appl. Phycol. 23: 721-726.

[15] Bouterfas R., Belkoura M. and Dauta A. (2006). The effcts of irradiance and photoperiod on the growth rate of three freshwater green lgae isolated from a eutrophic lake. Limnetica, 25 (3): 647-656.

[16] Watson D., Daume S., Prince J., Beazley L. and Knott B. (2004). The influence of light intensity on the density on the density of different diatoms as fed for juvenile greenlip abalone (*Haliotis laevigata*). Aquaculture, 235: 345-359.

[17] Meseck SL., Alix JH., Gary H. and Wikfors GH. (2005). Photoperiod and light intensity effects on growth and utilization of nutrients by the aquaculture feed microalga *Tetraselmis chui* (Ply429). Aquaculture, 246: 393-404.

[18] Oh SH., Han JG., Kim Y Ha JH., Kim SS., Jeong MH., Jeong HS., NY., Cho JS., Yoon WB., Lee SY., Kang DH. and Lee HY. (2009). Lipid production in *Porphyridium cruentum* grown under different culture conditions. Journal of Bioscience and Bioenginering, 108, 5, 429-434.

[19] Ruangsomboon S. (2012). Effect of light, nutrient, cultivation time and salinity on lipid production of newly isolated strain of the green microalga, *Botryococcus braunii* KMITL 2. Bioresource Technology, 109: 261-265.

[20] Mata TM., Melo AC., Simoes M. and Caetano NS. (2012). Parametric study of a brewery effluent treatment by microalgae *Scenedesmus obliquus*. Bioresour. Technol. 107: 151-158.

[21] Kotimchenko SV. and Yakovleva IM. (2005). Lipid composition of the red alga Tichocarpus crinitus exposed to different levels of photon irradiance. Phytochemistry, 66: 73-79.

[22] Singh SP. and Singh P. (2015). Effect of temperature and light on the growth of algae species: A review. Renewable and Sustinable Energy Reviews, 50: 431-444.

Turkish Journal of Science & Technology
15(2), 85-92, 2020

Voltage Controlled Boost Converter-Inverter System for Photovoltaic Applications

Zeynep Bala DURANAY[1*], Hanifi GULDEMIR[2]

Firat University, Technology Faculty, Department of Electrical Electronics Engineering, Elazig, Turkey
[1]zbduranay@firat.edu.tr, [2]hguldemir@firat.edu.tr

(Geliş/Received: 04/04/2020; Kabul/Accepted: 16/06/2020)

Abstract: Photovoltaic electric energy generation systems are attractive for the places far from the electric grid system and for small scale applications. Off-grid inverters are widely used in renewable energy applications. Most of the applications such as home appliances require constant voltage. Thus, the voltage of the inverter needs to be kept constant. In this paper, the analysis, modelling, control and simulation of a photovoltaic module fed boost converter-inverter system is studied. The PV fed boost converter provides dc link for the inverter. The cascade connection of boost converter and an inverter provides sinusoidal voltage to the ac loads. A conventional proportional+integral (PI) controller is used to obtain a constant dc link voltage even with input voltage variations. Matlab-Simulink programming environment is used for the modelling and simulations. The simulation results are presented.

Key words: Boost converter, dc link control, inverter, off-grid inverter, voltage regulation.

Fotovoltaik Uygulamalar için Gerilim Kontrollü Yükseltici Çevirici-Evirici Sistemi

Özet: Fotovoltaik enerji üretim sistemleri elektrik şebekesinden uzak yerlerdeki küçük çaplı uygulamalar için oldukça caziptir. Şebeke bağımsız olarak çalışan eviriciler yenilenebilir enerji uygulamalarında yaygın olarak kullanılmaktadır. Ev aletlerinde olduğu gibi birçok uygulama sabit gerilim gerektirmektedir. Bu nedenle bağlı olduğu evirici geriliminin sabit tutulması gerekir. Bu çalışmada bir fotovoltaik modül beslemeli yükseltici çevirici-evirici sistemin analizi, modellenmesi, kontrolü ve benzetimi yapılmıştır. Fotovoltaik modül beslemeli yükseltici çevirici, evirici için gerekli dc gerilimi sağlamaktadır. Kaskad bağlı yükseltici çevirici ve evirici ise ac yükler için gerekli sinüsoidal gerilimi oluşturmaktadır. Giriş gerilimlerinin değişmesi durumunda da sabit bir dc link gerilimi elde etmek için geleneksel PI denetleyici kullanılmıştır. Modelleme ve benzetim için Matlab/Simulink programlama ortamı kullanılmış ve benzetim sonuçları sunulmuştur.

Anahtar kelimeler: Yükseltici çevirici, dc link kontrol, evirici, şebeke bağımsız evirici, gerilim kontrolü.

1. Introduction

New energy resources such as wind power, fuel cell and solar power have been started to be used in home appliances [1] as well as industrial [2] and agricultural [3] applications. The use of solar power, which is one of the most popular renewable energy resources, for generation of electricity [4] is becoming very attractive over the years because of sustainability. The energy obtained from solar photovoltaic (PV) power has vital importance especially for the places where the access of electricity is impossible or it is too difficult in every means to access it [5-6]. In this case off-grid or standalone PV energy generation systems are used [7-9].

PV panels generate DC power. Because the voltage produced by the PV panels is low in magnitude it is required to be increased either using more panels or dc-dc boost converter [10]. This dc voltage has to be inverted to the mains values both in voltage level and frequency. A step up transformer or a boost inverter can be used to bring the voltage level and frequency to mains level. Mostly, inverters are preferred to transformers due to reliability and efficiency.

As the voltage produced by panels change by the climatic conditions such as temperature, irradiation, shading and clouding, the constant voltage level has to be maintained to prevent failures of the connected devices due to voltage oscillations. Dc-dc converters can be used to keep constant dc link voltage for the inverter. This time a converter need to be used together with the inverter causing decrease in efficiency, increase in circuit size and complication in control system structure.

* Corresponding author: zbduranay@firat.edu.tr. ORCID Number of authors: [1] 0000-0003-2212-5544, [2] 0000-0003-0491-8348

In this paper, a classical PI controller is used to keep the dc bus voltage constant and not affected by the dc source voltage changes. To achieve high precision, a control system which compensates the dc link voltage variations using boost converter and an inverter to perform a power conversion with a constant output voltage is studied.

The system can be used in applications where an ac voltage is required to obtain from a low dc voltage source such as photovoltaic applications or electrical vehicles.

2. Single Phase Inverter

An inverter is a vital interface between renewable energy source and an ac load, providing an ac power required by ac loads. A few kVA rating low power applications use single-phase inverters which have two types of structures. One of the single phase inverter structure as shown in Figure 1, is the half bridge inverter which is used for low cost applications. Two capacitors are used for the dc link in this structure and the load is connected to the connection point of these capacitors. The output voltage value can be between half of the negative and positive dc bus voltage i.e. between the values of –E/2 and E/2. In this topology the capacitors are charged by the load current causing dc bus voltage fluctuation. To decrease the output voltage ripples produced by this voltage fluctuation and to increase the performance of the system, these dc bus capacitors need to have a large capacity.

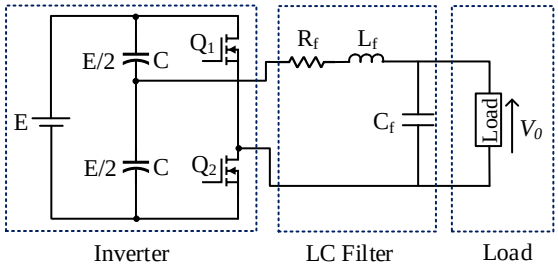

Figure 1. Half bridge single phase inverter.

The other type of the single phase inverter is the full bridge single phase inverter which has two legs to control the output voltage as shown in Figure 2. When compared with the half bridge inverter the dc bus capacitors have smaller capacity than those of the half bridge inverter capacitors as the connection point of these capacitors is not used for load. The output voltage can take the values between the negative and positive dc bus voltage values i.e. between –Vdc ~ +Vdc. These type of inverters are mostly used in high performance and high power applications.

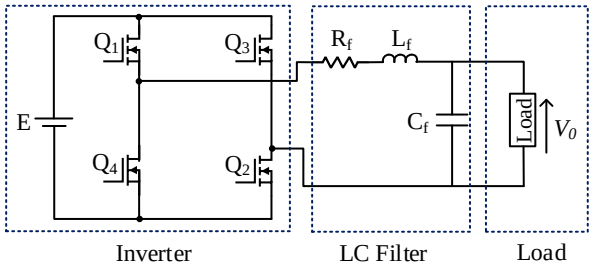

Figure 2. Full bridge single phase inverter.

If the half bridge inverter structure is planned to be used for a 220V utility application, then 800V dc bus voltage is needed. This voltage is reduced to 400V if full bridge single phase inverter is used.

Fast change of voltage (dv/dt) in the inverter results over voltages applied to load. This further creates additional problems such as increase in bearing currents, eddy current losses in the core and skin-effect losses in the windings if the load is an induction machine [11]. One of the solutions to reduce the dv/dt is to use a filter with passive elements at the inverter output [12, 13]. LC type filters are the most used filters [14]. The electrical circuit of the AC inverter shown in Figure. 2 includes an H-bridge inverter and an LC harmonic filter [15, 16].

An open loop PWM controller is used for the output voltage of the inverter. The LC filter is used for suppressing the higher-order current harmonics because of high frequency switching to reduce total harmonic distortion (THD) and also to reduce high dv/dt [17]. The design of the LC filter can be made with the equations presented in [18-20].

The single phase inverter applications require a power up to 5 kW and a dc voltage level of 400 V [21]. They are one of the main element of the off-grid residential PV applications.

3. Dc-Dc Boost Converter

If photovoltaic panels or battery groups are used to obtain a dc bus voltage for the inverter, then the dc output voltages of these PV panels or batteries need to be increased to required level. For this purpose, a dc-dc boost converter is used.

A dc-dc boost converter produces a higher output voltage from a low value dc input voltage by periodically making the switch in the circuit to be on and off.

The circuit diagram of a boost converter is given in Figure 3, where E represents the dc input voltage, S, L, C, D and R are the switch, inductor, filter capacitor, diode and the load respectively.

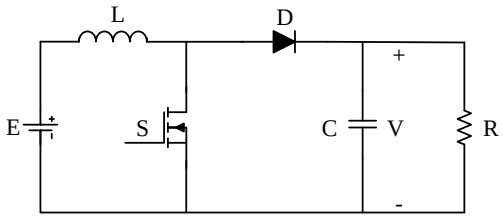

Figure 3. Dc-dc boost converter.

The analysis of the boost converter is made by examining the inductor current and voltage during a switching period. As shown in Figure 4-a and b, the dc-dc boost converter has two modes of operation [22] depending on switch states.

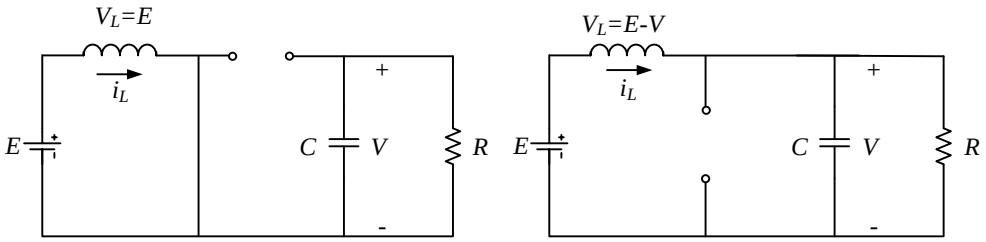

Figure 4. Equivalent circuits for switch closed (a) and for switch open (b).

If the switch S is closed, the diode D reverse biased and becomes off. The current in the inductor increases linearly. The capacitor feeds the load at this mode. In the second mode the switch is become off and the stored inductor current discharges through the diode and the load. Thus in this mode both inductor current and capacitor voltage feeds the load.

Waveforms of the steady state operation of the converter during one period of the switching is shown in Figure 4.

From Figure 4, the voltage across the inductor L during a switching period T is,

$$V_L(t) = \begin{cases} E & during \quad DT \\ E - V & during \quad (1-D)T \end{cases} \tag{1}$$

Due to the volt-second balance, the average voltage across the inductor in one switching period must be zero then,

$$E.DT + (E - V)(1 - D)T = 0 \quad (2)$$

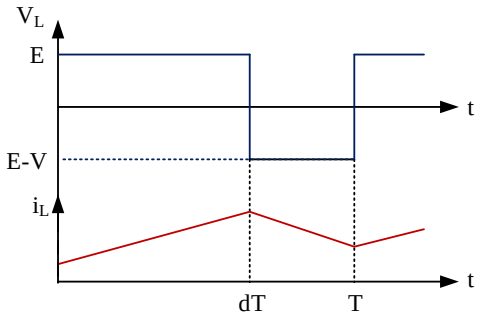

Figure 5. Boost converter waveforms for inductor voltage and current.

rewriting,

$$\frac{V}{E} = \frac{1}{1-D} \quad (3)$$

and the output voltage of the boost converter related to input voltage and duty cycle is

$$V = \frac{E}{1-D} \quad (4)$$

Equation 4 says that if switch is always open then D is zero, then the output voltage is equal to the input voltage. If duty ratio D is increased the denominator of Equation 4 will be smaller producing large output voltage. Thus, dc-dc boost converter produces an output voltage which is greater than or equal to the input voltage.

4. Model of Boost Cascade Connected Converter-Inverter

In this study, a cascade connected DC-DC power converter, an H-bridge inverter and a DC motor, as depicted in Figure 6, is considered.

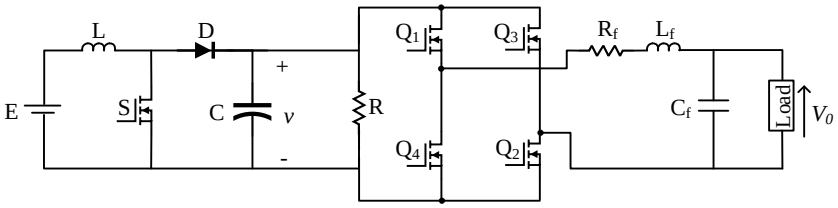

Figure 6. Single phase boost converter-inverter.

The DC-DC power converter is a boost type converter, consists of a DC power supply (E), a switching transistor (S) which regulates the converter output voltage (v), a diode (D), resistor (R), inductor (L) and capacitor (C). This converter is used to adjust the motor voltage which, in this case, is the dc link voltage of the inverter.

The inverter is an H-Bridge inverter i.e. two leg inverter with four switching transistors Q1-Q4. Transistors Q1 and Q2 are given with the same gate signal. The complement of this signal is applied to the other two transistors Q3 and Q4. That is, if Q1-Q2 both are on then Q3-Q4 both are off at the same time.

The load is an ac load.

The overall system, as listed in Table 1, have four modes of operation depending on the state of the switches S and Q1-Q4. Therefore, this system constitutes a variable structure system.

Table 1. Modes of operation.

Modes	S	Q1-Q2	Q3-Q4
1	ON	ON	OFF
2	ON	OFF	ON
3	OFF	ON	OFF
4	OFF	OFF	ON

5. Dc Bus Voltage Controller

The overall boost converter inverter system with control scheme is shown in Figure 7. The input voltage of the boost converter is provided by a photovoltaic array. The PV module generates a dc voltage output depending on the irradiation and temperature conditions. The dc link voltage of the inverter which is the output of the boost converter is measured and compared with the reference voltage. The error between the measured voltage and reference voltage is applied to a PI controller. In the PWM block, the output of the PI controller is compared with a triangular carrier wave to produce a PWM signal for the switch S of the boost converter. Depending on the error between measured and reference voltage a PWM signal is produced for the switch S to increase the output voltage of the boost converter if the error is positive and to decrease the output voltage if the error is negative. Thus regulating the output voltage of the boost converter which is also the dc bus voltage of the inverter. The parameters of the PI controller here is determined by trial and error method.

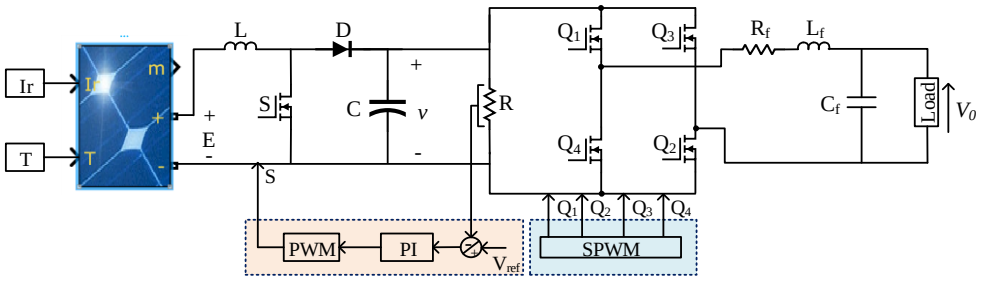

Figure 7. Block diagram of the converter-inverter system with control scheme.

6. Simulations

The Simulink program block of the boost converter-inverter system is shown in Figure 8. In this study Trina Solar TSM-250PA05.08 PV module is used. This PV module is 250 W, 31 V and 8.55 A at 1000 W/m^2 at maximum power point. The PV array contains 8 series connected modules produceing 240 V, 2000 W under 25 °C temperature and 1000 W/m^2 irradiation which is the standard test conditions (STC) as shown in Figure 8.

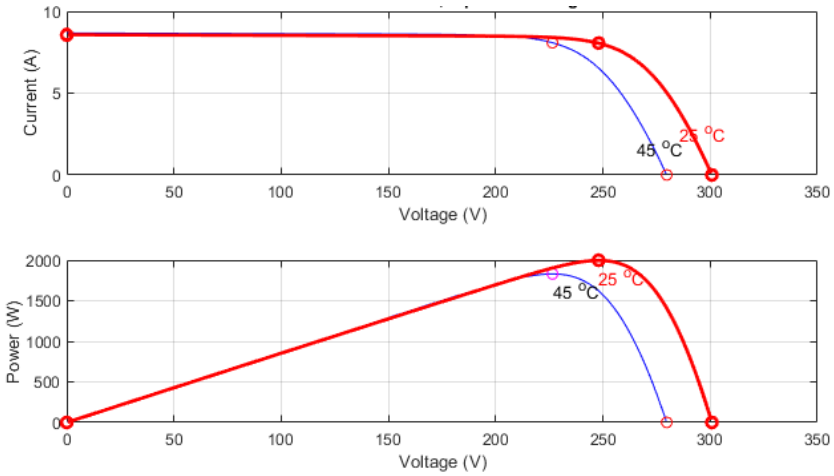

Figure 8. I-V and P-V characteristic curve of the PV module.

The boost converter has the parameters of L = 3 mH, C = 1 μF. The inverter is a full bridge single phase inverter. The PWM signals are produced using sinusoidal pwm technique within the PWM Pulse Generator block.

PWM technique comprises a compare of the high frequency triangular carrier signal with a low frequency sinusoidal reference signal. The controller is a PI type controller having proportional constant P= 0.0001 and integral constant Ki = 1. These parameters are obtained by trial and error. The load is a RL type load with R = 400 W and L = 1 mH.

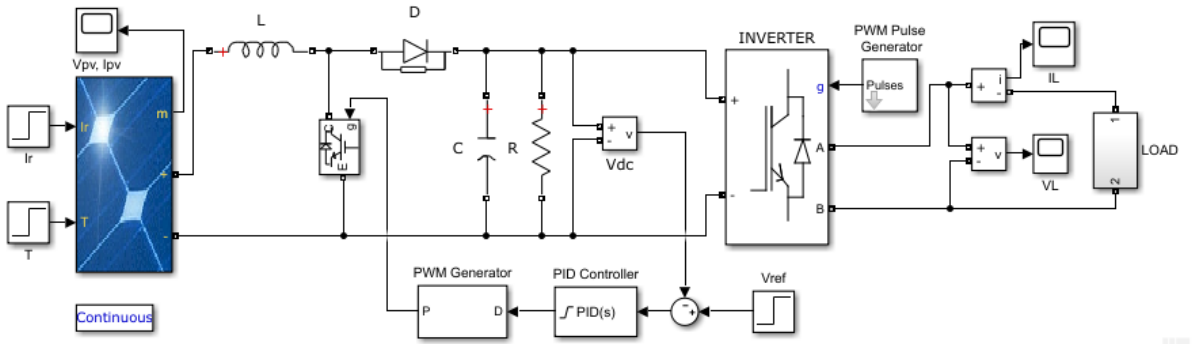

Figure 9. Simulink block of the converter-inverter system.

The system given in Figure 9 is simulated and results are presented. The voltage obtained from PV module vary with the environmental changes such as temperature and illumination or partial shading. To see the effect of input voltage variations on dc link voltage, only the results with abrupt changes in input voltage is presented here. The input voltage variation is shown in Figure 10. The Figure 10 shows the dc link voltage which is the output voltage of the boost converter when a step change in input voltage from 240 V to 280 V and then 280 V to 200 V occur.

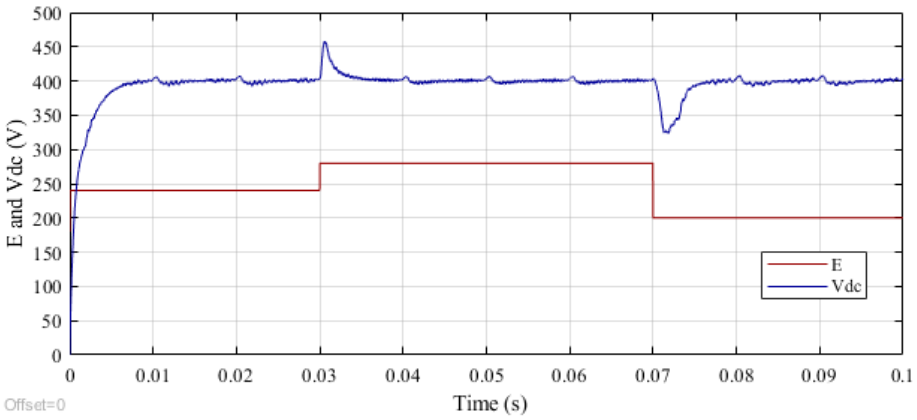

Figure 10. Dc link voltage of the inverter when changes in input voltage of boost converter occur.

The reference voltage command is 400V. It can be seen in Figure 10 that the output voltage of the boost converter reaches and follows the reference voltage even in input voltage change which occurs at t = 0.03 s and t=0.07 s. The Load voltage and current waveforms are presented in Figure 11 and Figure 12 respectively.

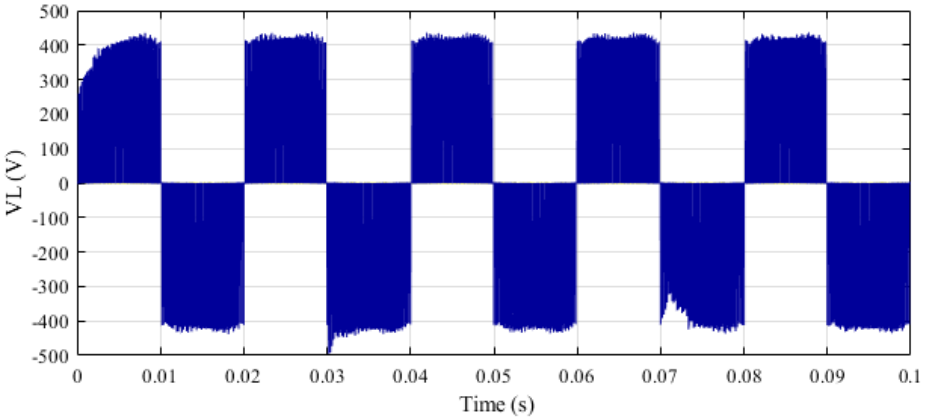

Figure 11. Inverter output voltage waveform.

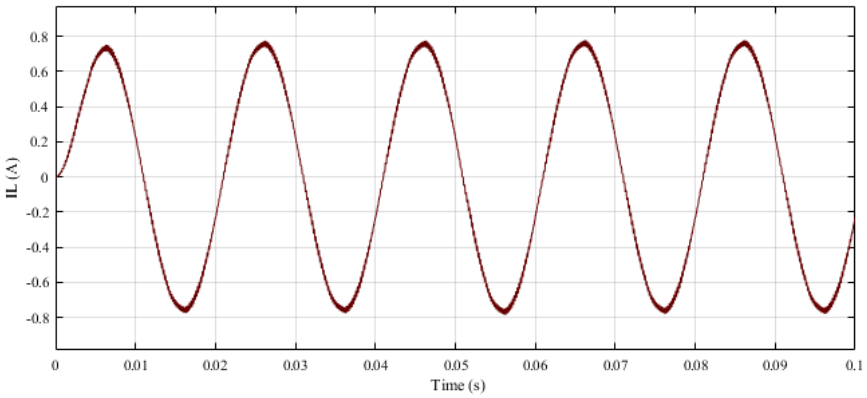

Figure 12. Load current waveform.

Figure 13 shows the dc link voltage waveform. The figure is obtained while the system is running with 350 V reference dc link voltage, this reference voltage is changed to 400 V at time t = 0.005 s. The input voltage of the boost converter maintained constant at 200 V. As it is clearly seen in the figure the dc link voltage follows the reference voltage command.

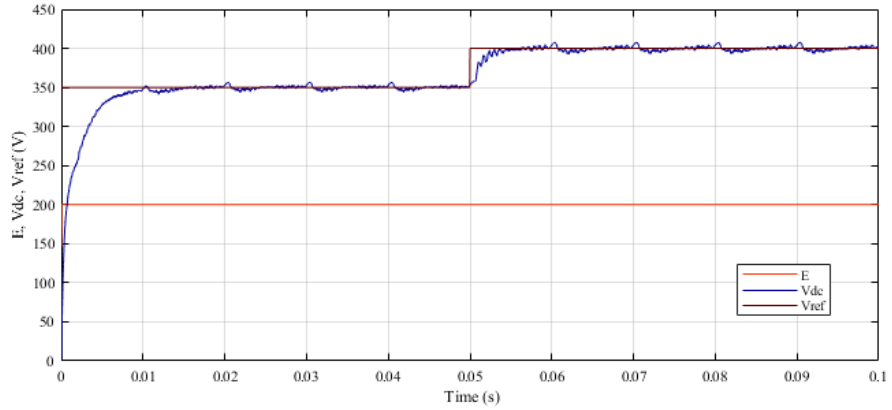

Figure 13. Dc link voltage of the inverter when refernce voltage is changed from 350 V to 400 V at t = 0.05 s.

7. Conclusion

In this study, dc link voltage control of an inverter is presented. The inverter dc link voltage is obtained from a boost converter which is powered by a photovoltaic solar module. A conventional PI controller is used to control

the dc link voltage of the inverter which is actually the output voltage of the boost converter. As the voltage obtained from solar PV module is dependent the climatic conditions such as temperature and irradiation, the system is simulated to obtain the output voltage with input voltage variations. The reference voltage command change is also provided to see the reference tracking performance of the system. The system is simulated using Simulink. Some of the obtained results are presented which show the effectiveness of the dc link voltage control of a boost-converter inverter system presented in this study. In the presented scheme, output voltage of boost converter follows the reference command voltage very closely even with input voltage and reference voltage changes. The system is insensitive to input voltage variations due to climatic environmental conditions and produces a constant dc link voltage for the load. Thus, this system can be used with off-grid applications requiring constant voltage.

References

[1] Sheila JH, Alicen K. Renewable Energy Applications for Existing Buildings. Oak Ridge, TN, USA: US Department of Energy, 2011.

[2] Taibi E, Gielen D, Bazilian M. The potential for renewable energy in industrial applications. Renewable Sustainable Energy Rev 2012; 16(1): 735-744.

[3] Chel A, Kaushik G. Renewable energy for sustainable agriculture. Agron. Sustainable Dev 2011; 31(1): 91-118.

[4] Singh GK. Solar power generation by PV (photovoltaic) technology: a review. Energy 2013; 53: 1-13.

[5] Van Campen B, Guidi D, Best G. Solar Photovoltaics for Sustainable Agriculture and Rural Development. Rome: FAO Publication, 2000.

[6] Duranay ZB, Guldemir H. Modelling and simulation of a single phase standalone PV system. In: ECAI 2019 International Conference, 11th Edition Electronics, Computers; 27-29 June 2019; Pitesti, Romania.

[7] Akikur RK, Saidur R, Ping HW, Ullah KR. Comparative study of stand-alone and hybrid solar energy systems suitable for off-grid rural electrification: a review. Renewable Sustainable Energy Rev 2013; 27: 738-752.

[8] Ghafoor A, Munir A. Design and economics analysis of an off-grid PV system for household electrification. Renewable Sustainable Energy Rev 2015; 42: 496-502.

[9] Sukamongkol Y, Chungpaibulpatana S, Ongsakul W. A simulation model for predicting the performance of a solar photovoltaic system with alternating current loads. Renewable energy 2002; 27(2): 237-258.

[10] Guldemir H. Sliding mode control of DC-DC boost converter. Journal of Applied Sciences 2005; 5(3): 588-592.

[11] Habetler TG, Naik R, Nondahl TA. Design and implementation of an inverter output LC filter used for dv/dt reduction. IEEE Trans Power Electron 2002; 17(3): 327-331.

[12] Kim SJ, Sul SK. A novel filter design for suppression of high voltage gradient in voltage-fed PWM inverter. In: IEEE Appl Power Electron Conf; 27 February 1997; Atlanta, GA, USA. pp. 122–127

[13] Von Jouanne A, Rendusara D, Enjeti P, Gray W. Filtering techniques to minimize the effect of long motor leads on PWM inverter-fed AC motor drives. In: IEEE/IAS Ann Meeting Conf; 8-12 October 1995; Orlando, FL, USA. pp. 37–44.

[14] Steinke J, Stulz C, Pohjalainen P. Use of a LC filter to achieve a motor friendly performance of the PWM voltage source inverter. In: 1997 Int. Electric Mach. Drives Conf., 2001.

[15] Renzhong X, Lie X, Junjun Z, Lie D. Design and research on the LCL filter in three-phase PV grid-connected inverters. International Journal of Computer and Electrical Engineering 2013; 5(3): 322-325.

[16] Liserre M, Blaabjerg F, Hansen S. Design and control of an LCL-filter-based three-phase active rectifier. IEEE Trans Ind Appl 2005; 41(5); 1281-1291.

[17] Ahmad AA, Abrishamifar A, Farzi M. A new design procedure for output LC filter of single phase inverters. In: 3rd International Conference on Power Electronics and Intelligent Transportation System; January 2010; China. pp. 86-91.

[18] Pavkovic D, Kristovic P, Hrgetic M,Komljenovic A, Uzarevic V. Single phase AC inverter current PR control with auxiliary PI controller for DC current suppression. In: IEEE EUROCON 2017-17th International Conference on Smart Technologies; 6-8 July 2017; Ohrid, Macedonia. pp. 324-329.

[19] Terzic B, Majic G, Slutej A. Stability analysis of three-phase PWM converter with LCL filter by means of nonlinear model. Automatika 2010; 51(3): 221-232.

[20] Reznik A, Simoes MG, Al-Durra A, Muyeen SM. LCL filter design and performance analysis for grid-interconnected systems. IEEE Trans Ind Appl 2014; 50(2): 1225-1232.

[21] Casadei D, Grandi G, Rossi C. Single-phase single-stage photovoltaic generation system based on a ripple correlation control maximum power point tracking. IEEE Trans Energy Convers 2006; 21(2): 562-568.

[22] Duranay ZB, Guldemir H, Tuncer S. Fuzzy sliding mode control of DC-DC boost converter. Engineering, Technology and Applied Science Research 2018; 8(3): 3054-3059.

Turkish Journal of Science & Technology
15(2), 93-99, 2020

Investigation of the relationships of the students' academic level and gender with Covid-19 based anxiety and protective behaviors: A data mining approach

Dönüş ŞENGÜR*
Department of Educational Sciences, Faculty of Education, Firat University, Elazig, Turkey
*dsengur@firat.edu.tr

(Geliş/Received: 07/06/2020; Kabul/Accepted: 13/08/2020)

Abstract: COVID-19, a new virus, has been caused an outbreak in all around the world. It has affected almost all parts of our lives such as working habits. The life of human beings has come to a halt. People have started to work in their homes. Besides, education activities from preschool to the colleges have canceled and distance courses took place instead of face to face education. This situation has caused fear and anxiety. Especially for students, the anxiety level about education has increased during the pandemic. In this study, the relationship of the students' academic level and gender with Covid-19 based anxiety and protective behaviors is investigated based on the data mining approach. To this end, an association rule-based classification (ARC) method is employed. Moreover, other classification approaches namely decision trees (DT), support vector machines (SVM) and k-nearest neighbor (k-NN) are also used. The ARC is used to detect the association rules between items of the dataset and obtained rules are used to construct a classifier. To detect the relationships between the students' academic level and gender with COVID-19 based anxiety and protective behaviors, a dataset, which was constructed from 215 university students by using an online self-administered questionnaire, is considered in experimental studies. The dataset covers three instruments namely Anxiety Scale (AS) with 10 items, Protective Behaviors Scale (PBS) with 14 items, and Related Knowledge Scale (RKS) with 12 items, respectively. The experimental results show that the proposed data mining approaches produce satisfactory results in determining the relationship between the students' academic level and gender with Covid-19 based anxiety and protective behaviors.

Key words: COVID-19, students' anxiety level, data mining, prediction, rule mining.

Öğrencilerin akademik düzeyi ve cinsiyetinin Covid-19 temelli kaygı ve koruyucu davranışlarla ilişkisinin incelenmesi: Bir veri madenciliği yaklaşımı

Öz: Yeni bir virüs olan COVID-19, tüm dünyada salgına neden oldu. Çalışma alışkanlıkları gibi hayatımızın hemen hemen her alanını etkiledi. İnsanın hayatı durma noktasına geldi. İnsanlar evlerinde çalışmaya başladılar. Ayrıca okul öncesi eğitimden kolejlere kadar olan eğitim faaliyetleri iptal edilmiş ve yüz yüze eğitim yerine uzaktan eğitimler verilmiştir. Bu durum korkuya ve endişeye neden oldu. Pandemi sırasında özellikle öğrenciler için eğitimle ilgili kaygı düzeyi artmıştır. Bu çalışmada öğrencilerin akademik düzeyi ve cinsiyetinin Covid-19 temelli kaygı ve koruyucu davranışlarla ilişkisi veri madenciliği yaklaşımına dayalı olarak incelenmiştir. Bu amaçla, bir ilişki kuralı tabanlı sınıflandırma (KTS) yöntemi kullanılır. Ayrıca, karar ağaçları (KA), destek vektör makineleri (DVM) ve k-en yakın komşu (k-NN) gibi diğer sınıflandırma yaklaşımları da kullanılmaktadır. KTS, veri kümesinin öğeleri arasındaki ilişki kurallarını tespit etmek için kullanılır ve elde edilen kurallar bir sınıflandırıcı oluşturmak için kullanılır. Öğrencilerin akademik düzeyi ve cinsiyeti ile COVID-19 temelli kaygı ve koruyucu davranışlar arasındaki ilişkiyi saptamak için, 215 üniversite öğrencisinden çevrimiçi kendi kendine uygulanan bir anket kullanılarak oluşturulmuş bir veri seti deneysel çalışmalarda ele alınmıştır. Veri seti, sırasıyla 10 maddelik Kaygı Ölçeği (KÖ), 14 maddeli Koruyucu Davranışlar Ölçeği (KDÖ) ve 12 maddelik İlgili Bilgi Ölçeği (İBÖ) olmak üzere üç aracı kapsamaktadır. Deneysel sonuçlar, önerilen veri madenciliği yaklaşımlarının, öğrencilerin akademik düzeyi ve cinsiyeti ile Covid-19 temelli kaygı ve koruyucu davranışlar arasındaki ilişkiyi belirlemede tatmin edici sonuçlar ürettiğini göstermektedir.

Anahtar kelimeler: KOVID-19, öğrencilerin kaygı düzeyleri, veri madenciliği, tahmin, kural madenciliği.

1. Introduction

COVID-19, which caused a pandemic worldwide, has been first appeared in Wuhan city of China in the last days of 2019 [1]. Although the disease initially looked like the ordinary flu, over time it became clear how dangerous the disease was. The disease has had many negative effects on our lives. Due to the disease, some concepts such as working from home, education with distance courses and curfew became to be a part of our lives. Students, who are an enormous group, affected by the COVID-19 pandemic. Students have started to get their courses by distance courses and have had to stay at home due to the curfew. This situation brings anxiety and

* Corresponding author: dsengur@firat.edu.tr. ORCID Number of author: 0000-0002-8786-6557

mental tiredness to the students. During the pandemic term, researchers have investigated how to measure the psychology situation of the students based on some instruments [2]. Riad et al. [2] developed instruments to evaluate COVID-19 based anxiety level, protective behaviors, and knowledge towards the COVID-19. A self-administered questionnaire was developed and used for data collection from 215 university students who were from Europe and China via social networks, respectively. The authors used item-total analysis and confirmatory factor analysis models for evaluating the collected dataset. The results showed that the developed instruments were promising for measuring the psychological effects of COVID-19. Trung et al. [3] investigated the learning habits of the Vietnamese students during the COVID-19 pandemic. The authors spread an online questionnaire on a network of educational communities over social networks to construct a dataset. Cao et al. [4] evaluated the mental situation of medical school students in China during the COVID-19 pandemic. A 7-item questionnaire, which examines the anxiety disorder levels of the participant, was used to collect the dataset. 7143 students were recruited in the dataset. Several statistical analyses were carried out on the collected dataset and some important findings were reported. Odriozola-González et al. [5] evaluated the mental impact of COVID-19 on university students during the pandemic lockdown in Spain. Anxiety, depression and stress levels of the students were measured and collected in a dataset by using an online questionnaire. 2530 students from the University of Valladolid were recruited in the study. The statistical analysis over-collected dataset revealed that students were suffered an important mental impact during the pandemic. Bitan et al. [6] investigated the degree of the fear factor of COVID-19 in Israel. Besides fear, anxiety, depression and stress level of the participants were saved into a dataset. 639 participants were used in the construction of the dataset and the two-factor structure model was used in the evaluation of the collected dataset. Authors reported that gender and chronic illness were two important factors associated with the fear of COVID-19. Zhang et al. [7] evaluated the adverse impact of the COVID-19 pandemic on Chinese students' anxiety and depression levels. An online questionnaire, which measured the demographics, physical activity, negative emotions, sleep quality, and aggressiveness level of the participants, were used on 66 students to construct the dataset. The authors used a mixed-effect model to evaluate the associations between variables. The authors also investigated the mediating effect of sleep quality. Kaparounaki et al. [8] explored students' psychological state during the pandemic lockdown. An online questionnaire was used to collect the dataset over 1000 university students. The depression, anxiety level and suicidal thoughts of the students were recorded by using the questionnaire. The results showed that there have been increases in anxiety, depression and suicidal thoughts, respectively.

As mentioned earlier, COVID-19 has been affected the whole world in almost all parts such as economy, lifestyle, education, travel etc. Education, which is an important part of our lives, has affected deeply. Especially, students' anxiety level, protective behaviors and knowledge scales have been changed due to the pandemic. In this work, it was aimed to shown the relationship between students' anxiety level, protective behaviors and knowledge scales and academic level and gender during the pandemic. To this end, various datamining techniques have been used for prediction purposes. As the recent literature is reviewed, it is seen that the researchers generally applied online questionnaires and collected datasets for measuring the students' mental health during the COVID-19 pandemic. In this study, data mining and machine learning techniques are used to determine the relationship between the students' academic level and gender with COVID-19 based anxiety and protective behaviors. The dataset, which was collected in [2], is considered in this study. 215 university students were recruited during the dataset collection where an online self-administered questionnaire was used. The questionnaire covered three instruments namely Anxiety Scale (AS) with 10 items, Protective Behaviors Scale (PBS) with 14 items, and Related Knowledge Scale (RKS) with 12 items, respectively. ARC method, which is generally used to detect the association rules between items of the dataset, is employed for gender and academic level prediction. Besides, DT, SVM and k-NN methods are further used for prediction and comparison purposes. The accuracy is used as the measure of validation of the proposed work. The obtained results reveal that data mining and machine learning are a promising tool for such applications.

The remainder of this paper is as follows. The next section introduces the background theories. The apriori algorithm and ARC theories are briefly introduced in Section 2. Section 3 describes the dataset, experimental works and results. The paper is concluded in Section 4.

2. Background Theories

This section briefly introduced the theories of the data mining approaches namely the apriori algorithm and ARC method [9, 10]. Readers may refer to [11, 12] for detailed information about the mentioned methods.

2.1. Apriori Algorithm

Apriori algorithm is known as the basic and ancient method in association rule mining [9]. Many new approaches have been developed based on the concept of the Apriori algorithm [13-15]. Apriori algorithm mines the frequent itemsets in as given set of transactions. Apriori algorithm produces the rules based on the support and confidence values. While the support is defined as the ratio of the total number of records of transactions that include all items in the antecedent and consequent parts of the rule, the confidence is defined as the percentage of the number of transactions that include all items in the consequent, as well as the antecedent, to the number of transactions that include all items. Lift is another metric that is used to evaluate the significance and reliability of a rule. The rules are generally in the form of A → B where A shows the antecedent part of the rule and B indicates the consequent part of the rule, respectively. Equations 1, 2, 3 and 4 show the rule, support, confidence and lift measures, respectively.

$$Rule: A \rightarrow B \tag{1}$$

$$Support = \frac{frq(A,B)}{N} \tag{2}$$

$$Confidence = \frac{frq(A,B)}{frq(A)} \tag{3}$$

$$Lift = \frac{Support}{Support(A).Support(B)} \tag{4}$$

where ‘frq’ shows the frequency.

2.2. Associative rules-based classification

ARC is a supervised rule-based classifier, which uses the rules that are obtained by the apriori algorithm [16]. Initially, the frequent items that meet the minimum confidence threshold are saved for rule-based classifier construction. The saved rules, whose consequent parts are restricted to the class label, are further selected for classification purposes. A heuristic approach is employed for ranking the selected rules according to their confidence values and the rules that cover the training samples are selected.

The ARC algorithm initially selects the best rule and then eliminates all the covered examples. If at least one example meets the rule conditions, this rule will be added to the final rules. This procedure is repeated until there are no more rules to select or no other samples within the scope. The algorithm then stops and returns the classifier in the form of the if-then-else rule list.

3. Experimental studies and results

3.1. Dataset

The students' anxiety level and protective behaviors dataset were constructed based on 215 university students from 17 counties [2]. An online, functionality and user-friendly questionnaire, which was spread between March 25th-27th 2020 via social networks, contained demographic information and three instruments namely anxiety scale with 10 items, protective behaviors scale with 14 items, and knowledge scale with 12 items. For anxiety and protective behavior scales, a 5-point Likert scales with 10 and 14 items were used, respectively. For anxiety scale "1" referred to "Totally disagree" and "5" referred to the "Totally agree". Similarly, for protective behaviors scale, “1” referred to “Not at all like me” and “5” referred to “Just like me”. For the knowledge scale, a multi-choice approach was adopted. Each item has four available options where one of them is the right option. More detailed information can be seen in [2]. The distributions of the recordings among the classes such as academic level and gender are given Table 1.

Table 1. The distribution of the recordings among the classes

Academic level	Bachelor	Masters	Doctoral
	152	49	14
Gender	Male	Female	
	173	42	

3.2 Results and Discussions

All coding was carried out with MATLAB on a computer equipped with NVIDIA Quadro M4000 GPU and Intel(R) Xeon(R) CPU E5-1650 @3.60 GHz 64 GB memory. Five-fold cross-validation technique and average accuracy score were used in experiments for evaluation of the proposed method. The accuracy is defined as the ratio of the number of correct classifications to the number of all samples in the dataset. In the experiments, both academic level and gender were used as output. While gender output has two labels, the academic level has three labels such as "bachelor", "masters" and "doctoral", respectively. Besides, anxiety, protective behaviors and knowledge scales were both used independently and concatenated forms. For ARC, the selection of the minimum support and gain values were carried out with a grid search algorithm. The minimum gain value was used for selecting the best rules. The support values were in the range of 10^{-2} and 1 and the gain values were in the range of 10^{-3} and 2, respectively. Moreover, the number of the best rules was fixed to five. This value was found heuristically during the experimental works. The initial experiments were carried out on an anxiety scale. Figure 1 shows the grid search results for anxiety scale vs gender classification. While the x-axis shows the minimum support values, the y-axis shows the minimum gain values. The z-axis indicates the accuracy scores.

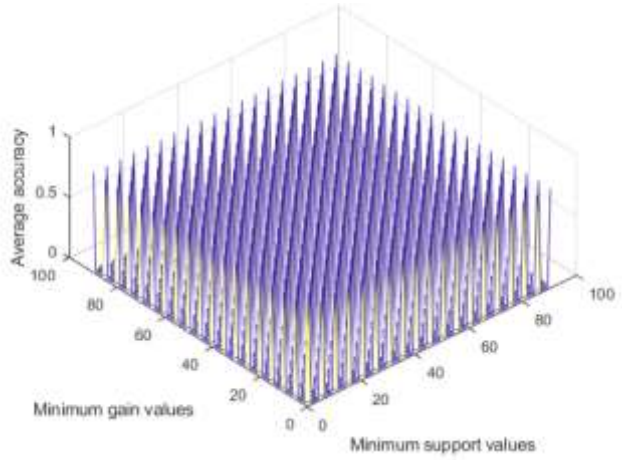

Figure 1 Grid search on an anxiety scale

Table 2 also shows the average accuracy scores for anxiety scale based academic level and gender classification. As seen in Table 2, by using anxiety scale, the academic level and the gender of the participants were classified with 73.95% and 79.93% average accuracy scores, respectively.

Table 2 Average accuracy scores for Anxiety scale

Anxiety Scale	**Average Accuracy**
Academic level	73.95%

Gender	79.93%

Table 3 gives the average prediction scores for the scale of protective behavior. As seen, 70.70% and 80.40% average accuracy scores were obtained for academic level and gender, respectively. Gender classification was carried out better than the academic level classification.

Table 3 Average accuracy scores for protective behaviors scale

Anxiety Scale	**Average Accuracy**
Academic level	70.70%
Gender	80.40%

Table 4 was constructed for giving the classification achievements for the knowledge scale. While the academic level was predicted with a 66.50% average accuracy score, 77.21% score was produced for gender class.

Table 4 Average accuracy scores for knowledge scale

Anxiety Scale	**Average Accuracy**
Academic level	66.50%
Gender	77.21%

From Tables 2, 3 and 4, it was seen that for single scales, the scale of the protective behavior produced the high average accuracy score for gender class and the academic level was predicted better with the anxiety scale. It is worth mentioning that the knowledge scale generally produced low average accuracy score when compared with the anxiety and protective behaviors scales, respectively.

Table 5 Average accuracy scores for anxiety + protective behaviors scales

Anxiety Scale	**Average Accuracy**
Academic level	74.16%
Gender	80.47%

In Table 5, the results that were obtained via the concatenation of the anxiety and protective behavior scales were given. One important observation was that the concatenation of the scales improved the classification accuracy scores. 74.16% and 80.47% average accuracy scores were obtained for academic level and gender classes, respectively.

Table 6 Average accuracy scores for anxiety + knowledge scales

Anxiety Scale	**Average Accuracy**
Academic level	74.16%
Gender	79.07%

The average accuracy scores for concatenated anxiety and knowledge scales were given in Table 6. As compared in Tables 5 and 6, both concatenated anxiety and protective behaviors and anxiety and knowledge scales produced the identical average accuracy scores for academic level class. Besides, a 79.07% average accuracy score was produced for the gender class as seen in Table 6.

Table 7 Average accuracy scores for protective behaviors + knowledge scales

Anxiety Scale	**Average Accuracy**
Academic level	75.77%
Gender	80.93%

The achievements for concatenated protective behaviors + knowledge scales were given in Table 7. As seen in Table 7, a 75.77% average accuracy score was obtained for academic level class and an 80.93% average accuracy score was produced for gender class.

Table 8 Average accuracy scores for anxiety + protective behaviors + knowledge scales

Anxiety Scale	Average Accuracy
Academic level	79.43%
Gender	82.33%

Finally, the achievements for concatenation of all scales were given in Table 8. A 79.43% average accuracy score was produced for academic level and an 82.33% average accuracy score was obtained for gender class.

Comparison of the obtained results for concatenation of the anxiety, protective behaviors and knowledge scales with some of the existing machine learning techniques were tabulated in Table 9. MATLAB Classification Learner Tool (MCLT) was used for comparison purposes. The default setting parameters of compared methods in MCLT was used. DT is a flow chart, such as a tree structure, where each inner node represents a test on an attribute, each branch represents a result of the test, and each leaf node (terminal node) contains a class tag [17]. Given a set of training examples, each marked as one or the other of two categories, an SVM training algorithm makes new examples to one category or another making it an unlikely binary linear classifier [18]. The output in the k-NN classification is a class member. An object is classified by the plural vote of its neighbors; the object is assigned to the class most common among its closest neighbors. If k = 1, the object is assigned to the class of the nearest neighbor [19].

Table 9 Performance comparison of average accuracy scores for anxiety + protective behaviors + knowledge scales

	Academic level	Gender
DT	61.4%	71.2%
SVM	74.9%	81.4%
k-NN	72.6%	80.5%
ARC	79.4%	82.3%

From Table 9, it is observed that the ARC produced the highest average accuracy scores for both academic level and gender. The second-best average accuracy scores were produced by the SVM technique. SVM produced 74.9% and 81.4% average accuracy scores for academic level and gender classes, respectively. k-NN yielded the third-best accuracy scores where 72.6% and 80.5% average accuracy scores were obtained for academic level and gender. Finally, the worst results, where 61.4% and 71.2% average accuracy scores produced for academic level and gender classes, were obtained by the DT method.

4. Conclusions

In this paper, the prediction of the students' academic level and gender with COVID-19 based anxiety and protective behaviors was investigated based on data mining and machine learning approach. A rule-based classifier namely ARC method was employed for this purpose. Besides, DT, SVM and k-NN methods were also used. The ARC was used to detect the association rules between items of the dataset and obtained rules are used to construct a classifier. To detect the relationships between the students' academic level and gender with COVID-19 based anxiety and protective behaviors, a dataset, which was constructed from 215 university students by using an online self-administered questionnaire, is considered in experimental studies. The following conclusions are extracted from the study.

1-) From the experimental analysis, it was seen that data mining and machine learning techniques have potential in the use of finding relationships between COVID-19 based anxiety, protective behaviors and knowledge scales and the academic level and gender of the students.

2-) Prediction of the gender was achieved better than the prediction of the academic level. This might be based on the number of class labels as the academic level has three class labels.

3-) Using multi scales has increased the prediction performance greatly.

In the future works, we are planning to construct a dataset for Turkish students and examine the effect of the COVID-19 on Turkish students' anxiety level and protective behaviors.

References

[1] World Health Organization. IHR Emergency Committee on Novel Coronavirus (2019-nCoV) (2020).
[2] Riad A, Huang Y, Zheng L, & Elavsky S. COVID-19 Induced Anxiety and Protective Behaviors During COVID-19 Outbreak: Scale Development and Validation. medRxiv 2020.
[3] Trung T, Hoang AD, Nguyen TT, Dinh VH, Nguyen YC, & Pham HH. Dataset of Vietnamese student's learning habits during COVID-19. Data in Brief 2020; 105682.
[4] Cao W, Fang Z, Hou G, Han M, Xu X, Dong J, & Zheng J. The psychological impact of the COVID-19 epidemic on college students in China. Psychiatry research 2020; 112934.
[5] Odriozola-González P, Planchuelo-Gómez Á, Irurtia MJ, & de Luis-García R. Psychological effects of the COVID-19 outbreak and lockdown among students and workers of a Spanish university. Psychiatry Research 2020; 113108.
[6] Bitan DT, Grossman-Giron A, Bloch Y, Mayer Y, Shiffman N, & Mendlovic S. Fear of COVID-19 scale: Psychometric characteristics, reliability and validity in the Israeli population. Psychiatry Research 2020; 113100.
[7] Zhang Y, Zhang H, Ma X, & Di Q. Mental Health Problems during the COVID-19 Pandemics and the Mitigation Effects of Exercise: A Longitudinal Study of College Students in China. International Journal of Environmental Research and Public Health 2020; 17(10), 3722.
[8] Kaparounaki CK, Patsali ME, Mousa DPV, Papadopoulou EV, Papadopoulou KK, & Fountoulakis KN. University students' mental health amidst the COVID-19 quarantine in Greece. Psychiatry Research 2020; 113111.
[9] Agrawal R, Imieliński T, Swami A. Mining association rules between sets of items in large databases. In: Proceedings of the 1993 ACM SIGMOD international conference on management of data, Washington DC, 25-28 May 1993. New York: ACM, 207–216
[10] Cano A, Zafra A, Ventura S. An interpretable classification rule mining algorithm. Information Sciences 2013; 240: 1–20.
[11] Agrawal R, Mannila H, Srikant R, Toivonen H, Verkamo AI. Fast discovery of association rules. Advances in Knowledge Discovery and Data Mining 1996; 12: 307–328.
[12] Hasanpour H, Meibodi RG, & Navi K. Improving rule-based classification using Harmony Search. PeerJ Computer Science 2019; 5: e188.
[13] Scheffer T. Finding association rules that trade support optimally against confidence. Principles of Data Mining and Knowledge Discovery 2001; 424–435.
[14] Nahar J, Imam T, Tickle KS, Chen Y-PP. Association rule mining to detect factors which contribute to heart disease in males and females. Expert Systems with Applications 2013; 40: 1086–1093.
[15] Nahar J, Tickle KS, Ali AS, Chen Y-PP. Significant cancer prevention factor extraction: an association rule discovery approach. Journal of Medical Systems 2011; 35: 353–367.
[16] Ma BLWHY, Liu B. Integrating classification and association rule mining. Proceedings of the fourth international conference on knowledge discovery and data mining, 1998.
[17] Şengür D, Tekin A. Prediction of Student's Grade Point Average by Using the Data Mining Methods, International Journal Of Informatics Technologies 2013; 6 (3) 7-16
[18] Vapnik VN (1995) The Nature of Statistical Learning Theory; Springer, New York, USA.
[19] Şengür D, Turhan M. Prediction of the action identification levels of teachers based on organizational commitment and job satisfaction by using k-nearest neighbors method. Fırat Univ Turkish J Sci Technol. 2018;13(2):61–8.

Turkish Journal of Science & Technology
15(2), 101-110, 2020

ANN-Based MPPT Algorithm for Photovoltaic Systems

Ahmet GÜNDOĞDU[1*], Reşat ÇELİKEL[2]
[1] Department of Electrical and Electronics Engineering, Faculty of Engineering, Batman University, Batman, Turkey
[*1] ahmet.gundogdu@gmail.com, [2] resat.celikel@batman.edu.tr

(Geliş/Received: 07/07/2020; Kabul/Accepted: 23/08/2020)

Abstract: It is very important to get maximum efficiency from photovoltaic panels with low yields. To be able to achieve high efficiency from panels, maximum power point tracking algorithms have been developed. Perturb&Observe and incremental conductance methods, which are among the conventional methods, are not very successful in capturing the points from which maximum power can be obtained in variable atmospheric conditions. In this article, a maximum power point tracking method based on the artificial neural network was proposed. In the proposed method, artificial neural network inputs were designed as temperature and voltage, while its output was designed as the reference voltage. By controlling this reference voltage through a PI controller, it was ensured that the system generated maximum power in variable atmospheric conditions. Conventional methods and the proposed method were compared by simulation studies conducted in the MATLAB/Simulink environment. The superiority of the proposed method was demonstrated with a compelling scenario in which temperature and radiation were constantly changing.

Key words: Photovoltaic System, Artificial Neural Networks-ANN, Boost Converter, MPPT Algorithms.

Fotovoltaik Sistemler için YSA Tabanlı MPPT Algoritması

Öz: Verimleri düşük olan fotovoltaik panellerden maksimum oranında verim elde etmek oldukça önemlidir. Panellerden yüksek verim elde etmek için maksimum güç noktası izleme algoritmaları geliştirilmiştir. Geleneksel yöntemlerden olan Değiştir&Gözle ve Artımsal İletkenlik yöntemleri, değişken atmosferik koşullarda maksimum gücün elde edileceği noktaları yakalamada çok başarılı değillerdir. Bu makalede yapay sinir ağı tabanlı bir maksimum güç noktası izleme yöntemi önerilmiştir. Önerilen yöntemde yapay sinir ağının girişleri sıcaklık ve gerilim, çıkışı ise referans gerilim olacak şekilde tasarlanmıştır. Bu referans gerilim bir PI kontrolör tarafından kontrol edilerek sistemin değişken atmosferik koşullarda maksimum güç üretmesi sağlanmıştır. Geleneksel yöntemler ile önerilen yöntem MATLAB/Simulink ortamında yapılan benzetim çalışmaları karşılaştırılmıştır. Önerilen yöntemin üstünlüğü, sıcaklık ve radyasyonun sürekli değiştiği zorlayıcı bir senaryo üzerinde gösterilmiştir.

Anahtar kelimeler: Fotovoltaik Sistem, Yapay Sinir Ağları-YSA, Yükseltici Tip Dönüştürücü, MPPT Algoritmaları.

1. Introduction

Reduced energy sources, increased environmental pollution, and global warming have increased the interest in renewable energy sources. Among the renewable energy sources, the most intensively used energy source is the sun. Since efficiencies of solar panels are low, maximum efficiency from the panels is obtained by using the maximum power point tracking (MPPT) algorithms. The ability of these MPPT algorithms to operate under variable atmospheric conditions is very important because it will increase efficiency [1].

Many studies related to MPPT algorithms have been carried out so far and it still continues to be developed today. Incremental Conductance (IC), Perturb & Observe (PO), Constant Voltage Controller (CVC), Artificial Intelligent (AI), and Hybrid methods, which were among the conventional methods, were compared [2-3]. In addition to the fact that the PO method causes oscillations that are inevitable in the steady-state, its performance is also low in variable atmospheric conditions. Therefore, modified PO methods have been developed. These algorithms have been tested and compared under variable atmospheric conditions [4-6]. In addition to modified PO methods, in another research, the superiority of a new PO algorithm, effective in partial shading conditions, was demonstrated by an experimental study [7].

The success of a variable step IC method, which was proposed as an alternative to the IC method and comprised of a table, was demonstrated experimentally [8]. High-performance MPPT algorithm studies with the Fuzzy Logic Controller (FLC) method is quite common. An MPPT algorithm, which consisted of IC and Fuzzy Logic estimator and operated with high performance in radiation changes, was experimentally realized [9]. The performances of two different hybrid MPPT algorithms consisted of PO-FLC and IC-FLC were examined in fast-

* Corresponding author: ahmet.gundogdu@gmail.com. ORCID Number of authors: [1] 0000-0002-8333-3083, [2] 0000-0002-9169-6466

changing weather conditions. It was seen that the performance of the IC-FLC hybrid algorithm was slightly superior to the performance of the PO-FLC algorithm [10]. In a different study, on the other hand, by using the System Identification (SI), a high-performance MPPT algorithm that can operate under variable atmospheric conditions was developed [11]. In this method, power generation with high performance was achieved both in temperature and radiation changes compared to the conventional methods.

The Artificial Neural Network (ANN) structure is used in motor control applications, measurement of EEG signals, and MPPT algorithms [12-14]. With the becoming prevalent of MPPT algorithms, comparison studies have been conducted to show the advantages of various algorithms [15]. In one of these studies, Particle Swarm Optimization (PSO), Genetic Algorithm (GA), PID, FL, and ANN methods were compared. Temperature and radiation values were used as input values in the ANN method [16]. In another study, a variable step ANN algorithm was developed and experimentally demonstrated to reduce high tracking performance, overshoot amount, and steady-state ripples [17]. A hybrid MPPT algorithm, which operates with high-performance both under rapidly changing atmospheric conditions and in partial shading conditions, was developed by combining the ANN and PO methods. Temperature and radiation data were used in the inputs of the ANN algorithm [18]. In another study where temperature and radiation values were used as inputs of the ANN algorithm, a comparison of conventional methods and the ANN method was made [19]. A three-layer and three-input ANN algorithm that determined the global MPP point under partial shading conditions was developed. The proposed algorithm was realized by using FPGA [20]. In another study, the ANN structure, where temperature and radiation values were used as input, was realized in the Simulink environment. It was shown that the experimental results obtained by using the proposed structure in a real system were the same as the simulation results [21].

In this study, an ANN structure with two inputs, three layers, and ten neurons was proposed to perform the MPPT algorithm in Photovoltaic (PV) power systems. In conventional ANN structures, either current and voltage information or radiation and temperature information are used as input. In the proposed ANN structure, on the other hand, voltage information and temperature information were used as input. The output information of this ANN structure constitutes the reference voltage. When the proposed method is operating under variable atmospheric conditions, it generates a reference voltage depending on the change of temperature and radiation. The reference voltage is controlled with a PI controller by comparing it with the voltage of the PV panel. The PO and IC methods, which are among the conventional methods, and the proposed method were compared by the simulation studies conducted in MATLAB/Simulink environment.

2. PV Cell Model

The model of a PV cell is seen in Figure 1. This PV cell model consists of a current source, a diode connected inversely and parallel to this current source, a parallel-connected resistor, and a series-connected resistor [22]. Mathematical equations of the PV cell model are shown in the equations between Equation 1 and Equation 3.

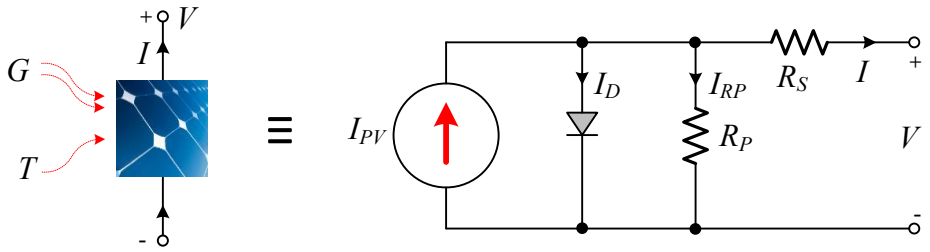

Figure 1. Electrical equivalent circuit model of PV cell

$$I = I_{PV} - I_D - I_{R_P} \tag{1}$$

$$I = I_{PV} - I_0 \left[exp\left(\frac{V+R_S I}{a}\right) - 1 \right] - \frac{V+R_S I}{R_P} \tag{2}$$

$$a = \frac{N_s n k T}{q} \tag{3}$$

where I_0 is called the reverse saturation current or leakage current of the diode. a is the ideality factor, N_s is the number of serial-connected cells, n is the diode ideality constant, k is the Boltzmann constant (1.3806503x10^{-23} J/K), T is the cell temperature (Kelvin), and q is the electron charge (1.60217646x10^{-19} C). The current generated by the PV cell by the effect of light is given in Equation 4.

$$I_{PV} = \left(I_{PV,n} + K_I(T - T_n)\right)\frac{G}{G_n} \tag{4}$$

where $I_{PV,n}$ refers to the current generated for 25 °C and 1000 W/m^2, T_n refers to the nominal temperature (Kelvin), G refers to the radiation value on the panel surface (W/m^2), and G_n refers to the nominal radiation value (W/m^2). The saturation current of the diode (I_0) is given in Equation 5.

$$I_0 = \frac{I_{SC,n} + K_I(T - T_n)}{\exp\left(\frac{V_{OC,n} + K_V(T - T_n)}{a}\right) - 1} \tag{5}$$

where $I_{SC,n}$ is the nominal short-circuit current, $V_{OC,n}$ is the nominal open-circuit voltage, K_I is current coefficient, and K_V is voltage coefficient.

Based on the cell model, the current-voltage and power-voltage graphs of a PV panel are shown in Figure 2. The current-voltage and power-voltage graphs of a 10 kW PV power system created in the MATLAB/Simulink environment in this study by depending on the cell model described above are shown in Figure 2. I-V and P-V curves of the power system are given in Figure 2(A) under a constant temperature of 25°C and for different radiation values and in Figure 2(b) under constant radiation of 1000 W/m^2 and for different temperature values.

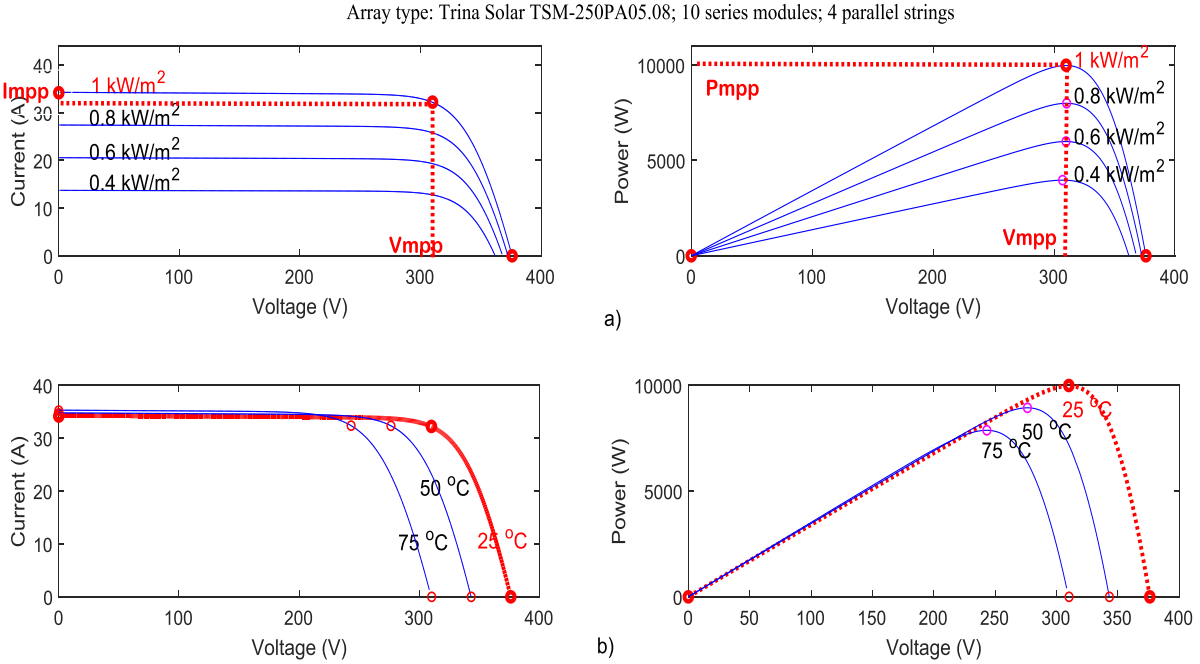

Figure 2. I-V and P-V curves of the PV system; a) at a constant 25°C and at different radiation, b) at constant 1000 W/m^2 and at different temperature values.

As can be seen in the graph, the power generation of the panel can vary depending on atmospheric conditions such as radiation and temperature. This variability affects the efficiency of the system. In terms of the efficiency of the power system, operating at a constant power point improves the efficiency of the system. In this respect, the maximum power point required for constant power applications is determined by the help of Buck-Boost converters and MPPT algorithms.

3. DC-DC Converter and System Model

The system model, consisting of a PV panel, ANN-based MPPT algorithm, and boost-type DC-DC converter is shown in Figure 3. The boost-type converter increases the V_S voltage applied to its input by depending on a specific conversion rate. The relation between the output voltage (V_0) and the input voltage (V_S) of the converter is given in Equation 6.

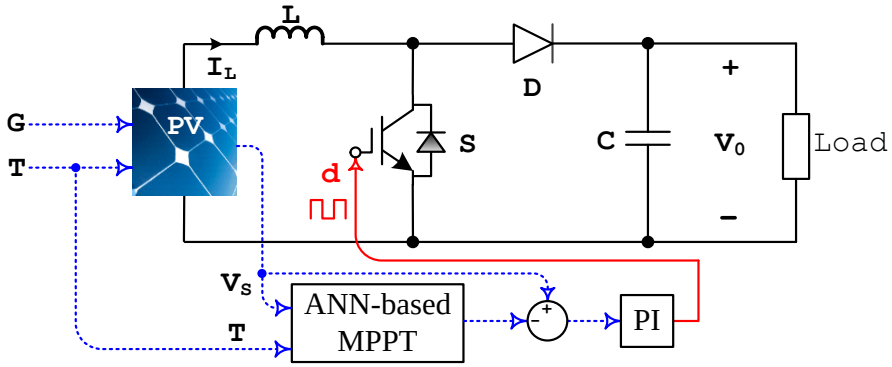

Figure 3. DC-DC Converter and System Model.

$$V_0 = \frac{V_S}{1-d} \tag{6}$$

where *d* refers to the duty cycle of the S switch, V_S refers to the panel output voltage, and V_0 refers to the converter output voltage. While the panel output voltage (V_S) is decreasing depending on atmospheric conditions, the duty cycle (*d*) is increased by the ANN-based MPPT algorithm in order to keep V_0 constant.

4. Conventional MPTT Methods

4.1. PO Method

In the conventional PO method, the magnitude of the step voltage change (ΔV_{ss}) at each step is constant. Therefore, for different values of ΔV_{ss}, the error amount and speed of the system response will be different. Small step changes reduce oscillations around the maximum power point, while they increase the time to reach maximum power. In large step changes, on the other hand, the maximum power point is reached much faster, but the oscillations that occur in the power around the maximum power point increase. In fast-changing weather conditions, this method either fails to track the MPP point or tracks it in such a way that it causes massive time and power losses. As seen in Figure 4(a), while the voltage increases in the blue zone to the left of the P_{MPP} point, the power also increases. In the Orange area to the right, on the other hand, while the voltage is increasing, the power is decreasing. $P_A<P_B$ at the right of Point B, while PA>PB at the region to the left of it. Depending on the magnitude of the step-change, this condition can lead to an error in the calculation of power, and therefore, it is considered a disadvantage of the PO method.

4.2. IC Method

The conventional IC algorithm operates according to the principle of I/V exchange. In this method, the measured instantaneous voltage and current values are compared with the previous voltage and current values. The maximum power point is attempted to be captured by comparing the obtained increasing conductivity value ($\Delta I/\Delta V$) with the instantaneous conductivity (I/V). The output power at the P_{MPP} point where the maximum power is obtained from the PV system is expressed with Equation 7.

$$P_{MPP} = V_{MPP} x I_{MPP} \tag{7}$$

Equation 7 is shown in the differential equation as follows.

$$\frac{dP}{dV} = \frac{d(IV)}{dV} = I + V\frac{dI}{dV} \tag{8}$$

$$\frac{dI}{dV} \cong \frac{\Delta I}{\Delta V} \tag{9}$$

$$\frac{dP}{dV} = \frac{d(IV)}{dV} = I + V\frac{\Delta I}{\Delta V} \tag{10}$$

If Equation 10 is solved for 3 different regions shown in Figure 4(b); it is obtained;

in the blue zone to the left of the P_{MPP} point $$\frac{dP}{dV} > 0,\ \frac{\Delta I}{\Delta V} > -\frac{I}{V} \tag{11}$$

at the P_{MPP} point $$\frac{dP}{dV} = 0,\ \frac{\Delta I}{\Delta V} = -\frac{I}{V} \tag{12}$$

in the orange zone to the right of the P_{MPP} point $$\frac{dP}{dV} < 0,\ \frac{\Delta I}{\Delta V} < -\frac{I}{V} \tag{13}$$

This method requires a high sampling rate in the tracking of the power change.

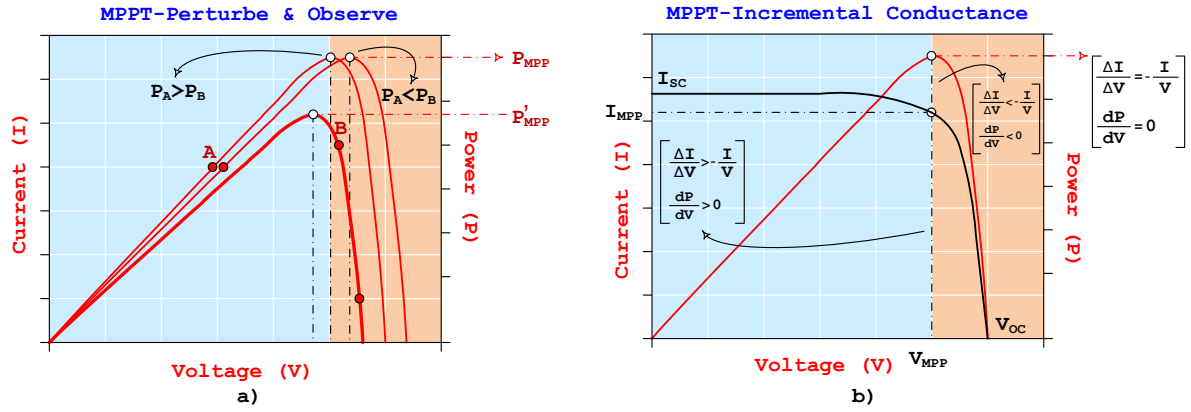

Figure 4. Conventional MPPT methods. a) Perturbe&Observe, b) Incremental Conductance

4.3. The Proposed ANN Model

In recent years, ANN has been being used for estimation and control purposes both in many different systems and in MPPT algorithms. There are quite a lot of studies related to this subject in the literature. ANN is a computation tool often used in nonlinear systems. It is defined by the properties of biological neurons, which consist of weighted connections used to send signals to each other. The weights used in the input values are set by the learning rule in the training process. In this study, an ANN structure with two inputs, ten neurons, and one output was proposed and it is shown in Figure 5.

As shown in Equation 14, the mapminmax function used in the ANN structure is used to normalize input values. In the hidden layer, the tansig function given in Equation 15 was used as the activation function. Normalized values are converted to their normal values using the mapminmax_reverse function in Equation 16.

$$mapminmax = \frac{(x-x_{min})(x_{max}-x_{min})}{(y_{max}-y_{min})} + y_{min} \tag{14}$$

$$tansig = \frac{2}{e^{-2x}+1} - 1 \tag{15}$$

$$mapminmax\_rever. = \frac{(x-y_{min})(x_{max}-x_{min})}{(y_{max}-y_{min})} + x_{min} \tag{16}$$

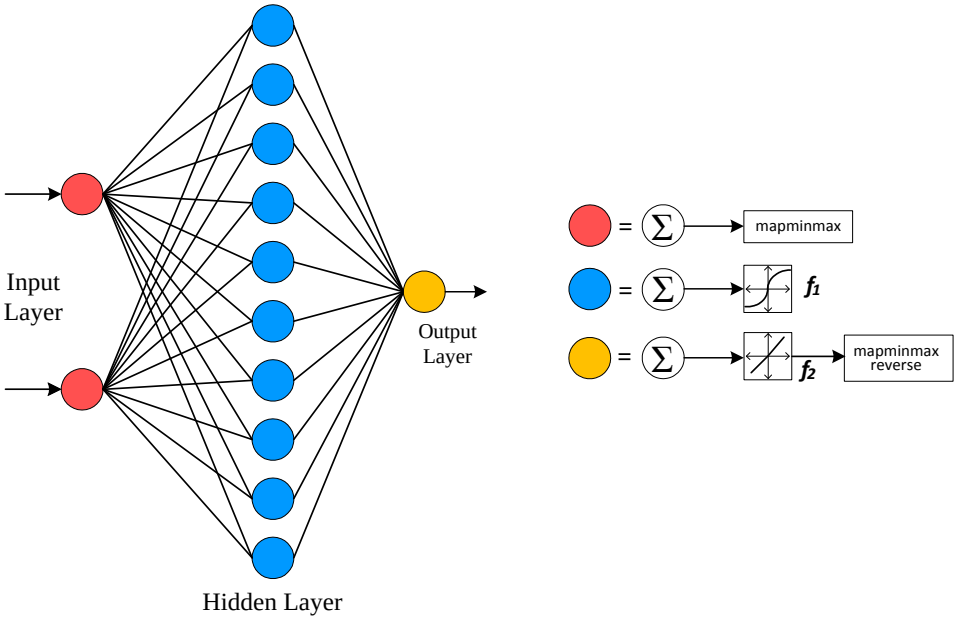

Figure 5. The proposed ANN structure.

As seen in Equation 14, the output neuron is obtained by summing each of the input signals after they were multiplied by the connection weights.

$$y_j = f\left(\sum w_{ij} x_i + b\right) \tag{17}$$

where f is the activation function, w_{ij} is the connection weight, x_i is the input signal, b is the deviation value, and y_j is the output neuron. The sum of the difference between the desired output value and the obtained value is seen in Equation 18.

$$E = \frac{1}{2}\sum_j \left(y_{dj} - y_j\right)^2 \tag{18}$$

where y_{dj} refers to the desired output value. In this study, the data required for the training of ANN were obtained in the MATLAB/Simulink environment. The number of data obtained for each input was 350000. 175000 of these data were used for training purposes, 70000 for verification purposes, and 105000 for testing purposes. As training algorithms, three different methods, Levenberg-Marquardt (LM), Scaled Conjugate Gradient (SCG) and Bayesian Regularization (BR), were used. The success of the ANN was measured using mean square error (MSE) and regression coefficient (R^2). These performance criteria were given in Equations 19 and 20, respectively.

$$MSE = \frac{\sum_{i=1}^{n} \left(y_{p,i} - y_i\right)^2}{n} \tag{19}$$

$$R^2 = 1 - \frac{\sum_{i=1}^{n} \left(y_{p,i} - y_i\right)^2}{\sum_{i=1}^{n} \left(y_{m,1}\right)^2} \tag{20}$$

where n is the sampling size, y_p is the estimated value, y_m is the measured value, and y_i is the value of the sampled data. The best results were obtained using the Levenberg-Marquardt algorithm. It was determined that MSE =3.46425e-7 and R^2 = 0.99962. Simulation studies conducted using the proposed ANN structure are given in Section 5.

5. The Proposed ANN-Based MPPT Algorithm and Its MATLAB/Simulink Simulation

When studies in the literature were examined, it is seen that either current and voltage values or temperature and radiation values has been used as input in ANN-based MPPT algorithms. In some studies, on the other hand, power values have also been added to the ANN input. In this study, the ANN structure was created with different input values. As ANN inputs, temperature and voltage information were used. The output of the ANN is the reference voltage to be controlled. PV panel voltage is controlled through the PI controller by using this reference voltage. Thus, the ripple in the power of the PV panel occurs barely.

The proposed method revealed an impressive performance under variable atmospheric conditions in which both temperature and radiation values were changing rapidly and slowly. Because the voltage reference generated by the ANN structure provides adaptation to variable atmospheric conditions, this proposed method is also an adaptive method. The current of the panel was not measured in this study. In this way, an advantage was ensured in terms of the number of sensors compared to many studies. The MATLAB/Simulink block diagram in which the proposed method is used is given in Figure 6. The sampling time was selected as 5µs. The switching frequency of the boost-type DC-DC converter was taken as 20 kHz. ANN algorithms require large computation times for microprocessors. Therefore, the sampling frequency of the MPPT algorithm was determined as 1 ms in this study.

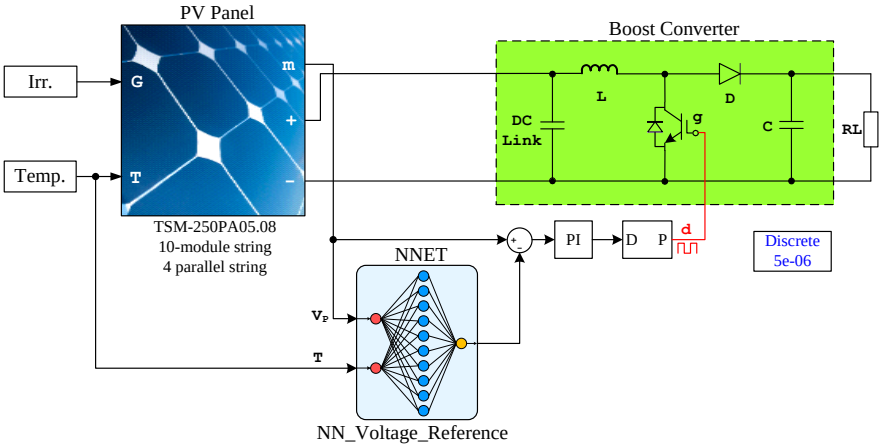

Figure 6. MATLAB/Simulink block diagram of the proposed ANN-based MPPT.

By creating a scenario in which radiation and temperature varied with different steps in different regions, IC, PO, and the proposed ANN-based method were compared. All three methods were tested under the same conditions in the comparison process. The temperature and radiation change scenario created for testing PO, IC, and the proposed method is seen in Figure 7.

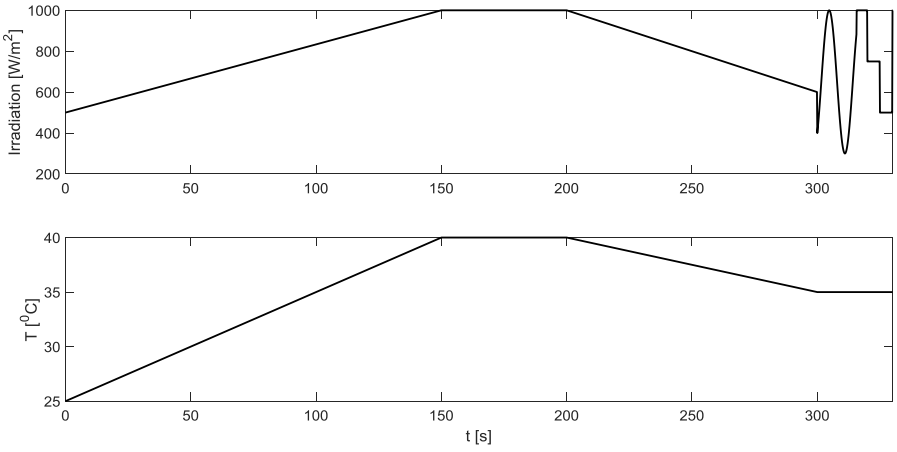

Figure 7. Radiation and temperature change scenario.

Figure 8 shows PV panel currents obtained by all three methods. Here, it is seen that there is no any ripple in the current waveform obtained by the proposed method.

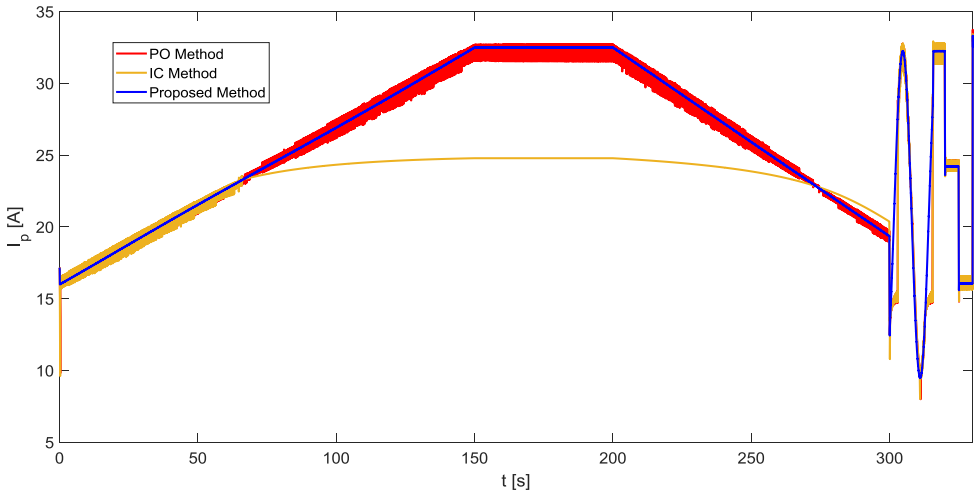

Figure 8. PV panel currents obtained for PO, IC and proposed ANN-based methods.

Figure 9 shows the obtained PV panel powers related to PO, IC and the proposed ANN-based method. Here, examinations were done in three different regions. In the first region, the steady-state was reached as earliest by the proposed method. In the second region, the IC method failed to track the maximum power point. In the PO method, the power ripple was quite high. In the ANN-based MPPT method, on the other hand, there was no power ripple. In the third region, whereas IC and PO were unable to track the maximum power point, the proposed method was successful. In the fourth region, the power ripple in the proposed ANN-based method was almost nonexistent compared to other PO and IC methods. In Figure 10, PV panel voltages obtained using each of the three methods are seen. Here, it is observed that the voltage obtained by the proposed method varies according to atmospheric conditions.

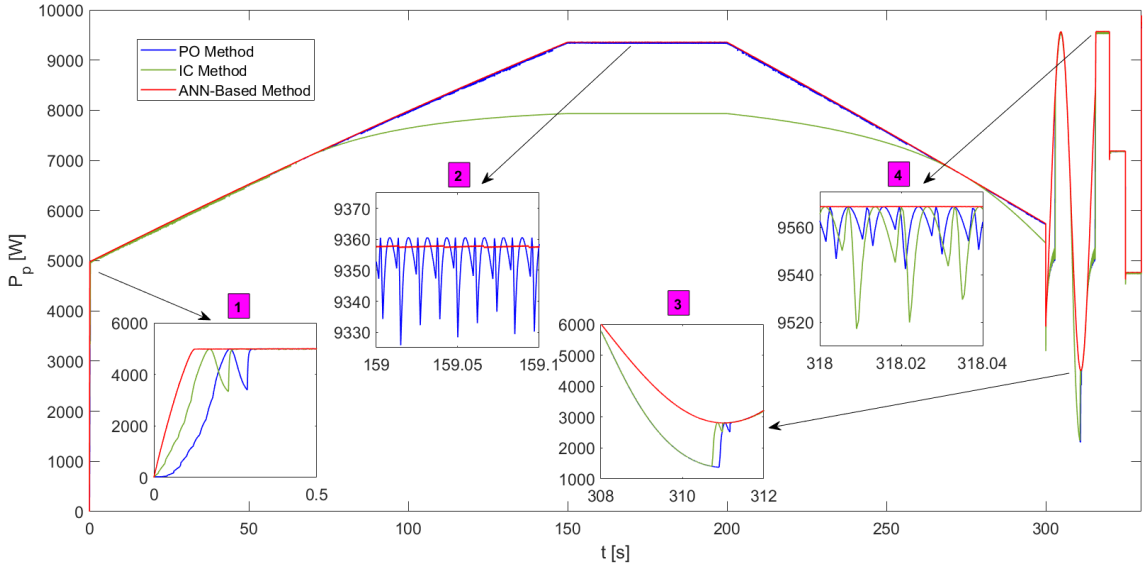

Figure 9. The obtained PV panel powers related to the PO, IC, and the proposed ANN-based methods.

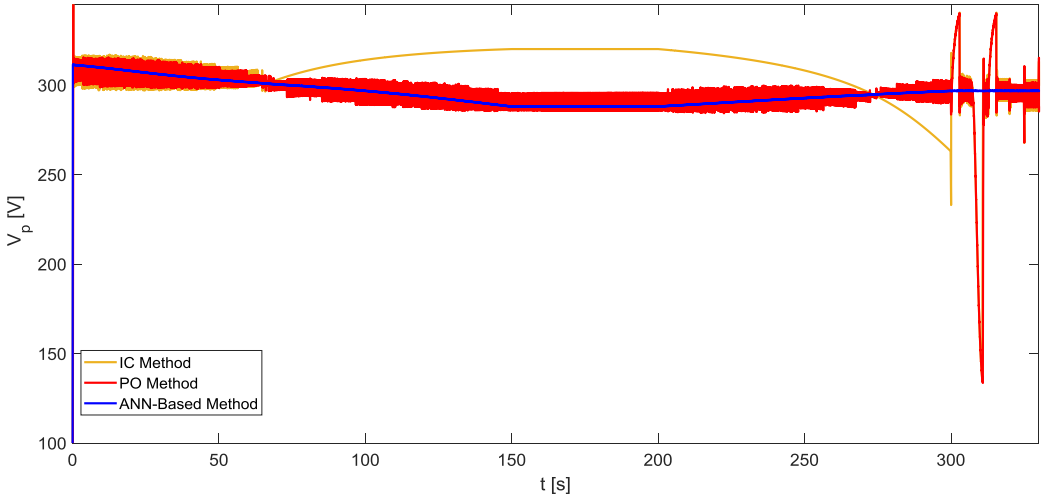

Figure 10. Obtained PV panel voltages related to the PO, IC, and proposed ANN-based methods.

6. Conclusion

It is quite important that MPPT algorithms operating under variable atmospheric conditions track the maximum power point. In addition to this, ripples that may occur in the PV power system are demanded to be low. Thus, the efficiency of the system is increased. There are many MPPT algorithms developed for this purpose. Conventional ANN methods are carried out by measuring either current and voltage or radiation and temperature values. In this study, an ANN-based MPPT method in which temperature and voltage data were used as input was proposed. In this proposed method, the output of the ANN structure constitutes the reference voltage, and this voltage is controlled by a PI controller. The performance of this ANN-based MPPT algorithm where temperature and voltage were used as inputs and which could operate under variable atmospheric conditions was discussed by comparing it to conventional PO and IC methods. In simulation studies, MPPT methods were tested using a scenario in which radiation and temperature values vary to create compelling conditions. In the proposed ANN-based method, the efficiency is highest as the amount of power ripple is minimum. It was seen that the proposed method was superior to the conventional methods in terms of both the fact that it could track the maximum power point in many different regions and the fact that the ripples in power were low.

References

[1] Larbes C, Cheikh SMA, Obeidi T, Zerguerras A. Genetic algorithms optimized fuzzy logic control for the maximum power point tracking in photovoltaic system. Renewable Energy 2009; 34: 2093–2100.

[2] Esram T, Chapman PL Comparison of photovoltaic array maximum power point tracking techniques. IEEE Transactions on Energy Conversion 2007; 22 (2): 439-449.

[3] Gupta A, Chauhan Y.K, Pachauri K. A comparative investigation of maximum power point tracking methods for solar PV systems. Solar Energy 2016; 136: 236-253.

[4] Belkaid A, Colak I, Kayisli K. Implementation of a modified P&O-MPPT algorithm adapted for varying solar radiation conditions. Electr Eng. 2017; 839–846.

[5] Chen PC, Chen PY, Liu YH, Chen JH, Luo YF. A comparative study on maximum power poit tracking techniques for photovoltaic generation systems operation under fast changing environments. Solar Energy 2015; 119: 261-276.

[6] Rezk H, Eltamaly AM. A comprehensive comparison of different MPPT techniques for photovoltaic systems. Solar Energy 2015; 112: 1-11.

[7] Ahmed J, Salam Z. An enhanced adaptive P&O MPPT for fast and efficient tracking under varying environmental conditions. IEEE Transactions on Sustainable Energy 2018; 9 (3): 1487-1496.

[8] Başoğlu ME, Çakır B. An improved incremental conductance based MPPT approach for PV modules. Turk J Elec Eng & Comp Sci. 2015; 23: 1687-1697.

[9] Radjai T, Rahmani L, Mekhilef S, Gaubert JP. Implementation of a modified incremental conductance MPPT algorithm with direct control based on a fuzzy duty cycle change estimator using dSPACE. Solar Energy 2014; 110: 325-337.

[10] Bataineh K. Improved hybrid algorithms-based MPPT algorithm for PV system operating under severe weather conditions. IET Power Electronics 2018; 12 (4): 703-711.

[11] Celikel R, Gundogdu A. System identification-based MPPT algorithm for PV systems under variable atmosphere

conditions using current sensorless approach. Int Trans Electr Energ Syst. 2020; e12433. https://doi.org/10.1002/2050-7038.12433.
[12] Celikel R. Speed Control of BLDC Using NARMA-L2 Controller in Single Link Manipulator. Balkan Journal of Electrical and Computer Engineering 2019; 7(2): 143-148.
[13] Karakaya B, Kaya T, Gulten A. FPGA-based ANN Design for Detecting Epileptic Seizure in EEG Signal. Balkan Journal of Electrical and Computer Engineering 2018; 6(2): 83-87.
[14] Deniz E. ANN-based MPPT algorithm for solar PMSM drive system fed by direct-connected PV array. Neural Comput & Applic. 2017; 28: 3061–3072.
[15] Elobaid LM, Abdelsalam AK, Zakzouk EE. Artificial neural network-based photovoltaic maximum power point tracking techniques: a survey. IET Renewable Power Generation 2015; 9(8): 1043-1063.
[16] Kermadi Mostefa, Berkouk EM. Artificial intelligence-based maximum power point tracking controllers for Photovoltaic systems: Comparative study. Renewable and Sustainable Energy Reviews 2017; 69: 369-386.
[17] Messalti S, Harrag A, Loukriz A. A new variable step size neural networks MPPT controller: Review, simulation and hardware implementation. Renewable and Sustainable Energy Reviews 2017; 68: 221-233.
[18] Çelik Ö, Teke A. A Hybrid MPPT method for grid connected photovoltaic systems under rapidly changing atmospheric conditions. Electric Power Systems Research 2017; 152: 194-210.
[19] Jyothy LP, Sindhu M.R. An Artificial Neural Network based MPPT Algorithm For Solar PV System. In 2018 4th International Conference on Electrical Energy Systems (ICEES) 2018; 375-380.
[20] Kota VR, Bhukya M.N. A novel global MPP tracking scheme based on shading pattern identification using artificial neural networks for photovoltaic power generation during partial shaded condition. IET Renewable Power Generation 2019; 13(10): 1647-1659.
[21] Ibrahim AW, Jin X, Dai X, Sarhan MA, Shafik MB, Zhou H. Artificial Neural Network Based Maximum Power Point Tracking for PV System. In 2019 Chinese Control Conference (CCC) 2019; 6559-6564.
[22] Aydogmus O. Design of a solar motor drive system fed by a direct-connected photovoltaic array. Advances in Electrical and Computer Engineering 2012; 12 (3): 53-58.

Turkish Journal of Science & Technology
15(2), 111-125, 2020

Performance Analysis of Open Loop V/f Control Technique for Six-Phase Induction Motor Fed By A Multiphase Inverter

Ahmet GÜNDOĞDU[1*], Reşat ÇELİKEL[2]
[1] Department of Electrical and Electronics Engineering, Faculty of Engineering, Batman University, Batman, Turkey
[*1] ahmet.gundogdu@gmail.com, [2] resat.celikel@batman.edu.tr

(Geliş/Received: 07/05/2020; Kabul/Accepted: 22/08/2020)

Abstract: Due to its advantages such as high power density and low torque ripple, the multi-phase induction motors are preferred in high power industrial applications requiring wind turbines, in marine propulsion systems, and particularly in electric vehicles. Control of n-phase induction motor drive systems with nonlinear structure is performed scalar or vectorially. The scalar control technique, also called Volt/Hertz (V/f), has a simple mathematical model. For low-performance industrial applications, its applicability is easy and its cost is low. In terms of the microprocessor, it requires less operational load density. It is resistant against motor parameter changes. In this study, the open-loop speed control of a 6-phase induction motor with asymmetric winding structure was performed using the V/f control technique. The mathematical model of the 6-phase induction motor and the power circuit model of the 6-phase inverter were created in MATLAB/Simulink environment. Using the space vector pulse width modulation (SVPWM) technique, the stator voltage and stator frequency were controlled. In reference speed and load changes, transient and steady state performance analysis of the drive system was carried out. The obtained simulation results showed that the 6-phase induction motor could be successfully controlled by the V/f control technique.

Key words: Multiphase Motor, Six-Phase Motor, Multiphase Inverter, V/f Control, Space Vector PWM.

Çok Fazlı İnverterden Beslenen Altı Fazlı İndüksiyon Motorun Açık Çevrim V/f Kontrol Tekniğinin Performans Analizi

Öz: Çok fazlı indüksiyon motorlar yüksek güç yoğunluğu ve düşük moment dalgalanması gibi avantajlarından dolayı yüksek güç gerektiren endüstriyel uygulamalar ile rüzgâr türbinleri, gemi tahrik sistemleri ve özellikle de elektrikli araçlarda tercih edilmektedir. Doğrusal olmayan yapıya sahip n-fazlı indüksiyon motor sürücü sistemlerinin denetimi skaler veya vektörel olarak gerçekleştirilir. Volt/Hertz (V/f) olarak ta adlandırılan skaler kontrol tekniği basit bir matematiksel modele sahiptir. Düşük performanslı endüstriyel uygulamalar için uygulanabilirliği kolay ve maliyeti düşüktür. Mikroişlemci açısından daha az işlemsel yük yoğunluğu gerektirir. Motor parametre değişimlerine karşı dayanıklıdır. Bu çalışmada V/f kontrol tekniği kullanılarak asimetrik sargı yapısına sahip 6-fazlı bir indüksiyon motorun açık çevrim hız denetimi gerçekleştirilmiştir. 6-fazlı indüksiyon motorun matematiksel modeli ile 6-fazlı inverterin güç devresi modeli MATLAB/Simulink ortamında oluşturulmuştur. Uzay vektör darbe genişlik modülasyon tekniği (UVDGM) kullanılarak, stator gerilimi ve stator frekansı kontrol edilmiştir. Referans hız ve yük değişimlerinde, sürücü sistemin geçici ve sürekli durum performans analizi yapılmıştır. Elde edilen benzetim sonuçlarından 6-fazlı indüksiyon motorun, V/f kontrol tekniği ile başarılı bir şekilde kontrol edilebildiği gösterilmiştir.

Anahtar kelimeler: Çok Fazlı Motor, 6-Fazlı Motor, Çok Fazlı İnverter, V/f Kontrol, Uzay Vektör PWM.

1. Introduction

Alternating Current (AC) drives, developed to control induction motors commonly used in industrial applications, ensure the control of the speed, torque or rotor position of the motor at specified operating ranges. This control is generally performed vectorially or scalar. Induction motors have a complex structure whose parameters vary over time because of its mathematical model, and that contains nonlinear and high-order differential equations. Since there is no 90° phase difference between the components that make up the torque and the flux, they are not independent of each other and there is a clamping effect between them. The motor model has been developed as a result of the analytical analyses. With the development of the motor model, which would eliminate this clamping effect, the first study on vector-controlled AC drives was conducted by German engineer Blaschke in 1971 [1]. High-performance drives using Field Oriented Control (FOC) and Direct Torque Control (DTC) methods, known as *vector control* methods, are used successfully in the industrial field. The advantages and disadvantages of these methods, whose application schemes are different but purposes are

* Corresponding author: ahmet.gundogdu@gmail.com. ORCID Number of authors: [1] 0000-0002-8333-3083, [2] 0000-0002-9169-6466

the same, have been revealed by comparing from different angles [2]. The main purpose of both methods is to control the torque and flux of the motor independently of each other and without being affected too much by parameter changes.

In the control implementations performed with fixed-parameter controllers that are commonly used for this purpose, an accurate mathematical model of the drive system, which is being controlled, is required. The vector control method has high dynamic performance but is sensitive to changes in machine parameters. Determination of the amplitude and position of the flux vector in an accurate way plays an important role in the control process [3, 4]. In the *scalar control* method, on the other hand, the torque and flux cannot be controlled independently due to the magnetic coupling between the torque and flux components of the motor [5]. In the scalar control method, which has relatively lower performance, the controlled variables are only the stator voltage and frequency. Therefore, torque and flux are a function of these two variables and there is a magnetic coupling between them. This coupling effect causes the transient state performance of the motor to slow down and deteriorate. Oscillations occur in the torque. By keeping the ratio of the voltage and frequency (V/f) applied to the stator constant, the air-gap flux is kept constant and it is tried to ensure that the motor produces constant torque at all speed ranges [2].

However, at low speeds, since a significant portion of the source voltage falls on the stator resistance, the air-gap flux decreases despite the fact that the V/f ratio is constant. Because the stator voltage cannot be increased in the speed zone above the rated speed (i.e., in the field attenuation zone), the air-gap flux must be reduced. In both cases where field attenuation occurs, the motor moves out of the constant torque zone and continues to operate in the constant power zone, and thus the torque constancy of the motor is impaired. For this reason, scalar control method is not preferred in servo applications that require precise position control. However, this method is widely used in industrial applications that do not require high performance because it is easy to implement and cost effective [6,7]. It is resistant to changes in machine parameters. The scalar control method is performed as both open-loop and closed-loop. The open-loop V/f control method has poor dynamic performance and is low cost. However, changes in load torque result in a high-amplitude steady-state error at motor speed, and oscillations occur in the torque in the transient state. In applications requiring a fast dynamic response and more precise speed control, open-loop is insufficient and closed-loop V/f control method is preferred.

2. Multiphase Motors

Due to their advantages such as high torque density and low torque ripple, multi-phase induction motors are preferred in high-power industrial applications, wind turbines, marine propulsion system, and electric vehicles [8]. Multiphase machines have led the concept of the multiphase drive system to emerge. Although the concept of multiphase drive system entered the literature in the middle of the 20nd century, two studies that could be considered fundamental in this field were published at the beginning of this century. The first of these studies is related to the control of the 6-phase induction motor with asymmetric double winding structure [9]. The second, on the other hand, is the study in which a detailed literature review of multi-phase electrical machines used in variable speed applications is given [10]. When multi-phase machines are compared with three-phase machines, it is seen that they have higher reliability, higher torque density, lower torque ripple [11]. In addition, as the total power is divided by the number of phases, the power requirement of the multiphase machine per phase is reduced; thus, the current-voltage levels of the semiconductor switching elements that provide this power decrease.

Besides these advantages that they have, obtaining and controlling of their mathematical model is more complex and difficult [12]. Despite their complex structure, with the development of the inverter technology and modulation algorithms, control of multiphase electrical machines can be carried out easily via advanced control techniques. Despite the advantages and disadvantages mentioned above, it is seen clearly through the conducted literature review that the usage areas of multi-phase electrical machines have become widespread. In the industry, the profusion of three-phase motion systems and drives is remarkable. It can be said that interest in multi-phase induction motors and multi-phase motor drives, used especially in high power applications, has increased in the last three decades [13]. Among multi-phase induction motors, 6-phase induction motors are more preferred. These motors are classified in the literature under three main headings: a) Dual three-phase, b) Symmetric six-phase, c) Asymmetric six-phase. All three motor types consist of two three-phase windings and the layout of these windings is shown in Figure 1.

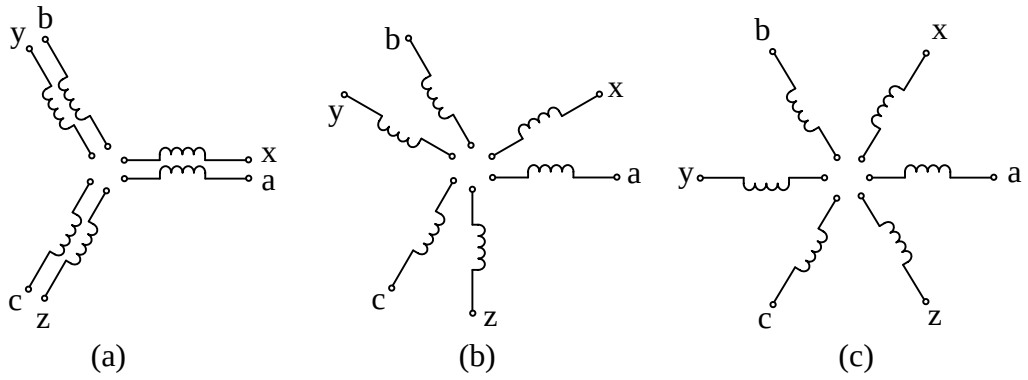

Figure 1. Winding layout of the 6-phase induction motor.
a) Dual three-phase ($\gamma = 0^0$), b) Asymmetric six-phase ($\gamma = 30^0$), c) Symmetric six-phase ($\gamma = 60^0$)

Some studies related to the control of 6-phase induction motors are given below. It was shown that the torque density of the motor was increased by adding the 3rd harmonic currents to the phase currents in the six-phase induction motor, and the results were supported by experimental studies [14]. An experimental study in which two separate three-phase inverters were used for indirect field-oriented control of six-phase induction motors was conducted [15]. Field-oriented vector control of six-phase induction motors consisting of two separate three-phase windings with an electrical angle of 30° between them was experimentally performed using six-phase inverters [16]. Rotor-field-oriented vector control of a six-phase induction motor with 10 kW power was performed experimentally [17]. Harmonic analysis of the windings of a 4-pole, 48-slot six-phase induction motor for open and short circuit states was performed both by simulation and experimentally and the results were compared [18]. Efficiency and performance analysis of high-frequency three-phase and six-phase induction motors used in medium and low power applications were performed. The results obtained by simulation and experimentation were given comparatively [19]. A new control algorithm that reduced torque ripples and motor losses in the motor in conditions where one or more of the motor phase windings were open-circuit was proposed. The validity of the proposed method was confirmed experimentally [20].

A new SVPWM technique was proposed to control a 15 kW six-phase induction motor, consisting of two separate three-phase windings, via a six-phase inverter. Though this proposed new technique was easy to implement digitally, it significantly reduced the harmonic current components of stator currents. The study was validated with experimental results [21]. Detailed mathematical models of two separate five-phase and six-phase motor drive systems were created for steady-state operation. The experimental results were given comparatively [22]. For current control of the six-phase induction motor with asymmetric winding structure, the model-based predictive control method was experimentally analyzed. Simulations were made to examine the performance of the control method. To determine the performance of the model-based predictive control method, the effect of the number of the considered voltage vectors was investigated and different cost functions were analyzed. The calculation time required to prove the real-time applicability of the control method was discussed [23]. By the field-oriented control method in which two separate controller structures (Fuzzy Controller-FC and sliding mode-SM controllers) were used, the vector control of the six-phase induction motor was performed experimentally. Analyses were made for the condition where three of the motor phase windings were open-circuit or disabled [24]. Direct torque control of the six-phase induction motor was performed without using a speed measurement sensor [25]. A new flux controller based on “adaptive gradient descent” was proposed to increase the efficiency of the six-phase induction motor controlled by the direct torque control method. It was validated by experimental studies that the proposed controller greatly increases efficiency by reducing iron losses and harmonic losses. This new controller structure is easy to implement, adaptable, and also requires no additional hardware for practical applications [26].

An experimental study was conducted on different current control techniques in the six-phase induction motor drive system with asymmetric winding structure [27]. Sensorless control of the six-phase induction motor with asymmetric winding structure was performed using the “non-linear backstepping control” method. Speed and voltage sensors were not used in the control algorithm [28]. In another study, a compilation of the studies conducted until 2016 and 2018 was given respectively [29, 30]. A “Circuit-Oriented Method” based motor model was developed to simulate possible failure conditions on the stator and rotor sides. The performance of

the model was observed both by simulation and experimentally using a 90-w, 14-V, 50-Hz, bipolar six-phase induction motor. Results were given comparatively [31]. The speed and torque control of the six-phase induction motor fed by a two-level six-phase inverter was experimentally performed using the direct torque control method. With the developed voltage-vector-selection algorithm, ripples in motor torque were reduced [32]. A detailed experimental analysis related to the failure conditions of six-phase induction motors with asymmetric, symmetrical and dual three-phase winding structures was conducted [33]. Blank operation and locked-rotor tests of the six-phase induction motor with an asymmetric winding structure were performed and motor parameters were estimated. To increase the accuracy of predicted parameters, a zero-sequence test method using an improved equivalent circuit was proposed. The proposed method was validated using experimental results [34].

For the creation of virtual voltage vectors used to reduce current harmonics, a simplified method was proposed. The proposed method was validated using experimental results [35]. A new prediction algorithm based on Model Reference Adaptive System-MRAS was proposed to predict and monitor stator resistance online. Direct torque control of the six-phase induction motor was performed experimentally by the proposed prediction algorithm [36]. For speed-sensorless direct torque control of a six-phase induction motor, a second-order sliding-mode MRAS-based flux observer was proposed. The performance of the proposed observer was validated by experimental results [37]. In six-phase induction motors, the effects of harmonics induced in the air-gap on the dynamic behavior of the motor were investigated. With the developed space harmonic model, analyses were made for both normal operation and fault states. The proposed model was experimentally performed using a 1.5 kW six-phase induction motor [38].

3. Mathematical Model of 6-Phase Induction Motor

The six-phase induction motor is a 6-dimensional system. Therefore, modeling and controlling of the motor in the original 6-phase reference plane is very difficult. In the general machine theory, mathematical transformations are used to facilitate the solution of differential equations whose coefficients vary over time and whose solution is difficult, and to reduce all variables to a common reference frame. If these transformations are used, the coupling effect between some variables is eliminated and a simplified model of the machine is obtained. To establish a dynamic model of these motors, the concepts of $\alpha\beta$ and dq conversion used in the derivation of the 2-phase equivalent circuit model of a 6-phase source-fed motor need to be known and properly laid out. In the 6-phase induction motor with asymmetric winding structure, two 3-phase windings are placed in the stator as shown in Figure 2 in a way that there is γ=30° electrical angle between them. The windings are star-connected and neutral points are insulated from each other [39].

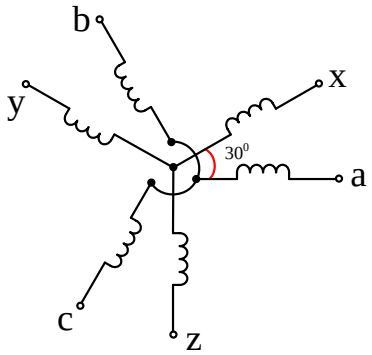

Figure 2. Asymmetric winding layout.

The mathematical model of these two winding groups, which are separated from each other by an electrical angle γ=0, in the $\alpha\beta$ axis set is given by the following equations. While modeling, it was assumed that stator windings were distributed as sinusoidal around air-gap, that air-gap flux showed a uniform distribution, that friction, ventilating losses and magnetic saturation were neglected, and that the windings were identical. If $p = d/dt$;

Voltage equations;

$$V_{s\alpha} = R_s I_{s\alpha} + p\lambda_{s\alpha} \quad (1)$$

$$V_{s\beta} = R_s I_{s\beta} + p\lambda_{s\beta} \quad (2)$$

$$V_{r\alpha} = R_r I_{r\alpha} + p\lambda_{r\alpha} + \omega_r \lambda_{r\beta} = 0 \quad (3)$$

$$V_{r\beta} = R_r I_{r\beta} + p\lambda_{r\beta} - \omega_r \lambda_{r\alpha} = 0 \quad (4)$$

where the notations of "s" and "*r*" refer to the stator and rotor variables, respectively. In addition, while the stator voltages are referred by $V_{s\alpha}$ and $V_{s\beta}$, $I_{s\alpha}$ and $I_{s\beta}$ refer to stator currents, $I_{r\alpha}$ and $I_{r\beta}$ refer to rotor currents. ω_r is rotor angular speed. R_s, R_r are stator and rotor winding resistances respectively.

Flux equations;

$$\lambda_{s\alpha} = \int (V_{s\alpha} - R_s I_{s\alpha})\, \mathrm{dt} \quad (5)$$

$$\lambda_{s\beta} = \int \left(V_{s\beta} - R_s I_{s\beta}\right) \mathrm{dt} \quad (6)$$

$$\lambda_{r\alpha} = \int \left(-R_r I_{r\alpha} - \omega_r \lambda_{r\beta}\right) \mathrm{dt} \quad (7)$$

$$\lambda_{r\beta} = \int \left(-R_r I_{r\beta} + \omega_r \lambda_{r\alpha}\right) \mathrm{dt} \quad (8)$$

Current equations;

$$I_{s\alpha} = (L_r \lambda_{s\alpha} - L_m \lambda_{r\alpha})/(L_s L_r - L_m L_m) \quad (9)$$

$$I_{s\beta} = \left(L_r \lambda_{s\beta} - L_m \lambda_{r\beta}\right)/(L_s L_r - L_m L_m) \quad (10)$$

$$I_{r\alpha} = (L_s \lambda_{r\alpha} - L_m \lambda_{s\alpha})/(L_s L_r - L_m L_m) \quad (11)$$

$$I_{r\alpha\beta} = \left(L_s \lambda_{r\beta} - L_m \lambda_{s\beta}\right)/(L_s L_r - L_m L_m) \quad (12)$$

where $\lambda_{s\alpha}$, $\lambda_{s\beta}$ are stator flux components, $\lambda_{r\alpha}$, $\lambda_{r\beta}$ are rotor flux components. L_s, L_r are stator and rotor inductances and L_m is mutual inductance.

Electromagnetic torque equation;

$$T_e = (3P/2) L_m \left[I_{s\beta} I_{r\alpha} - I_{s\alpha} I_{r\beta}\right] \quad (13)$$

The relationship between the mechanical speed of the motor and its electrical speed is expressed as in Equation 14 by taking into account the number of poles of the motor.

$$J \frac{2}{P} \frac{d\omega_r}{dt} = T_e - T_L - \frac{2}{P} B \omega_r \quad (14)$$

where J is the moment of inertia of the motor (kg.m^2) and B is the coefficient of friction that causes the moment of friction (Nm.s). The MATLAB/Simulink model in the $\alpha\beta$ axis set of the 6-phase induction motor with

asymmetric winding structure given above equations was formed as in Figure 3. The V/f control of the motor whose simulation model was formed described in detail in section 4.

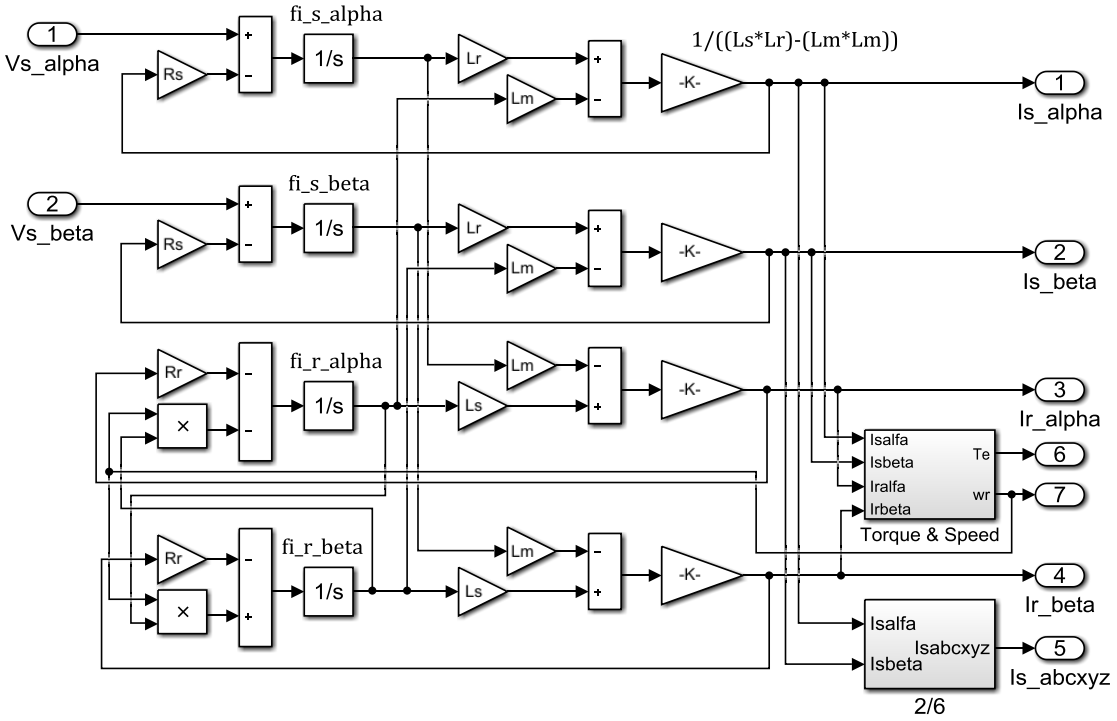

Figure 3. 6-phase induction motor's MATLAB/Simulink model in αβ axis.

4. V/f Control of 6-Phase Induction Motor

The speed and torque response of an induction motor controlled by the V/f scalar control method is low due to the clamping effect between the flux and torque components. As a result of analytical analysis on the motor model, this clamping effect is eliminated based on the development of the motor Model, which is represented by space vectors reduced to two axes, instead of n-number phase variables. Thus, the flux and torque of the motor can be controlled independently from each other. By eliminating the clamping effect, the speed and torque response of the motor is improved. With the development of this method, known as vector control, it has been understood that this low speed and torque response in the scalar control method is not due to the structure of the induction motor, but it is due to the form of the control applied to the motor [40,41].

The V/f control method is one of the methods used in the control of the variable-speed industrial drive systems. Its structure is simple and its cost is low. It can be performed as open and closed loop. The V/f method is a method based on the variation of the amplitude and frequency of the stator voltage of the motor. In induction motors, rotor speed is a function of the stator frequency. Therefore, in order to reach the desired rotor speed in the variable speed applications, the frequency of the stator voltage must be re-determined for each speed value. In order for the motor to produce constant torque at all speed values up to nominal speed, the motor's air-gap flux (λ_s) must be kept constant. However, by keeping the stator voltage constant, only changing the frequency of it distorts the stability of the air-gap flux. The generation of the torque in the motor depends on the formation of flux. The relationship between stator voltage and stator flux is given in Equation 15.

$$V_{s\alpha} = R_s I_s + p\lambda_s \tag{15}$$

The stator flux is defined as the integral of the back-emf voltage induced in the stator windings, and it is calculated as in Equation 16.

$$\lambda_s = \int (V_s - R_s I_s)\,\mathrm{dt} \tag{16}$$

If the ohmic voltage drop up to $R_s I_s$ on the stator winding resistance is ignored, then Equation 17 is obtained.

$$\lambda_s = \int V_s\,\mathrm{dt} \tag{17}$$

As can be seen in Equation 17, the stator flux vector λ_s is the integral of the applied V_s voltage and it is also directly related to the amplitude and frequency of that voltage. The impedance of the motor winding to which the V_s voltage is applied is $Z = \sqrt{R^2 + (X_L)^2}$. Here, $X_L = 2\pi f_S L$ is the inductive reactance of the winding and it is directly related to the frequency of the applied voltage f_s. In the V/f control method; 1) Changing only the f_s frequency by keeping the V_s winding voltage constant changes both the inductive reaction of the winding (X_L) and the total winding impedance (Z). Since the winding current I_s will change accordingly, the stator flux λ_s also changes. 2) If the f_s stator frequency is kept constant and only the f_s voltage is changed, again, the stator flux λ_s changes. Therefore, in order for the controlled motor to operate under constant torque at different speed values, the stator voltage and the stator frequency must be changed together. Because of this, in order to generate constant torque with constant λ_s flux in the motor, the voltage/frequency ratio must be kept constant. This ratio, known as the V/f ratio, is formulated with $k = V_s/f_s$.

As known, the T_e electromagnetic torque generated by the motor is as much as the ratio of the power of the motor to the mechanical speed of the motor and is expressed by Equation 18.

$$T_e = \frac{P_e}{\omega_m} \tag{18}$$

where ω_m is the mechanical speed of the motor. P_e is the power generated by the motor. Assuming that P is the number of poles, there is a relationship in the form $\omega_m = 2\omega_r/P$ between the mechanical speed of the motor and its electrical speed. Taking this relationship into account, a general diagram of the V/f method can be given as in Figure 4.

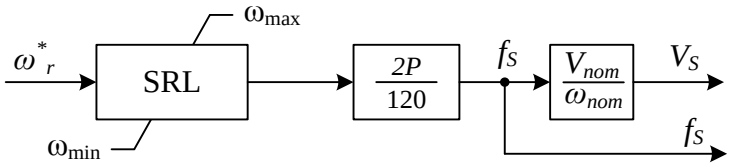

Figure 4. General principle diagram of V/f.

With the reference speed information at the block input shown in Figure 4, first the stator frequency f_s, then by multiplying this frequency value by the constant *k*, the stator voltage V_S corresponding to this frequency is calculated. The V_s and f_s obtained from the block output are the reference signals used to obtain the V_α and V_β voltages at the input of the SVPWM modulation algorithm that will drive the inverter, and these are recalculated for each reference speed value. Due to the clamping effect between the torque and flux components of the motor, the transient state performance of the V/f control technique is low. Against sudden reference speed changes, the motor cannot respond dynamically quickly enough. Therefore, in the transient state zone, the dynamic performance of the motor can be partially controlled using the slew rate limiter (SRL) block. The SRL block ensures delay only at sudden reference speed changes on a specific slope.

5. Space Vector Pulse Width Modulation (SVPWM)

In order for the V/f control of the 6-phase induction motor to be performed, the power supply feeding the motor must be a controlled-source whose voltage and frequency can be changed. In this study, the power circuit model of the 6-phase inverter used as a controlled power supply is given in Figure 5. In the control process, a 6-phase inverter with a single DC bus bar structure given in Figure 5 can be used, as well as two separate 3-phase

inverters can also be used. In high-power drive systems where 6-phase inverters with a single DC bus bar structure are used, the design of the DC bus bar is of particular importance.

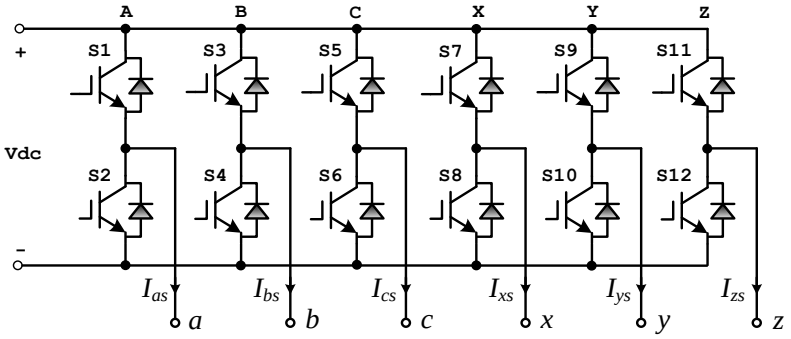

Figure 5. Power circuit model of the 6-phase inverter.

In Figure 5, the *abc* ends at the output of the inverter, which will feed the motor, feed the first 3-phase winding group of the motor, while the *xyz* ends feed the second 3-phase winding group. Between the current and voltages of these winding groups, which are placed separately with 30° electrical angles into the stator, there must also be 30° electrical angles. Therefore, for modulation of the inverter legs feeding each winding group, two separate SVPWM switching blocks whose input signals are separated 30° were used. The block diagram related to this is given in Figure 6.

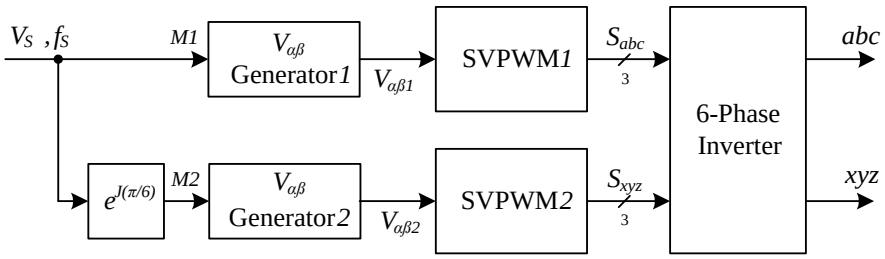

Figure 6. General principle diagram of V/f control of 6-phase induction motor.

6. V/f Drive System Model of 6-Phase Induction Motor

A general block diagram for the drive system is given in Figure 7. In the drive system performed as open loop, V_α and V_β input voltage values of the SVPWM algorithm were obtained from the reference speed input. The SVPWM1 block generates the triggering signals of switches on the ABC legs of the 6-phase inverter, while the SVPWM2 block generates the triggering signals of the switches on the XYZ legs. For both modulation algorithms, the switching frequency was chosen as $f_s = 5\ kHz$.

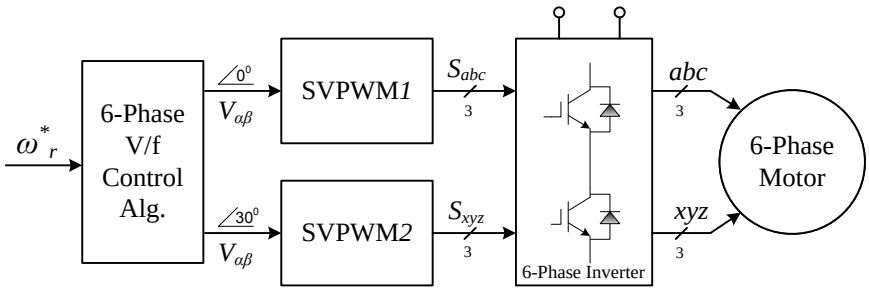

Figure 7. V/f drive system model of the 6-phase induction motor.

7. Simulation of V/f Speed Control of 6-Phase Induction Motor With MATLAB/Simulink

In this section, the open-loop V/f control of the 6-phase induction motor fed from the 6-phase inverter was simulated with MATLAB/Simulink. The simulation model for this is given in Figure 8.

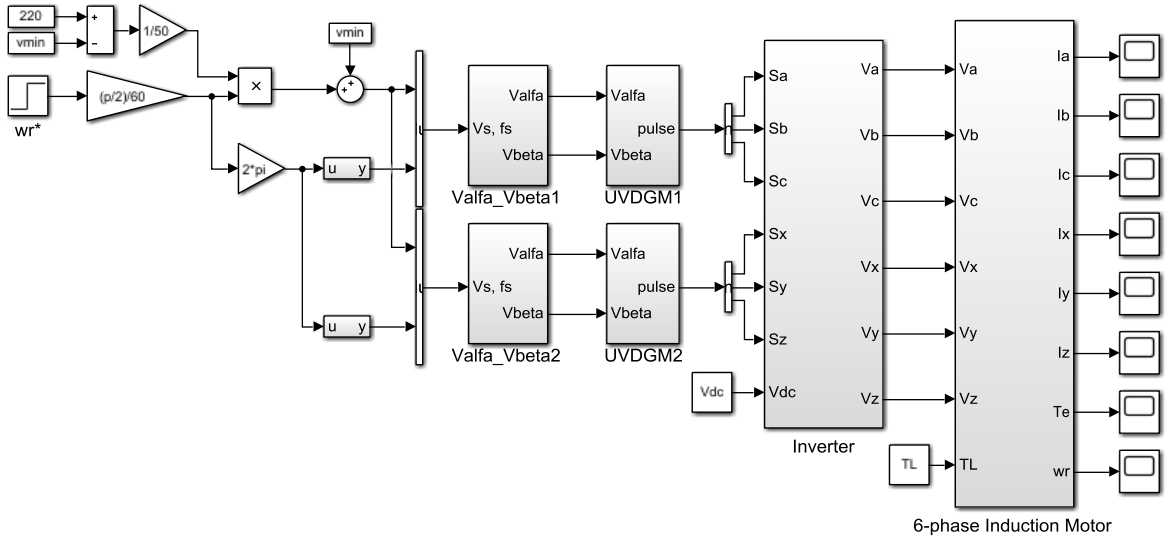

Figure 8. MATLAB/Simulink model of open-loop V/f control of 6-phase induction motor.

Within the Model, the V/f ratio was obtained first, and then the effective value of the V winding voltage required by the motor windings was determined by multiplying the obtained V/f ratio by the f frequency information generated from the reference speed information. The variation of M1 modulation signal in 0° plane and M2 modulation signals in 30° plane obtained by using this voltage and frequency information, which should be applied to Stator windings, is given in Figure 9.

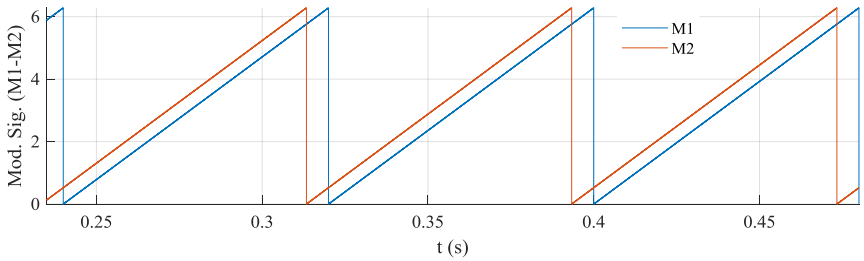

Figure 9. Change of M1-M2 modulation signals.

At low reference speed values, the frequency and voltage values generated by the algorithm will be low due to the constant V/f ratio. At low stator voltages, the motor will not be able to generate sufficient startup torque since a large part of the source voltage will fall as $R_s I_s$ on the stator winding. Therefore, in low-speed zones, the minimum boost voltage must be applied to the motor windings in order for the motor to generate sufficient startup torque.

8. Simulation Results

The simulation results obtained for different speed and load values by using the simulation model in Figure 8 are given with the following graphs. In Figure 10, for the reference speeds given as +750 rpm and +1500 rpm in the case of no-load operation, motor speed, motor torque, stator one phase winding current, and changes in the amplitude of the stator flux consisting of the components $\alpha\beta$ are given, respectively. In Figure 10a, the motor follows the given reference speeds properly. Within reference speeds capture times, the motor reaches the

steady-state by generating a torque worth of V/f ratio. In the reference speed changes, motor speed to reach the reference speed times are high due to the open-loop control structure and its transient state performance is low. This is a natural result of the open-loop V/f control algorithm. For further improvement of the transient state performance, closed-loop V/f control technique may be preferred. Thus, by processing the speed error between the reference speed and the actual speed taken from the motor shaft by a PI speed controller, it is ensured the motor to generate maximum torque. The fact that the motor generate maximum torque at reference speed changes further shortens the actual motor speed to reach reference speed (settling time), thus increases the motor's transient state performance.

In Figure 10b, it is seen that the motor generates high torque in the transient state to capture the given reference speeds and that in the steady state zone at constant speeds, the motor generates enough torque to meet the idle iron, friction and ventilating losses. As shown in Figure 10c, for the same reference speed values, the motor one phase winding current is higher in the transient state, and in the steady state, on the other hand, it is at the value that can generate the idle running torque of the motor. Since the V/f ratio is equal and constant at both reference speed values, the motor phase winding current has the same amplitude in both steady states except the transient state. Figure 10d shows the change in amplitude of the stator flux formed by $\alpha\beta$ flux components. Since the V/f ratio is equal and constant at both reference speed values, the stator flux is constant and has the same amplitude in both constant speed regions except the transient state. The fact that the stator flux has the same amplitude at different speed values means that the motor generates constant torque. For this reason, this region where the constant V/f ratio and the stator flux are kept constant from zero to nominal speed is called the *constant torque region*.

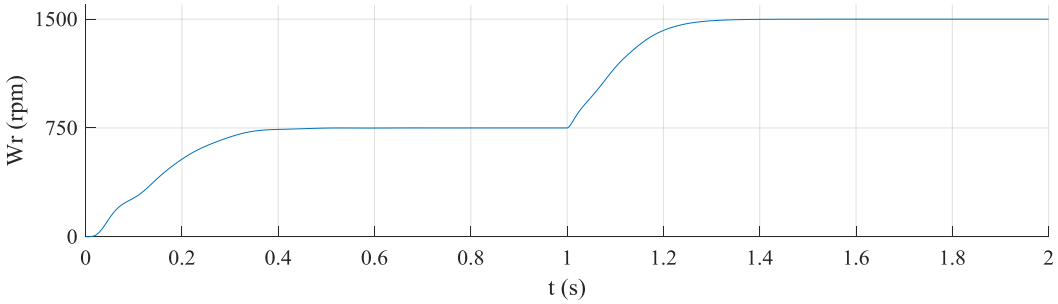

Figure 10a. Rotor speed at no-load operating state for +750 rpm to +1500 rpm.

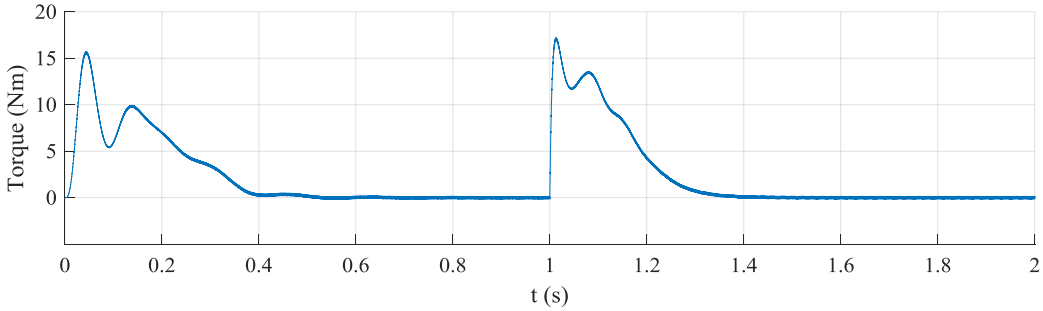

Figure 10b. Motor torque at no-load operating state for +750 rpm to +1500 rpm.

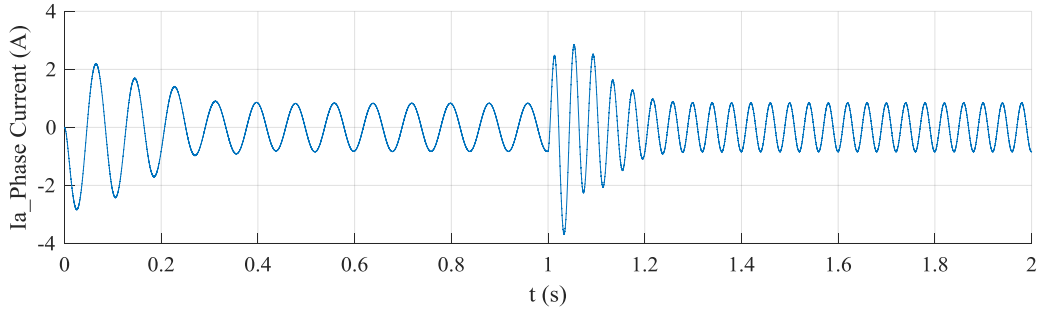

Figure 10c. Stator phase winding current at no-load operating state for +750 rpm to +1500 rpm.

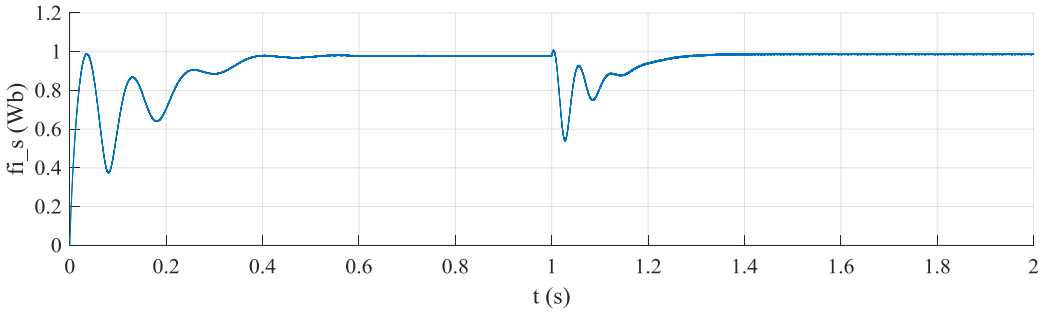

Figure 10d. Stator flux at no-load operating state for +750 rpm to +1500 rpm

Figure 11 presents stator currents at reference speeds given as +750 rpm and +1500 rpm in the case of no-load operation. Figure 11a shows stator currents at +750 rpm reference speed and Figure 11b shows stator currents at 1500 rpm reference speed. The 6-phase stator currents in both graphs are of the same amplitude; however, the frequency of stator currents obtained for the reference speed of +750 rpm is lower than the frequency of stator currents obtained at +1500 rpm speed.

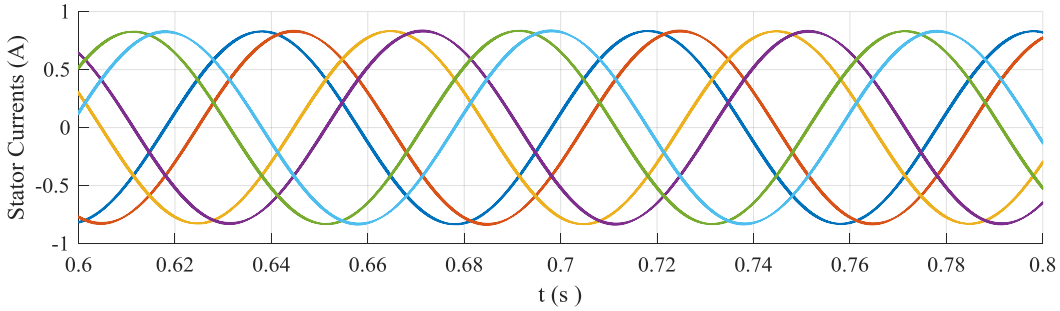

Figure 11a. Stator currents at no-load operating state for +750 rpm.

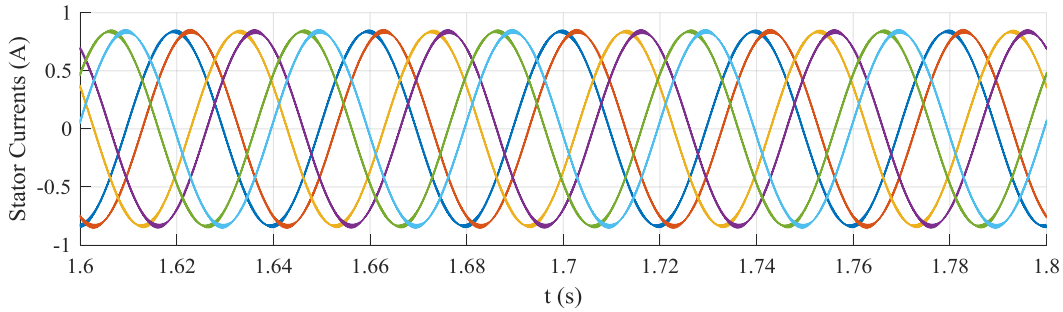

Figure 11b. Stator currents at no-load operating state for +1500 rpm.

In Figure 12-abcd, graphs for the on-load operating state at 1400 rpm are given. In the range of 0.8 to 1.2 sec, the motor was loaded with 4 Nm. In Figure 12a, a decrease in motor speed with loading was observed. The slip amount increased with loading and the motor continued to operate with steady-state speed error throughout the loading period. Steady-state speed error is one of the major disadvantages of open-loop control systems. In order for the decreasing motor speed to capture the reference speed again, the amount of slip must be compensated by the V/f algorithm. This compensation process is possible by feeding of the measured rotor speed back into the algorithm. The increased motor torque, motor currents and stator flux during the same loading period are shown in figures 12b,c,d, respectively.

As seen in Figure 12b, the motor generated a torque, which was in value that could meet the load imposed on its shaft during the loading period. Depending on the decreasing rotor speed and increased slip along with loading, the amplitude and frequency of the induced tension on the rotor increases. This causes the rotor flux λ_r to increase. As required by equation 9 and equation 10, the increased rotor flux also increases the stator currents. The increase of stator currents is shown in Figure 12c. On the other hand, as required by Equation 5 and

Equation 6, the increase of the stator current under constant V_s stator voltage causes the stator flux to decrease. This decrease in the stator flux is shown in Figure 12d.

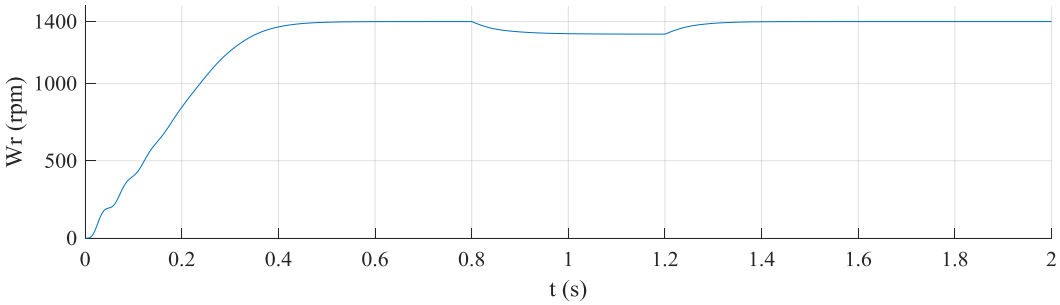

Figure 12a. Rotor speed at the loaded state.

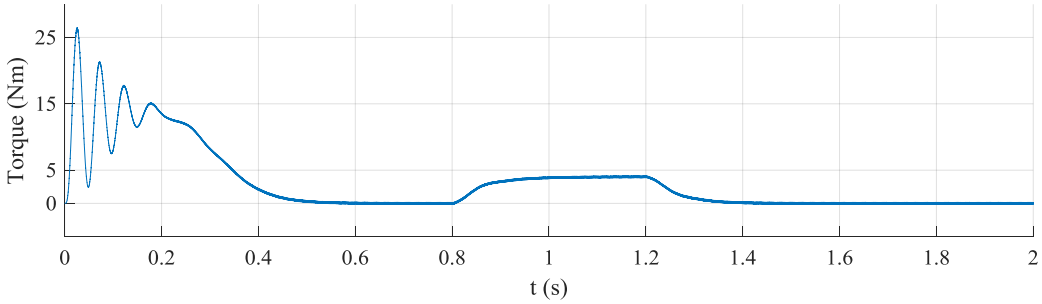

Figure 12b. Motor torque at the loaded state.

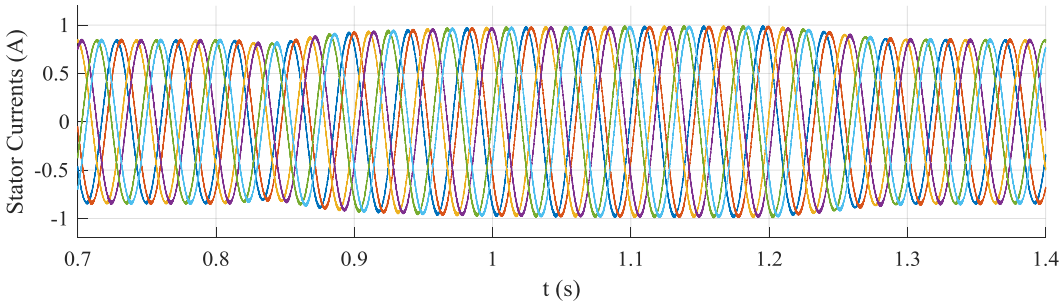

Figure 12c. Stator phase currents at the loaded state.

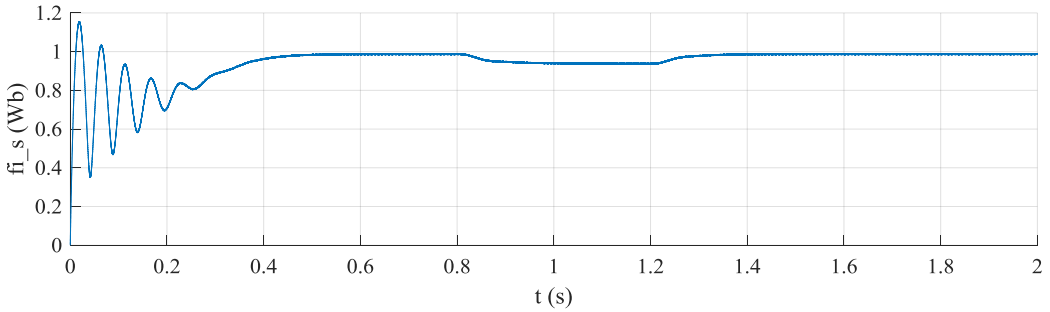

Figure 12d. Variation of the amplitude of the stator flux at the loaded state.

Figure 13-a,b,c,d show the speed, current, torque and flux graphs in the change of reference speed from +1500 rpm to -1500 rpm at the unloaded state. As can be seen from the graphs, in the region where the reference speed changes, the motor has generated maximum torque by drawing maximum current from the source. In Figure 13b, six-phase stator currents, and in Figure 13c, motor torque are shown. The decrease in stator flux within the time of settling on the reference speed in the negative direction is seen in Figure 13d.

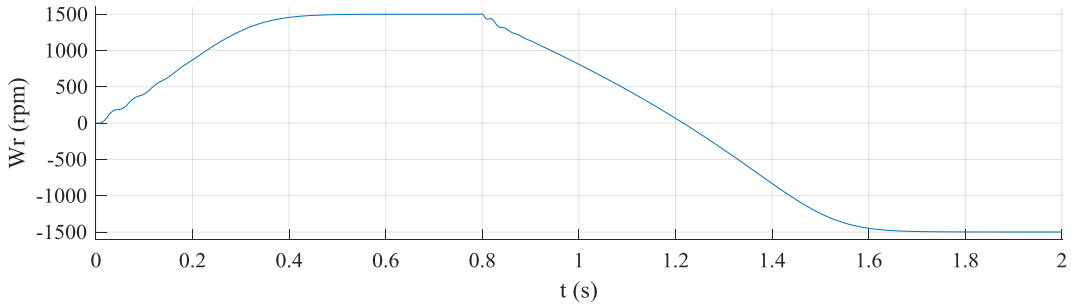

Figure 13a. Rotor speed.

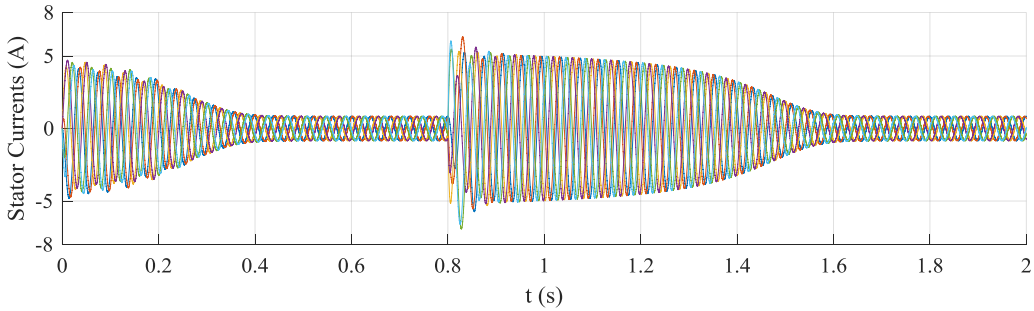

Figure 13b. 6-phase stator currents.

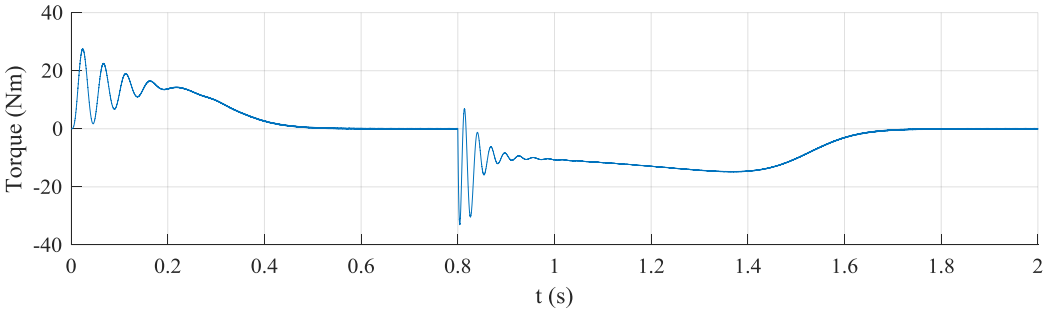

Figure 13c. Motor torque.

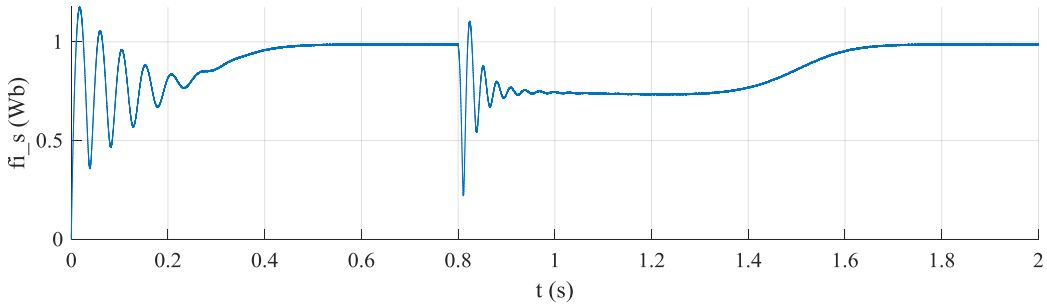

Figure 13d. Stator flux.

9. Conclusion

Due to its easy applicability and low cost, the open-loop V/f control method is preferred for low-performance industrial applications. In this study, open-loop speed control of a 6-phase induction motor with asymmetric winding structure was performed in MATLAB/Simulink environment by using the V/f control technique. A 6-phase induction motor was preferred because of its advantages such as high reliability, high torque density, and low torque ripple compared to 3-phase induction motors. With the conducted simulation studies, it was shown that the 6-phase induction motor could be successfully controlled by the V/f control technique.

Since the speed feedback is not used in the drive system realized as open-loop, the transient state performance of the motor is low in terms of the time to reach the reference speed. In addition, in the case of loaded operation, the steady-state speed error occurs in proportion to the magnitude of the load torque. This is a natural result of the open-loop V/f control technique and is not due to the structure of the motor. On the other hand, the motor's steady-state performance in the no-load and four-quadrant operation modes is high. In the drive systems where 6-phase induction motors are used, since the total power is divided by the number of phases, the current, voltage and power requirements per phase decrease. Therefore, drive circuit design can be realized with semiconductor switching elements with lower current and voltage capacity. It is thought that the 6-phase induction motor, controlled by advanced control methods, may be an alternative to the permanent magnet synchronous motors commonly used in electric vehicles.

Appendix A

Motor Parameters:

Rs=10.1 Ω; Rr=9.8546 Ω; Ls=0.8330 H; Lr=0.8330 H; Lm=0.7827 H; J=0.06 kg.m^2; B=0 Nm.s; P=4;

Rated Values:

Vphase=220 V, Vline=380 V, Vdc=537 V, Vboost= Vmin=30 V, P=550 W, T=4 Nm.

References

[1] Blaschke F. A New Method for the Structural Decoupling of AC Induction Machines. In Conf. Rec. IFAC, Dusseldorf, Germany 1971; 1-15.

[2] Hoang L.H. Comparison of Field-Oriented Control and Direct Torque Control for Induction Motor Drives. Thirty-Fourth IAS Annual Meeting. Conference Record of the 1999; IEEE Industry Applications Conference, 2: 1245-1252.

[3] Siddavatam R, Prakash R, Umanand L. Improving the Dynamic Response of Scalar Control of Induction Machine Drive using Phase Angle Control. IECON 2018-44th Annual Conference of the IEEE Industrial Electronics Society. 541-546.

[4] Gündoğdu A, Dandil B, Ata F. Direct Torque Control Based on Hysteresis Controller of Asynchronous Motor. Science and Engineering Journal of Fırat University 2017; 29(1): 197-205.

[5] Altay AS. Sensorless Vector Control Of a Three Phase-Inductıon Motor By Using a New MRAS Method. Phd.Thesis, İstanbul Technic University Institute of Science, İstanbul, (2014).

[6] Sen PC. Electric Motor Drives and Control Past Present, and Future", IEEE Transactions on Industrial Electronics 1990; 37(6): 562-575.

[7] Bose BK. Modern Power Electronics and AC Drivers, Prentice Hall, New Jersey, (2002).

[8] Levi E, Barrero F, Duran MJ. Multiphase Machines and Drives-Revisited. IEEE Transactions On Industrial Electronics 2016; 63(1): 429-432.

[9] Bojoi R, Farina F, Profumo F, Tenconi A. Dual-three phase induction machine drives control–a survey. IEEJ Transactions on Industry Applications 2006; 126(4): 420-429.

[10] Levi E. Multiphase electric machines for variable-speed applications. IEEE Transactions on Industrial Electronics 2008; 55(5): 1893-1909.

[11] Levi E, Bojoi R, Profumo F, Toliyat HA, Willianson S. Multiphase Induction Motor Drives-a Technology Status Review. IET Electr. Power Appl., 2007; 1(4): 489–516.

[12] Hou L, Su Y, Chen L. Dsp-Based Indirect Rotor Field Oriented Control for Multiphase Induction Machines. IEEE Int. Electric Machines and Drives Conference 2003; 976-980.

[13] Jones M, Vukosavic S, Levi E, Iqbal A. A Six-Phase Series- Connected Two-Motor Drive With Decoupled Dynamic Control. IEEE Transactions on Industry Applications 2005; 41(4): 1056-1066.

[14] Lyra ROC, Lipo TA. Torque Density Improvement in a Six-Phase Induction Motor With Third Harmonic Current Injection. IEEE Transactions On Industry Applications 2002; 38(5): 1351-1360.

[15] Singh GK, Nam K, Lim SK. A Simple Indirect Field-Oriented Control Scheme for Multiphase Induction Machine. IEEE Transactions On Industrial Electronics 2005; 52(4): 1177-1184.

[16] Mohapatra KK, Kanchan RS, Baiju MR, Tekwani PN, Gopakumar K. Independent Field-Oriented Control of Two Split-Phase Induction Motors From a Single Six-Phase Inverter. IEEE Transactions On Industrial Electronics 2005; 52(5): 1372-1382.

[17] Bojoi R, Levi E, Farina F, Tenconi A, Profumo F. Dual three-phase induction motor drive with digital current control in the stationary reference frame. IEE Proc.-Electr. Power Appl., 2006; 153(1): 129-139.

[18] Apsley J, Williamson S, Analysis of Multiphase Induction Machines With Winding Faults. IEEE Transactions On Industry Applications 2006; 42(2): 465-472.

[19] Boglietti A, Bojoi R, Cavagnino A, Tenconi A. Efficiency Analysis of PWM Inverter Fed Three-Phase and Dual Three-Phase High Frequency Induction Machines for Low/Medium Power Applications. IEEE Transactions On Industrial Electronics 2008; 55(5): 2015-2023.

[20] Kianinezhad R, Nahid-Mobarakeh B, Baghli L, Betin F, Capolino GA. Modeling and Control of Six-Phase Symmetrical Induction Machine Under Fault Condition Due to Open Phases. IEEE Transactions On Industrial Electronics 2008; 55(5): 1966-1977.
[21] Marouani K, Baghli L, Hadiouche D, Kheloui A, Rezzoug A. A New PWM Strategy Based on a 24-Sector Vector Space Decomposition for a Six-Phase VSI-Fed Dual Stator Induction Motor. IEEE Transactions On Industrial Electronics 2008; 55(5):1910-1920.
[22] Levi E, Jones M, Vukosavic SN, Toliyat HA. Steady-State Modeling of Series-Connected Five-Phase and Six-Phase Two-Motor Drives. IEEE Transactions On Industry Applications 2008; 44(5): 1559-1568.
[23] Barrero F, Arahal MR, Gregor R, Toral S, Duran MJ. A Proof of Concept Study of Predictive Current Control for VSI-Driven Asymmetrical Dual Three-Phase AC Machines. IEEE Transactions On Industrial Electronics 2009; 56(6): 1937-1954.
[24] Fnaiech MA, Betin F, Capolino GA, Fnaiech F. Fuzzy Logic and Sliding-Mode Controls Applied to Six-Phase Induction Machine With Open Phases. IEEE Transactions On Industrial Electronics 2010; 57(1): 354-364.
[25] Zaimeddine R, Undeland T. Direct Torque Control Scheme For Dual-Three-Phase Induction Motor. The 2010 International Power Electronics Conf., 2010; 3007-3014.
[26] Taher A, Rahmati A, Kaboli S. Efficiency Improvement in DTC of Six-Phase Induction Machine by Adaptive Gradient Descent of Flux. IEEE Transactions On Power Electronics 2012; 27(3): 1552-1562.
[27] Che HS, Levi E, Jones M, Hew WP, Rahim NA. Current Control Methods for an Asymmetrical Six-Phase Induction Motor Drive. IEEE Transactions On Power Electronics 2014; 29(1): 407-417.
[28] Seyed M, Fatemi JR, Abjadi NR, Soltani J, Abazari S. Speed sensorless control of a six-phase induction motor drive using backstepping control. IET Power Electronic 2013; 7(1): 114–123.
[29] Levi E, Barrero F, Duran MJ. Multiphase Machines and Drives-Revisited. IEEE Transactions On Industrial Electronics 2016; 63(1): 429-432.
[30] Liu Z, Li Y, Zheng Z. A Review of Drive Techniques for Multiphase Machines. Ces Transactions On Electrical Machines And Systems 2018; 2(2): 243-251.
[31] Pantea A, Yazidi A, Betin F, Taherzadeh M, Carriere S, Henao H, Capolino G.A. Six-Phase Induction Machine Model for Electrical Fault Simulation Using the Circuit-Oriented Method. IEEE Transactions On Industrial Electronics 2016; 63(1): 494-503.
[32] Pandit JK, Aware VA, Nemade RV, Levi E. Direct Torque Control Scheme for a Six-Phase Induction Motor With Reduced Torque Ripple. IEEE Transactions On Power Electronics 2017; 32(9): 7118-7129.
[33] Munim WNWA, Duran MJ, Che HS, Bermudez M, Ignacio GP, Rahim NA. A Unified Analysis of the Fault Tolerance Capability in Six-Phase Induction Motor Drives. IEEE Transactions On Power Electronics 2017; 32(10): 7824-7836.
[34] Che HS, Abdel-Khalik AS, Dordevi, O, Levi E. Parameter Estimation of Asymmetrical Six-Phase Induction Machines Using Modified Standard Tests. IEEE Transactions On Industrial Electronics 2017; 64(8): 6075-6085.
[35] Pandit JK, Awar, MV, Nemade R, Tatte,Y. Simplified Implementation of Synthetic Vectors for DTC of Asymmetric Six-Phase Induction Motor Drives. IEEE Transactions On Industry Applications 2018; 54(3): 2306-2318.
[36] Holakooie MH, Ojaghi M, Taheri A. Direct Torque Control of Six-Phase Induction Motor With a Novel MRAS-Based Stator Resistance Estimator. IEEE Transactions On Industrial Electronics 2018; 65(10): 7685-7696.
[37] Holakooie MH, Ojaghi M, Taheri A. Modified DTC of a Six-Phase Induction Motor With a Second-Order Sliding-Mode MRAS-Based Speed Estimator. IEEE Transactions On Power Electronics 2019; 34(1): 600-611.
[38] Abdel-Khalik AS, Hamdy RA, Massoud AM, Ahmed S. Low-Order Space Harmonic Modeling of Asymmetrical Six-Phase Induction Machines. IEEE Access 2019; 7: 6866-6876.
[39] Bojoi R, Lazzari M, Profumo F, Tenconi A, Digital Field-Oriented Control for Dual Three-Phase Induction Motor Drives. IEEE Transactions on Industry Applications 2003; 39(3): 752-760.
[40] Gündoğdu A., "Torque Ripple Reduction of Asynchronous Motor by Neural-Fuzzy Networks", Phd.Thesis, Firat University Institute of Science, Elazığ, Turkey, 2012.
[41] Uzun H, Akar O, Demirci A, Akuner MC, Terzi UK. Analyzing High Efficiency Asynchronous Motors Using Scalar Control Technique. Balkan Journal of Electrical & Computer Engineering 2018; 6: 23-26.

Turkish Journal of Science & Technology
15(2), 127-137, 2020

The Effect of Aggregate Size and Cure Conditions On The Engineering Properties of Concrete

Kenan Toklu[1*], Salih Yazıcıoğlu [2]
[1] İnşaat Mühendisliği Bölümü, Çorlu Mühendislik Fakültesi, Tekirdağ Namık Kemal Üniversitesi, Tekirdağ, Türkiye
[2] İnşaat Mühendisliği Bölümü, Teknoloji Fakültesi, Gazi Üniversitesi, Ankara, Türkiye
[*1] ktoklu@nku.edu.tr, [2] syazicioglu@gazi.edu.tr

(Geliş/Received: 07/04/2020; Kabul/Accepted: 22/08/2020)

Abstract: In this study, the effect of curing conditions and aggregate size on the engineering properties of concrete was investigated. Aggregates in the range of 0-8 mm and 0-16 mm were used in concrete production and then cubic samples of 100x100x100 mm were prepared. In the study, slump value of fresh concrete was determined as S3. Three samples were used for each experiment. Compressive strength, abrasion, porosity and carbonation tests were performed on 28-day concrete samples subjected to water and air curing. According to the results obtained, it is determined that concrete samples under the effect of water curing give better results. In addition, better results were obtained for compressive strength, abrasion, porosity and carbonation properties of concrete by increase in aggregate size. It has also been observed that there is an increase in compressive strength of concrete, a positively decrease for abrasion, porosity and carbonation properties.

Key words: Concrete, air cure, water cure, slump, aggregate size.

Agrega Boyutu ve Kür Şartlarının Betonun Mühendislik Özelliklerine Etkisi

Öz: Bu çalışmada, agrega boyutu ve kür şartlarının betonun mühendislik özelliklerine etkisi araştırılmıştır. Tane boyutu 8 ve 16 mm olan agregalar kullanılarak 100x100x100 mm' lik küp numuneler hazırlanmıştır. Çalışmada taze betonların slump değeri S3 olarak belirlenmiştir. Her bir deney için 3'er adet numune kullanılarak su ve hava kürüne tabi tutulan 28 günlük beton numuneleri üzerinde basınç dayanımı, aşınma, porozite ve karbonatlaşma deneyleri yapılmıştır. Elde edilen sonuçlara göre su kürü etkisindeki beton numunelerinin daha iyi sonuç verdiği belirlenmiştir. Ayrıca, agrega boyutunun artmasıyla betonun basınç dayanımında artış, aşınma, porozite ve karbonatlaşma özelliklerinde olumlu yönde azalma meydana geldiği görülmüştür.

Anahtar kelimeler: Beton, hava kürü, su kürü, slump, agrega boyutu.

1. Introduction

Although the first use date of concrete is not known precisely, the history of concrete technology goes back to about 1845. Concrete; It is a composite material that is produced by mixing fine aggregate, coarse aggregate, cement, water and mineral, chemical additives or fiber in certain proportions according to the requirement. In addition to, concrete is a composite material that initially has a plastic consistency that can take the desired shape and hardens as a result of the hydration of cement and water with the passing of time [1].

The concrete aggregate used in the production of concrete or mortar is a stack that is combined with the binding material formed by the hydration of cement and water to create concrete and broken or unbroken grains, naturally or artificially, whose maximum grain size does not exceed generally 100 mm [2].

The properties and performance of fresh or hardened concrete depends on the quality and proportion of the materials forming the concrete (water / cement, aggregate grain distribution, etc.). Some properties of high strength and economical concrete and aggregates used in the concrete production are directly related. Thanks to the appropriate aggregate, concretes with durability, strength and workability can be obtained [3].

The dimensional distribution of aggregates is determined by sieve analysis experiment. Aggregates are classified as fine-grained or coarse-grained aggregates according to the results of sieve analysis. Aggregates passing through 4 mm sieve are called fine aggregates, and aggregates with a diameter larger than 4 mm are called large aggregates. Aggregates have an important place in the materials that make up the concrete as they form carrier frame of the concrete. For a quality concrete, the grain distribution of aggregates in concrete mix design must be properly and in accordance with the standards. In this way, an economical and quality concrete can be produced by providing the maximum compaction of concrete. [4].

* Corresponding author: ktoklu@nku.edu.tr. ORCID Number of authors: [1] 0000-0003-1288-845X, [2] 0000-0002-6767-2026

Curing conditions of concrete are specified as the effects of humidity and temperature in the environment where the concrete is located. In order for the hydration reactions between cement and water to continue, there must be water in the environment where the concrete is located. If there is not enough water in the environment, hydration reactions either slow down or stop completely. As a consequence, concrete cannot gain strength [5,6]. Therefore, it is necessary to provide the curing conditions of the concrete in the best way to ensure the maximum level of hydration reactions [7].

In this study, the effects of different aggregate size and curing conditions on the engineering properties of concrete were investigated.

2. Material and Method

2.1. Material

2.1.1. Cement

CEM I 42.5 R type cement was used as cement in the study. Cement properties are shown in Table 1.

Table 1. Cement properties

Properties	SiO_2	Al_2O_3	Fe_2O_3	CaO	MgO	SO_3	K_2O	Ignition Loss (%)
Value (%)	18.69	5.34	3.27	63.70	1.54	2,70	0,75	3.57

2.1.2. Aggregate

In the study, crushed stone aggregates of 0-8 mm and 0-16 mm grain sizes were used for concrete production. Sieve analysis results of 0-8 mm and 0-16 mm aggregate groups are given in Figure 1 and Figure 2, and physical properties are given in Table 2.

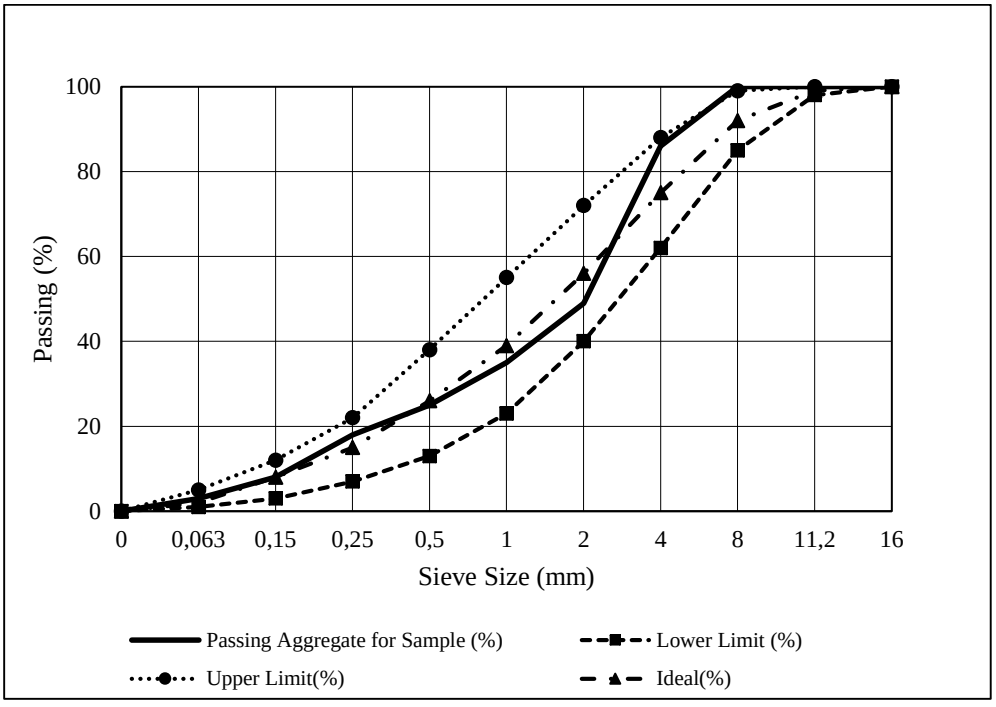

Figure 1. Limits of aggregate grain size distribution curve determined for concrete with the largest grain size of 8 mm aggregate and granulometry curve for 0-8 mm aggregate group

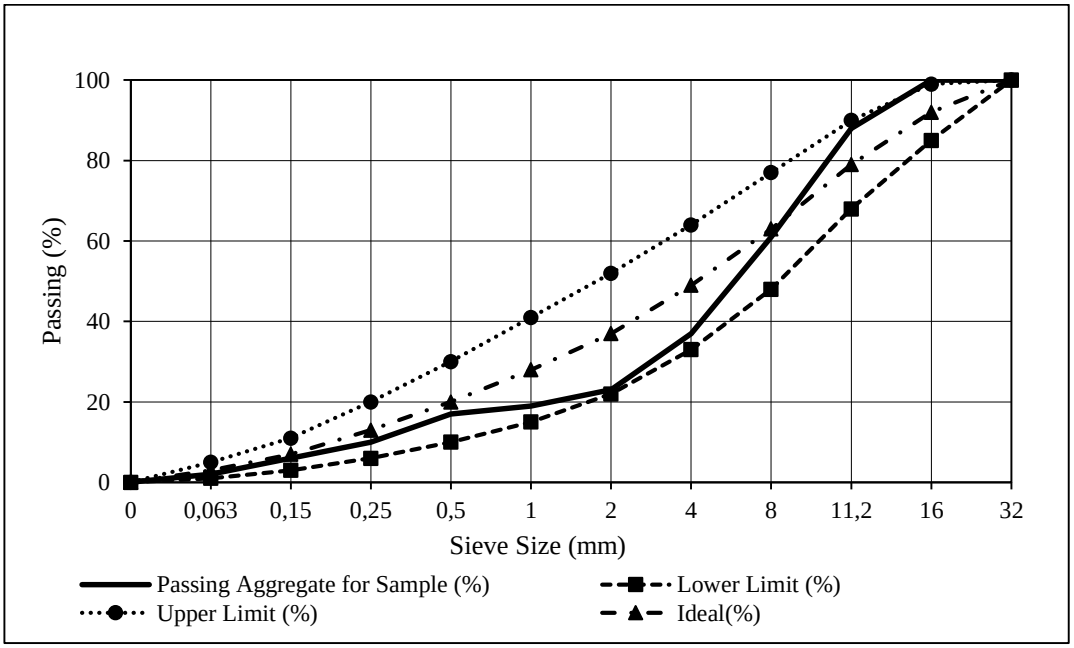

Figure 2. Limits of aggregate grain size distribution curve determined for concrete with the largest grain size of 16 mm aggregate and granulometry curve for 0-16 mm aggregate group

Table 2. Physical properties of aggregate

Physical properties of aggregate			
Aggregate Type	Water Absorption (%)	Specific Weight (gr/cm^3)	Abrasion Loss (%)
Crushed Stone (0-8 mm)	3.34	2.78	-
Crushed Stone (0-16 mm)	0.744	2.71	23.1

2.1.3. Mixing water

Tap water of Ankara was used as mixing water.

2.2. Method

2.2.1. Preparation of concrete samples

Aggregate used in concrete production is crushed stone aggregate. The aggregate used in the preparation of samples has a maximum grain size of 8 and 16 mm respectively. In the study, slump value was kept constant (6-9 cm) in all concrete series. The total amount of binders in all concrete series has been selected as 400 kg/m^3. Mix ratios of concrete samples prepared in this way are given in Table 3. In the study, 100x100x100 mm cube sample molds were used for compressive strength, abrasion, porosity and carbonation tests. Concrete mixes are prepared in the mixer and placed in the molds by considering the recommendations given in the standards (TS EN 12390-3 [8] and ASTM C944 / C944M [9]). After the prepared mixes were placed in the molds with 25 times rodding in 2 stages, the samples were removed from the molds after waiting 1 day under laboratory conditions. Then, half of the samples were kept in air curing and the other half of samples were kept in water curing for 28 days.

Table 3. Mixing ratios of the samples tested

Mixing ratios of Samples			
Aggregate Size (mm)	Water (kg/m^3)	Cement (kg/m^3)	Aggregate (kg/m^3)
0-8	238	400	1708
0-16	230	400	1716

2.2.2. Tests

Compressive Strength Test

For each group of concrete samples produced with a maximum aggregate size of 8 and 16 mm, a total of 12 samples of 100 mm cubes (3 samples both cured in air and water for each group) were subjected to compressive strength test on the 28^{th} day. Compressive strength tests were carried out in accordance with TS EN 12390-3-2010 [8]. The mold where samples are poured and samples are given in Picture 1. Samples subjected to water curing were kept at a temperature of 20 °C and all surfaces were left in water (Picture 2) and samples that were subjected to air curing (Picture 3) were cured by standing in a laboratory environment.

Picture 1. Molds where samples are poured and their appearance after pouring

Picture 2. Samples left on the water cure

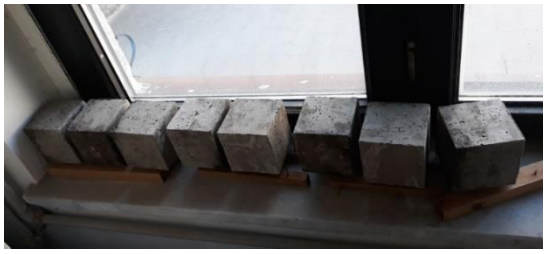

Picture 3. Samples left on air curing

Abrasion Test

12 samples in total including 6 samples for each group from 100 mm cubes produced with aggregates with 0-8 mm and 0-16 mm grain sizes were subjected to the abrasion test. Abrasion test was carried out in accordance with ASTM C944 / C944M [9]. Half of the samples were kept in air curing and the other half were kept in water curing for 28 days and then they were subjected to abrasion test. The samples, which have completed the curing period for the abrasion test, were subjected to abrasion for 6 minutes with abrasive wheels having a speed of 200 rpm. The abrasion test aparatus and samples after abrasion are given in Picture 4 and Picture 5.

Picture 4. Abrasion Test Aparatus

Picture 5. Samples after abrasion test

Porosity Test

For the determination of porosity, the dry weights of the samples were determined first and the value found was recorded as Wo. Samples with dry weights were kept in water during the period of 1 day so that all surfaces were kept in water to absorb water. Then all surfaces of the samples taken from the water were dried. After the samples were dried, they were weighed and the value found was recorded as W_1. Then, the weight of the samples under water was found by the Archimedes scale (Picture 6) and the value found was recorded as W_2. All the required values were calculated and replaced with the Equation 1 and porosity (P) value was found.

$$P = \frac{(W_1 - W_0)}{(W_1 - W_2)} * 100 \quad (1)$$

Picture 6. Archimedes scale

Carbonation Test

For each group of concrete samples produced with a maximum aggregate size of 8 and 16 mm, a total of 12 samples of 100 mm cubes (3 samples both cured in air and water for each group) were subjected to accelerated carbonation tests on the 28th day. The gas tightness of the accelerated test apparatus was first tested for carbonation test. After the samples were placed in the carbonation tank, 1 bar of CO_2 gas was given to the tank. Sodium dichromate was used to adjust the humidity inside the apparatus to approximately 55%. The appearance of the accelerated carbonation tank prepared is given in Picture 7. The concretes removed from the carbonation tank were subjected to the splitting tensile test [10] to be split in two pieces to samples, and the phenolphthalein solution was sprayed into the divided pieces and color change was observed in the sample. Fenolftalin which reacts with the hydration product, calcium hydroxide, creates a color that turns pink in the sample, and no color change occurs in the carbonation zone. The appearance of the phenolftaline sprayed sample is as in Figure 3, and the carbonation depth is measured by measuring the values A1, A2, B1, B2, C1, C2, D1, D2 and placing the values found in the Equation 2 below [11, 12]. Carbonation test samples are given in Picture 8.

Picture 7 Carbonation test apparatus

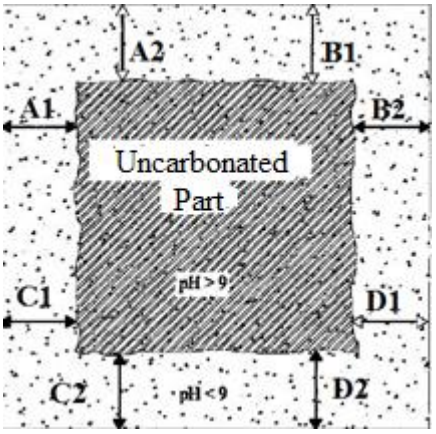

Figure 3. Sample for the carbonation test [11, 12].

$$\text{Carbonation Depth} = \frac{(A_1+A_2+B_1+B_2+C_1+C_2+D_1+D_2)}{8} * 100 \quad (2)$$

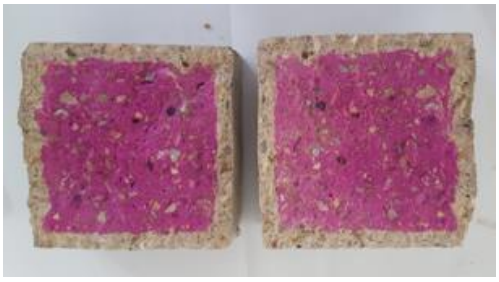

Picture 8. Fenolftalin sprayed samples

3. Findings

3.1. Compressive strength test

The results of the compressive strength test performed on the hardened concrete samples (28 days) are shown in Figure 4.

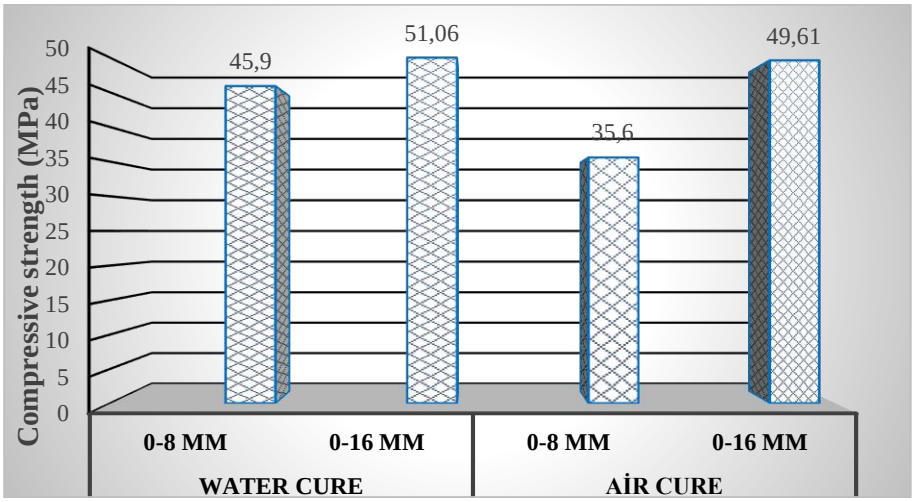

Figure 4. Results of compressive strength test on 28th day

When Figure 4 is analyzed, it is seen that compressive strength of concrete samples cured in water gives better results than the aired cured ones. In the samples produced with 0-8 mm aggregate group, it is seen that the compressive strength of the samples cured with water was 45.9 N/mm^2, the compressive strength of the samples cured with air was 35.6 N/mm^2. Concrete samples produced with 0-8 mm aggregate group cured with water gave approximately 29% more compressive strength than air curing. In the samples produced with 0-16 mm aggregate group, it was observed that those that were cured with water have a compressive strength of 51.06 N/mm^2, and those that were cured with air have a compressive strength of 49.61 N/mm^2. It has also been seen that concrete samples produced with 0-16 mm aggregate group cured with water give approximately 3% more compressive strength than air cured samples. Therefore, it has been observed that concrete samples cured with water give better results than concrete samples cured with air. When the results are examined in terms of aggregate size, increases in compressive strength have occurred with increasing aggregate size. The most important feature affecting compressive strength is the compactness of the sample. The amount of water in the mixture and the amount of void will increase as the aggregate size decreases. Therefore, the compaction and compressive strength of the sample is reduced. The compaction and compressive strength of the sample increases with increasing aggregate size [4].

3.2. Abrasion test

When Figure 5, which gives the results of the abrasion test of the concrete samples according to the curing conditions, was examined, it was seen that the abrasion resistance of the samples that were subjected to water curing gave better results similar to the results of the compressive strength. In addition, when the aggregate grain size is taken into consideration, it was observed that the abrasion percentage decreased with increasing aggregate size.

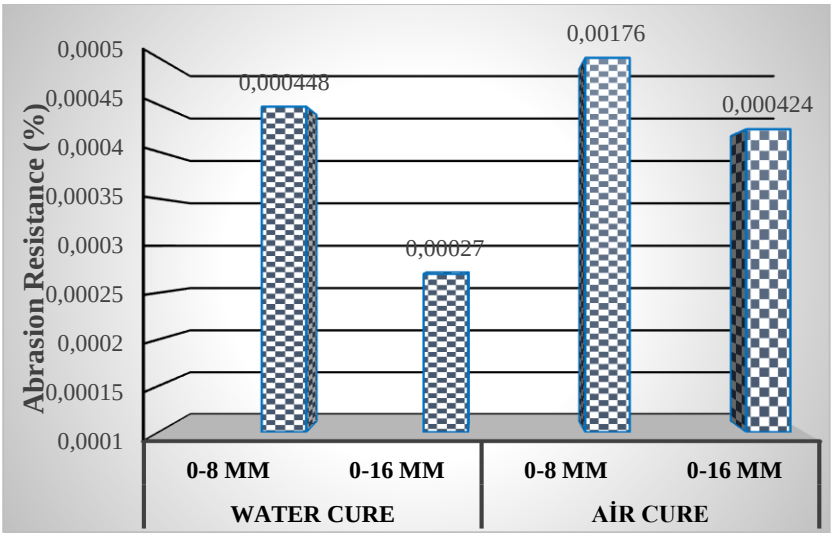

Figure 5. Abrasion Test Results

3.3. Porosity test

It is determined that the percentage of porosity in concrete samples gives better results in water-cured samples when Figure 6, which gives the results of the porosity test, is analyzed. It has been observed that the porosity of concrete samples produced with 0-8 mm aggregate group cured with water is 6.26%, and those cured with air are 13.13%. Thus, it can be said that concrete samples produced with 0-8 mm aggregate group cured with water are less void than air cured samples. In the concrete samples produced with 0-16 mm aggregate group, it was observed that the porosity of those cured with water was 4.13%, and those cured with air were 8.05%. Therefore, it can be said that water cured concrete samples have a more void-free structure than air cured samples. As a result, in terms of porosity, the cure made with water gave better results than the cure made with air. When Figure 6 is examined in terms of aggregate size, it is seen that porosity decreases with increasing aggregate size. As the grain size in the

sample decreases, the number of grain in the unit volume increases and the space volume between these grains increases and the porosity in the mixture increases [4].

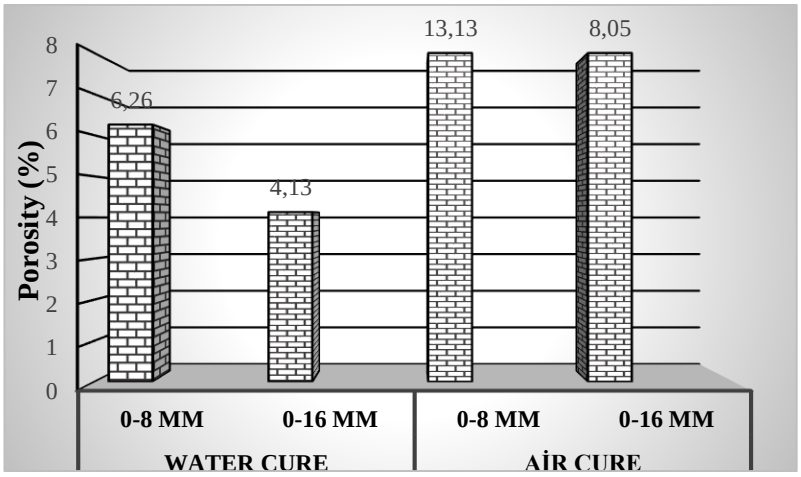

Figure 6. Porosity test results of concrete samples under different curing conditions

3.4. Carbonation test

The results of the carbonation test of the concrete samples according to the curing conditions are given in Figure 7.

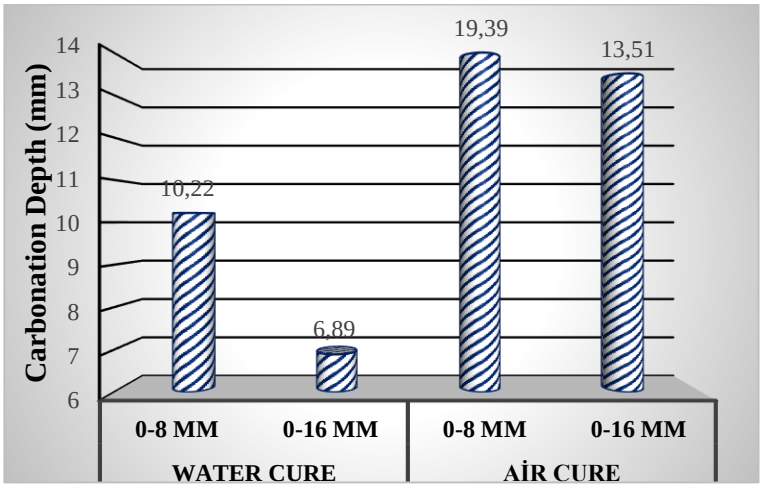

Figure 7. Carbonation test results of concrete samples in different curing conditions

When Figure 7 was analyzed, it was observed that carbonation in concrete samples gave better results in water-cured samples. It has been determined that the carbonation depth of the concrete samples produced with 0-8 mm aggregate group is 10.22 mm in water cured ones and 19.39 mm in air cured ones. Concrete samples produced with 0-8 mm aggregate group cured with water showed approximately 47% less carbonation than air cured samples. In the concrete samples produced with 0-16 mm aggregate group, the carbonation depth of those cured with water is 6.89 mm, and those cured with air are 13.51 mm. It has been observed that water cured concrete samples have approximately 49% less carbonation than air cured concrete samples. When Figure 7 was analyzed in terms of aggregate size, it was seen that the carbonation depth decreased with increasing aggregate size. Therefore, carbonation reactions are less in low porosity concretes [13].

Overall, by looking at Figure 8, it can be concluded that the compressive strength, porosity and carbonation depth of a concrete sample are related eachother.

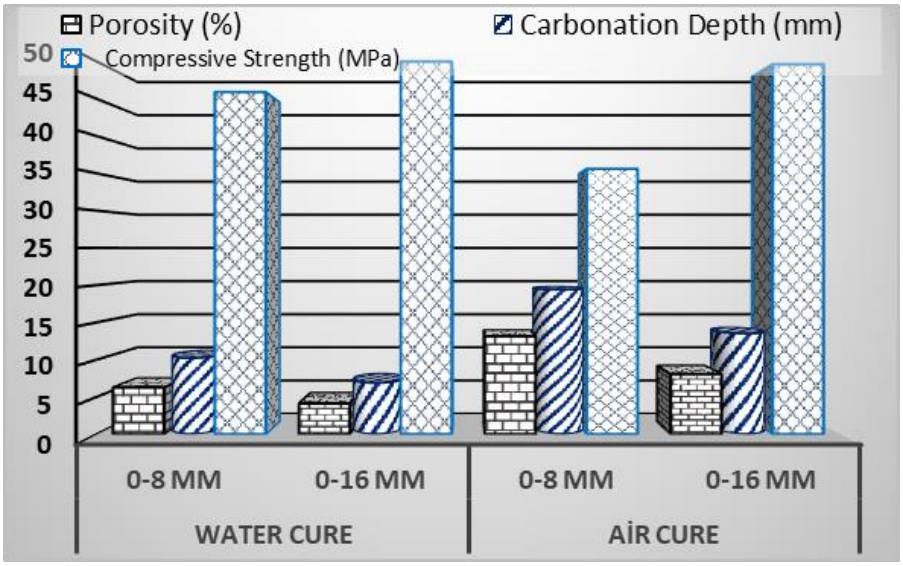

Figure 8. The results of porosity, carbonation and compressive strength tests.

4. Results

When we interpret our experimental data in terms of water cure and air cure, it was seen that the samples that were subjected to water curing performed better in terms of engineering properties compared to the air cured samples. The compressive strength of concrete samples subjected to water curing was higher. As a result of more voids in the samples that were cured in the air, the compressive strength has decreased and the abrasion, porosity and carbonation values have increased. In short, it was concluded that the water curing makes the concrete more resistant to external influences.

When the effect of aggregate size on the engineering properties of the samples was examined, it was observed that the compressive strength of the samples having 0-16 mm aggregate diameter range was higher than that of 0-8 mm aggregate grain size samples. We can conclude that when the aggregate granulometry grading of the samples is more balanced, it gives higher strength value.

It has been observed that samples having 0-16 mm aggregate diameter have lower porosity, abrasion and carbonation depth values. The use of larger size aggregates in conrete results in higher strength, in other words larger aggregate will create a lower surface area and lower water requirement. Therefore, a lower water cement ratio can be used, resulting in higher strength. As a result, it was observed that 0-16 mm aggregate group improved the engineering properties of the samples compared to 0-8 mm aggregate group.

References

[1] Şimşek O. Beton ve beton teknolojisi. 5. Baskı, Ankara, Türkiye: Seçkin Yayınları, 2015.
[2] Güçlüer K, Günaydın O, Tekin ÖF, Şahan MF. Farklı tipte agrega kullanımının betonun mekanik özelliklerine etkisinin araştırılması. NÖHÜ Müh Bilim Derg 2017; 6(1): 107-114.
[3] Özel C, Kaplan AN. Kendiliğinden yerleşen beton özellikleri üzerinde agrega özelliklerinin etkisi. USMTD 2017; 1(1): 1-6.
[4] Usta S. Agrega Granülometrisinin Beton Bileşimindeki Teorik Malzeme Miktarları ile Betonun Kompasite ve Porozite Değerleri Üzerindeki Etkilerinin İncelenmesi. Yapı teknol elektron Derg 2012; 8(1): 1-15.
[5] Neville AM. Properties of concrete. London: Longman, 1995.
[6] Özalp F, Şengül Ö, Taşdemir MA. Kür Koşulları ve Tecrit Malzemesinin Betonun Geçirimlilik ve Mekanik Özeliklerine Etkisi. THBB Derg 2015; 69-74.
[7] Özcan F, Atiş CD, Karahan O, Bilim C. Silis Dumanının ve Kür Şartlarının Harç Basınç Dayanımına Etkisi. 2014; Tam metin bildiri: http://www.imo.org.tr/resimler/ekutuphane/pdf/11143.pdf.
[8] TS EN 12390-3. Beton - Sertleşmiş beton deneyleri - Bölüm 3: Deney numunelerinin basınç dayanımının tayini. Türk Standartları Enstitüsü, Ankara, 2010.
[9] ASTM C944/C944M-12 Standard Test Method for Abrasion Resistance of Concrete or Mortar Surfaces by the Rotating-Cutter Method. West Conshohocken, PA; ASTM International, 2012.

[10] TS EN 12390-6. Beton - Sertleşmiş beton deneyleri - Bölüm 6: Deney numunelerinin yarmada çekme dayanımının tayini. Türk Standartları Enstitüsü, Ankara, 2010.
[11] Yazıcıoğlu S, Demirel B, Gönen T, Özer Ş. Farklı tip çimentoların betonun karbonatlaşmasına etkisi. UTBD 2012; 4(3): 112-120.
[12] Kara C, Yazicioglu S. Mermer tozu atığı ve silis dumanının betonun karbonatlaşma özelliğine etkisi. Bitlis Eren Univ J Sci 2016; 5(2): 191-202.
[13] Baradan B, Aydın S. Betonun Durabilitesi (Dayanıklılık, Kalıcılık). Beton 2013 Hazır Beton Kongresi; 2013; pp. 265-288.

C O P Y R I G H T R E L E A S E F O R M

TURKISH JOURNAL OF SCIENCE AND TECHNOLOGY (TJST)
Published by Firat University

Firat University, Fen Bilimleri Enstitüsü Müdürlüğü
Turkish Journal of Science & Technology Editörlüğü
Elazığ-TURKEY,
Manuscript title: .....
.....
.....
Full names of all authors (in order to appear on manuscript): .....
.....
Name, address etc. of corresponding author: .....
.....
.....
ID Number: ..... Telephone: .....
E-mail: ..... Mobile phone: .....

The author(s) warrant(s) that:
a) the manuscript submitted is his/her/their own original work;
b) all authors participated in the work in a substantive way and are prepared to take public responsibility for the work;
c) all authors have seen and approved the manuscript as submitted;
d) the manuscript has not been published and is not being submitted or considered for publication elsewhere;
e) the text, illustrations, and any other materials included in the manuscript do not infringe upon any existing copyright or other rights of anyone. Notwithstanding the above, the Contributor(s) or, if applicable the Contributor's Employer, retain(s) all proprietary rights other than copyright, such as
a) patent rights;
b) to use, free of charge, all parts of this article for the author's future works in books, lectures, classroom teaching or oral presentations;
c) the right to reproduce the article for their own purposes provided the copies are not offered for sale.
However, reproduction, posting, transmission or other distribution or use of the article or any material contained therein, in any medium as permitted hereunder, requires a citation to the Journal and appropriate credit to Firat University as publisher, suitable in form and content as follows:
Title of article, author(s), journal title and volume/issue, Copyright© year.
All materials related to manuscripts, accepted or rejected, including photographs, original figures etc., will be kept by Turkish Journal of Science and Technology editority for one year following the editor's decision. These materials will then be destroyed.
I/We indemnify Firat University and the Editors of the Journals, and hold them harmless from any loss, expense or damage occasioned by a claim or suit by a third party for copyright infringement, or any suit arising out of any breach of the foregoing warranties as a result of publication of my/our article. I/We also warrant that the article contains no libelous or unlawful statements and does not contain material or instructions that might cause harm or injury.
This copyright form must be signed by all authors. Separate copies of the form (completed in full) may be submitted by authors located at different institutions; however, all signatures must be original.

ID number: ..... ID number: .....
Full name (block letters) ..... Full name (block letters) .....
Signature ..... Date ..... Signature ..... Date .....
ID number: ..... ID number: .....
Full name (block letters) ..... Full name (block letters) .....
Signature ..... Date ..... Signature ..... Date .....
ID number: ..... ID number: .....

Turkish authors must supply their ID card number; foreign authors must supply their passport number (if possible)